

Copyright (c) by

DON HOWARD LEE

1969

DOUBLE INJECTION: HIGH FREQUENCY NOISE
AND TEMPERATURE DEPENDENCE

Thesis by
Don Howard Lee

In Partial Fulfillment of the Requirements
For the Degree of
Doctor of Philosophy

California Institute of Technology

Pasadena, California

1969

(Submitted May 8, 1969)

TO MY PARENTS

ACKNOWLEDGMENTS

The author would like to express his thanks to the many people at Caltech who contributed to the work presented herein. In particular, the author is indebted to Dr. M-A. Nicolet whose direction and guidance underlie this work. Also, the help of Drs. H. Bilger, E. McCarter and Mr. N. Harlambis during the summer recesses is also acknowledged.

A special note of thanks goes to Dr. C. A. Mead of Caltech and Mr. L. C. Hedrick of Tektronix Inc. for their constant encouragement and inspiration during the course of this work.

The double-injection diodes were generously provided by Drs. J. W. Mayer, R. Baron and Mr. O. J. Marsh, Hughes Research Laboratories, Malibu, California.

The financial support of Tektronix Inc., Fairchild Camera and Instrument, the Ford Foundation and the National Science Foundation through their Fellowship programs is gratefully acknowledged. This work was also supported in part by NASA Electronics Research Center, Cambridge, Mass. and the Jet Propulsion Laboratory by NASA Contract No. NAS 7-100.

Mrs. Doris Schlicht, who typed the manuscript, deserves special thanks for her patience and assistance. I am also grateful to my wife for her constant support and self-denial.

ABSTRACT

Noise measurements from 140°K to 350°K ambient temperature and between 10kHz and 22MHz performed on a double injection silicon diode as a function of operating point indicate that the high frequency noise depends linearly on the ambient temperature T and on the differential conductance g measured at the same frequency. The noise is represented quantitatively by $\langle i^2 \rangle = \alpha \cdot 4kTg\Delta f$. A new interpretation demands Nyquist noise with $\alpha \equiv 1$ in these devices at high frequencies. This is in accord with an equivalent circuit derived for the double injection process. The effects of diode geometry on the static I-V characteristic as well as on the ac properties are illustrated. Investigation of the temperature dependence of double injection yields measurements of the temperature variation of the common high-level lifetime τ ($\tau \propto T^2$), the hole conductivity mobility μ_p ($\mu_p \propto T^{-2.18}$) and the electron conductivity mobility μ_n ($\mu_n \propto T^{-1.75}$).

TABLE OF CONTENTS

CHAPTER I	HIGH FREQUENCY NOISE IN DOUBLE INJECTION	1
1.1.	Introduction	1
1.2.	DC Properties of the Semiconductor Regime	3
1.2.1.	Current-Voltage Characteristics	3
1.2.2.	Influence of Geometry on Semiconductor Regime I-V Characteristics	7
1.2.3.	Experimental Results on a Long Silicon $p^+ \pi n^+$ Structure From 140°K to 350°K	16
1.3.	Differential Step Response of Double Injection	20
1.4.	AC Properties of the Semiconductor Regime	25
1.4.1.	Small Signal ac Equivalent Circuit	25
1.4.2.	Experimental Verification of Results	30
1.4.3.	Nonlinear Effects	36
1.5.	High Frequency Noise in Double Injection Silicon Diodes	37
1.5.1.	Generalities	37
1.5.2.	Model of High Frequency Noise in Double Injection	41
1.5.3.	Measured Spectral Noise Density	45
1.6.	Evaluation of Results and Conclusion	53
1.7.	Discussion and Outlook	58
CHAPTER II	TEMPERATURE DEPENDENCE OF THE COMMON HIGH-LEVEL LIFETIME AND CONDUCTIVITY MOBILITY OF CARRIERS IN SILICON FROM DOUBLE INJECTION	64
2.1.	Introduction	64
2.2.	Temperature Dependence of the Current-Voltage Characteristic for Double Injection	65
2.3.	Common High-Level Lifetime Versus Temperature in Si	66
2.4.	Majority and Minority Carrier Mobility Versus Temperature in High Resistivity Silicon	68
2.5.	Conclusion	76
APPENDIX A	SOLUTION FOR GEOMETRICAL FACTOR	79
APPENDIX B	SOLUTION OF AC SMALL SIGNAL IMPEDANCE	81
APPENDIX C	THEORY OF NOISE MEASUREMENT AND EXPERIMENTAL PROCEDURE	88
C.1.	Noise Spectral Density	88
C.2.	Measurement System	89
C.3.	Small Signal AC Equivalent Circuit and Notation	89

C.4.	Measurement Procedure	93
C.5.	Analysis	93
APPENDIX D	REALIZATION OF NOISE MEASUREMENT APPARATUS	96
D.1.	Description of Amplifier and Input Circuitry	96
D.2.	Amplifier and Wave Analyzer Characteristics	102
D.3.	High Frequency Effects	104
D.4.	Low Frequency Effects	106
D.5.	Measurement of Gain Ratio η	107
D.6.	Comments on Construction	108
D.7.	Active Integrator	108
APPENDIX E	CALIBRATION MEASUREMENTS	112
E.1.	Wave Analyzer Detector	112
E.2.	Verification of Nyquist's Theorem	113
E.3.	Verification of Schottky's Theorem	114
E.4.	Resistor Calibration	115
APPENDIX F	TEMPERATURE ENVIRONMENT AND THERMOSTAT	119
F.1.	General Considerations	119
F.2.	Description of Thermostat	119
F.3.	Operation and Procedure	121
F.4.	Calibration	122
APPENDIX G	CURVE FITTING AND ERROR ANALYSIS	125
G.1.	Introduction	125
G.2.	Least-Squares Curve Fitting of a Function $I_{eq} = y(f, C_v)$	125
G.3.	Determination of the Weights w_i	127
G.4.	Computer Program	130
REFERENCES		132

CHAPTER I

HIGH FREQUENCY NOISE IN DOUBLE INJECTION1.1. Introduction.

Within the last few years, several experimental and theoretical studies directly related to the present subject of high frequency noise in double injection diodes have appeared in the literature. Two of the experimental investigators report that the mean square current fluctuations can be represented by

$$\langle i^2 \rangle = \alpha \cdot 4kT g \Delta f^* \quad (1.1.1)$$

with $\alpha \sim 1$, even though the two devices and their operating conditions are dissimilar. (1.1,1.2) In one case, the device is a long germanium diode operated in a square law range, whereas in the other case the device is a thin commercial germanium photocell biased in the V^3 range. Another study presents noise measurements on a long double injection silicon diode operated in the square law range. (1.3) The value of the limiting white noise level is stated there in terms of the low frequency conductance $\partial I / \partial V$

$$\langle i^2 \rangle = \beta \cdot 4kT (\partial I / \partial V) \Delta f \quad (1.1.2)$$

* Here k is Boltzman's constant; T the temperature in $^{\circ}K$; Δf the frequency interval and g the conductance of the device.

where $\beta = 0.52 \pm 0.1$ but the value of g at the measuring frequency is not given. These results obtained on dissimilar devices operating under different conditions seem to indicate a general fact, namely, that double injection exhibits thermal noise at high frequencies. The present investigation has therefore been undertaken to clarify the matter.

In general, the I-V characteristic is an unreliable means with which to confirm the presence of double injection. This is aptly demonstrated by Rose in his "comparative anatomy of models for double injection" in which two carrier injection encompasses a host of characteristics, including that of single injection.^(1.4) Fortunately, by determining such physical parameters as geometry, doping level, mobilities and lifetimes a specific mode of double injection can be established. The investigation presented here is primarily concerned with a long silicon (semiconductor) structure. Section 1.2 thus deals with the pertinent analysis and resulting dc features of this special case. The effects of geometry on the current voltage characteristic are also examined. Experimental results on a planar $p^+ \pi n^+$ silicon diode at room temperature confirm the analysis. The I-V characteristics are determined as a function of temperature, and a detailed description and analysis of the temperature behavior is presented in Chapter II. In Sections 1.3 and 1.4, which deal with transient and small signal ac behavior, an equivalent circuit is established for a long semiconductor double injection diode. The experimental verification of the results provide further confirmation of double injection. Nonlinear and temperature effects are also considered. Using the results from the transient and ac properties,

a model of the high frequency noise in double injection is proposed in Section 1.5. This model is verified by noise spectral density measurements. Section 1.6 contains an estimate of the magnitude of the low frequency noise spectral density which originates from generation-recombination effects.

1.2. DC Properties of the Semiconductor Regime.

1.2.1. Current-Voltage Characteristics. The current-voltage characteristics resulting from the simultaneous injection of electrons and holes (double injection) into insulator and high resistivity material have been dealt with in detail primarily by M. Lampert and A. Rose. (1.5, 1.6, 1.7) In fact, the latter has compiled and discussed some fourteen different models for two carrier injection. (1.4) Recently, J. Mayer, R. Baron and O. Marsh have experimentally verified three distinct double injection regimes predicted by Lampert and Rose. (1.8, 1.9, 1.10) These consist of the "insulator" ($J \propto V^3/L^5$), the "semiconductor" ($J \propto V^2/L^3$) and the negative resistance regimes. In conjunction with these experimental studies, the effects of diffusion and thermal generation on the I-V characteristics are investigated for both the insulator and semiconductor cases. (1.11, 1.12)

The basic time-independent equations which describe double injection current consists of (i) the current equations for the electrons and holes,

$$\vec{J}_n = q\mu_n [n\vec{E} + \beta(\nabla n)] \quad (1.2.1)$$

$$\vec{J}_p = q\mu_p [p\vec{E} - \beta(\nabla p)] \quad (1.2.2)$$

$$\vec{J} = \vec{J}_n + \vec{J}_p \quad (1.2.3)$$

where $\beta = \frac{kT}{q}$, $n = n_0 + \Delta n$ and $p = p_0 + \Delta p$, (ii) the charge conservation equations,

$$\frac{1}{q} (\nabla \cdot \vec{J}_n) = r \quad (1.2.4)$$

$$\frac{1}{q} (\nabla \cdot \vec{J}_p) = -r, \quad (1.2.5)$$

and (iii) Poisson's equation

$$\epsilon \nabla^2 \Phi = -q(\Delta p - \Delta n) = -\nabla \cdot (\epsilon \vec{E}) \quad (1.2.6)$$

Here, the symbols have their usual meanings, in particular, r is the net recombination rate, while n_0 , p_0 and Δn and Δp are the thermal equilibrium and net excess carrier densities for the electrons and holes respectively. Equation (1.2.4) is now multiplied by $1/\mu_n$ and (1.2.5) by $-1/\mu_p$. By adding, the following equation results

$$(p_0 - n_0) \nabla \cdot \vec{E} + \nabla \cdot [(\Delta p - \Delta n) \vec{E}] - \beta(\nabla^2 p + \nabla^2 n) = -\frac{(b+1)}{\mu_n} r \quad (1.2.7)$$

where $b = \mu_n/\mu_p$. Rewriting Eq.(1.2.3) in terms of (1.2.1) and (1.2.2) gives

$$\vec{J} = q\mu_p[p_0 + bn_0 + \Delta p + b\Delta n] \vec{E} + \beta(b\nabla n - \nabla p) \quad (1.2.8)$$

These equations, (1.2.7) and (1.2.8), are now subject to a set of assumptions called the "high-level approximations" which state that the excess electron and hole carrier densities are approximately equal and are much greater than the thermal equilibrium carrier densities; that is,

$$(a) \quad \Delta n \gg n_0 \quad (1.2.9a)$$

$$(b) \quad \Delta p \gg p_0 \quad (1.2.9b)$$

$$(c) \quad \Delta p \approx \Delta n \quad (\text{except that the value of } \Delta p - \Delta n \quad (1.2.9c) \\ \text{is taken from Poisson's equation}) .$$

The net recombination rate is defined by

$$r = \frac{\Delta n}{\tau_n} \approx \frac{\Delta p}{\tau_p} \quad (1.2.10)$$

which implies that there is a common high-level lifetime τ where

$$\tau = \tau_n \approx \tau_p \quad (1.2.11)$$

Under the high-level approximations, the individual retention in Eq.(1.2.7) of the first term, second term and third term produces respectively the semiconductor, insulator, and diffusion dominated regimes. Thus, the diffusion dominated regime is described by Eq. (1.2.8) and

$$2\beta v^2 p = \frac{(b+1)}{\mu_n \tau} p \quad (1.2.12)$$

which leads to the definition of an ambipolar diffusion length L_a , where

$$L_a = \sqrt{2\beta\tau \mu_n \mu_p / (\mu_n + \mu_p)} \quad (1.2.13)$$

Retaining only the second term of Eq.(1.2.7) results in

$$\nabla \cdot \left[\frac{\epsilon}{q} (\nabla \cdot \vec{E}) \vec{E} \right] = - \frac{(b+1)}{\mu_n \tau} p \quad (1.2.14)$$

This leads to the Lampert insulator regime in which the one dimensional I-V characteristic is given by

$$J = (125/18) \epsilon \mu_p \mu_n \tau V^3 / L^5, \quad (1.2.15)$$

where L is the length of the diode. Similarly, the retention of only the first term yields

$$(p_0 - n_0) \nabla \cdot \vec{E} = - \frac{(b+1)}{\mu_n \tau} p \quad (1.2.16)$$

In this case, the resulting semiconductor regime is described by the current-voltage characteristic

$$J = (9/8) q \mu_p \mu_n \tau (p_0 - n_0) V^2 / L^3 \quad (1.2.17)$$

The initial behavior at low injection levels is, of course, given by

$$\vec{J} = q \mu_p (p_0 + b n_0) \vec{E} \quad (1.2.18)$$

which is just the ohmic regime.

The investigation here is totally focused on a double injection diode made from high resistivity π type silicon. This diode is "sister" to those previously investigated in Reference 1.10 and has parameters such that the semiconductor regime is the principal double injection mode. Therefore, the primary concern with the remainder of this work will be the semiconductor regime described by Eqs.(1.2.8), (1.2.16) and (1.2.17).

1.2.2. Influence of Geometry on Semiconductor Regime I-V Characteristics. The theoretical and experimental investigation of the current-voltage characteristics of Lampert's two-carrier semiconductor regime have been entirely concerned with the one and two dimensional planar cases (i.e. rectangular diodes). In this section the effect of geometry on the dc properties is examined. Only the semiconductor regime $p^+ \pi n^+$ type structures are investigated. As an example, the planar case is illustrated in Figure 1.2.1. Here, the p^+ contact supplies the holes and the n^+ contact the electrons.

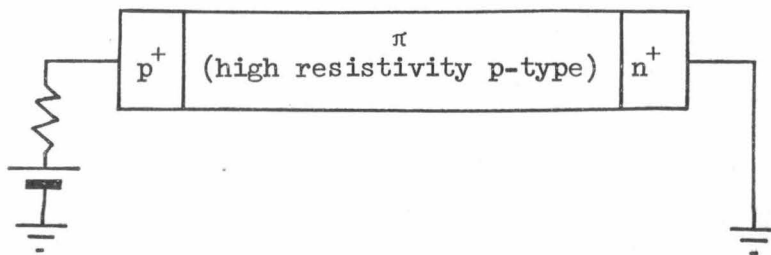


Figure 1.2.1
Planar $p^+ \pi n^+$ double injection diode

From Eqs.(1.2.8) and (1.2.16), the current density can be written as

$$\vec{J} = - q\mu_p\mu_n\tau(p_0 - n_0)(\nabla \cdot \vec{E}) \vec{E} . \quad (1.2.19)$$

Since the divergence of the current density is zero (i.e. $\nabla \cdot \vec{J} = 0$), and if the condition of spatial uniformity for the mobilities, common high-level lifetime and the net thermal equilibrium carrier density ($p_0 - n_0$) is maintained, then

$$\nabla \cdot [(\nabla \cdot \vec{E})\vec{E}] = 0 . \quad (1.2.20)$$

Equation (1.2.20) is now solved for the electric field subject to the following conditions:

- (i) The diode is forward biased as shown in Figure 1.2.1. The voltage across the structure is V . There is no appreciable voltage drop across either the p^+ or n^+ regions.
- (ii) The electric field at the electron emitting boundary R_2 ($n^+ - \pi$ contact) is zero (i.e. $\vec{E}(R_2) = 0$).
- (iii) The electric field is a function of only one coordinate direction, that is, $\vec{E} = E(u_1) \vec{e}_1$.

The potential and charge distributions can be determined from the electric field by

$$\Phi = - \int_c E(u_1) du_1 \quad (1.2.21)$$

and

$$n \approx p = - \frac{\mu_n \tau (p_0 - n_0)}{b + 1} \nabla \cdot \vec{E} \quad (1.2.22)$$

Condition (iii) is fulfilled by the cylindrical, spherical and planar geometrical configurations. By applying the divergence operator for curvilinear orthogonal coordinate systems, Eq.(1.2.20) is easily integrated twice for the electric field (see Appendix A). Integrating the electric field along u_1 from R_1 to R_2 , the expression for the current-voltage characteristic results in

$$I_{D.I.} = \delta q \mu_p \mu_n \tau (p_0 - n_0) V^2 \quad (1.2.23)$$

The factor δ depends only on the geometry and is therefore called the geometrical factor. This factor does not alter the square-law relationship of the I-V characteristic but influences only the magnitude. It is interesting to observe that since the spatial dependences of the charge carriers and thus the electric field are functionally the same for pure unipolar space charge limited current, the geometrical factors are identical. (1.13) That is, for single injection*

$$I_{S.I.} = \delta \mu \epsilon V^2 \quad (1.2.24)$$

* In this case, however, the appropriate boundary condition is that the electric field be zero at R_1 rather than at R_2 . Also, the introduction of the notion of space charge current is relevant since for double injection the small difference in excess charge densities ($\Delta p - \Delta n$) does indeed form a space charge and can therefore be discussed in terms of single injection space charge current. It is also noted that R_1 in Figure 1.2.1 is located at the $p^+ - n$ contact.

By taking the ratio of Eqs.(1.2.23) and (1.2.24) and assuming $\mu = \mu_n$,

$$I_{D.I.}/I_{S.I.} = \tau/\tau_R \quad (1.2.25)$$

where τ_R is the dielectric (or Ohmic) relaxation time and is defined by

$$\tau_R = \epsilon/q \mu_p (p_0 - n_0) . \quad (1.2.26)$$

Here, the ratio of double injection current to space charge limited current is not only independent of the geometrical factor but is determined solely by the bulk lifetime and dielectric relaxation time.*

Equation (1.2.25) thus provides a means for determining the dominant mode of injection. For a given situation in which the semiconductor regime can exist, the bulk lifetime will in general be much greater than the relaxation time. Under this condition, the contribution of any space charge current to the overall current density will be negligible (see Section 1.2.3).

* It should be noted that a similar comparison between the double injection "insulator" regime (see Eq.(1.2.15)) and single injection space charge limited current leads to

$$\hat{I}_{D.I.}/I_{S.I.} = \frac{\hat{\delta}}{\delta} \tau \mu_p V$$

where $\hat{\delta}$ is defined to be the geometrical factor associated with the insulator regime. The quantity $\hat{\delta}/\delta$ is, in general, a function of geometrical terms in contrast to expression (1.2.25). In particular, for the planar case

$$\hat{I}_{D.I.}/I_{S.I.} = (500/81) \tau/T_p$$

where the transit time T_p is defined as

$$T_p = L^2/(\mu_p V) .$$

Here the ratio of the double injection insulator regime current to that of space charge current is determined not only by geometrical factors but by the bulk lifetime and a transit time T_p .

The low-level injection behavior is described by Ohm's Law (Eq. (1.2.18)) and can be expressed as

$$I_{\Omega} = \frac{1}{\bar{\delta}} q \mu_p (p_o + bn_o) V \quad (1.2.26)$$

where

$$\bar{\delta} = \frac{h_2 h_3}{A} \int_{R_1}^{R_2} \frac{du_1}{h_2 h_3} \quad (1.2.27)$$

The terms h_1^2 , h_2^3 and h_3^2 are the diagonal elements of the metric tensor of the coordinate system and A is the cross-sectional area. In this case, the quantity $1/\bar{\delta}$ is the appropriate geometrical factor for the ohmic mode. A transition voltage V_T is now defined to be that voltage which makes the ohmic current equal to the double injection current. Therefore, from Eq.(1.2.25) and (1.2.27) the transition voltage V_T is

$$V_T = \frac{1}{\bar{\delta} \delta} \frac{1}{\mu_n \tau} \frac{(p_o + bn_o)}{(p_o - n_o)} \quad (1.2.28)$$

When the thermal equilibrium hole carrier concentration p_o is much larger than the electron concentration n_o , Eq.(1.2.28) reduces to

$$V_T = \frac{1}{\bar{\delta} \delta} \frac{1}{\mu_n \tau} \quad (1.2.29)$$

Since the quantity $1/\bar{\delta} \delta$ has dimensions of length squared (i.e. $1/\bar{\delta} \delta \sim L^2$ for the planar case), Rose has suggested that the onset of the

semiconductor regime occurs when the minority carrier transit time is of the order of the bulk high-level lifetime (i.e. $T_n \simeq 1/(\bar{\delta}\delta\mu_n V_T) \simeq \tau$). Table 1.2.1 summarizes the analytical expressions for the geometrical factors, electric fields and carrier density profiles. (1.14, 1.15) For convenience of comparison, the planar case is also presented. Two cases are considered with respect to the cylindrical and spherical structures. In case (a), the total current density is directed radially outward, whereas in case (b), the total current density is directed radially inward. Figure 1.2.2 contains qualitative plots of the electric fields and carrier densities. Here, the influence of geometry is clearly evident. In particular, the electric field for case (b) of the spherical geometry possesses a maximum value when ρ/ρ_1 equals $4^{1/3}$ (i.e. $\rho/\rho_1 = 1.587$).^{*} Figure 1.2.3 illustrates the appropriate normalized geometrical factors as a function of the ratio of the radii. For the cases (a) and (b) in either the cylindrical or spherical geometries, the ratio of the double injection currents is not equal to unity but depends on the ratio of the radii. This current ratio, which is just the ratio of the geometrical factors, for the cylindrical case is given by

$$\left[\frac{I_b}{I_a} \right]_{\text{Cylindrical}} = \frac{\left\{ \rho_2 \left[\ln_e \left[\frac{\rho_2}{\rho_1} + \left[\frac{\rho_2}{\rho_1} \right]^2 - 1 \right]^{1/2} \right] - \left[1 - \left[\frac{\rho_1}{\rho_2} \right]^2 \right]^{1/2} \right\}^2}{\rho_1 \left[\left[\frac{\rho_2}{\rho_1} \right]^2 - 1 \right]^{1/2} - \cos^{-1} \left[\frac{\rho_1}{\rho_2} \right]} \quad (1.2.30)$$

* The symbol ρ instead of r is used to designate the radial variable to avoid confusion with the notation for the dynamic impedance.

TABLE 1.2.1

Geometrical factors, electric fields and charge distributions for semiconductor regime double injection diodes in the planar, cylindrical and spherical geometrics.

GENERAL RELATIONSHIPS:		$I_{D.I.} = \delta q \mu_n \mu_p \tau (p_o - n_o) V^2$				$V_T = \frac{1}{\delta b} \left[\frac{1}{\mu_n \tau} \right]$
TYPE OF STRUCTURE	PLANAR $u_1 = x$	CYLINDRICAL CASE (a) $u_1 = \rho$	CYLINDRICAL CASE (b) $u_1 = \rho$	SPHERICAL CASE (a) $u_1 = \rho$	SPHERICAL CASE (b) $u_1 = \rho$	
DOUBLE-INJECTION GEOMETRICAL FACTOR δ	$\frac{9}{8} \frac{A}{L^3}$	$\frac{2\pi H}{\rho_2} \left[\ln_e (z + (z^2 - 1)^{\frac{1}{2}}) - \frac{(z^2 - 1)^{\frac{1}{2}}}{z} \right]^{-2}$	$\frac{2\pi H}{\rho_1} \left[(z^2 - 1)^{\frac{1}{2}} - \cos^{-1} \frac{1}{z} \right]^{-2}$	$\left[\int_{\rho_1}^{\rho_2} \left[\frac{\rho_2^3 - \rho^3}{6\pi \rho^4} \right]^{\frac{1}{2}} d\rho \right]^{-2}$	$\left[\int_{\rho_1}^{\rho_2} \left[\frac{\rho^3 - \rho_1^3}{6\pi \rho^4} \right]^{\frac{1}{2}} d\rho \right]^{-2}$	
OHMIC GEOMETRICAL FACTOR $\bar{\delta}$	$\frac{L}{A}$	$\frac{1}{2\pi H} \ln_e \left[\frac{\rho_2}{\rho_1} \right]$	$\frac{1}{2\pi H} \ln_e \left[\frac{\rho_2}{\rho_1} \right]$	$\frac{1}{4\pi} \left[\frac{\rho_2 - \rho_1}{\rho_2 \rho_1} \right]$	$\frac{1}{4\pi} \left[\frac{\rho_2 - \rho_1}{\rho_2 \rho_1} \right]$	
ELECTRIC FIELD $E(u_1)$	$\frac{3}{2} \frac{V}{L} \left(1 - \frac{x}{L} \right)^{\frac{1}{2}}$	$P \left[\left[\frac{\rho_2}{\rho} \right]^2 - 1 \right]^{\frac{1}{2}}$	$P \left[1 - \left[\frac{\rho_1}{\rho} \right]^2 \right]^{\frac{1}{2}}$	$\frac{M \left[\rho_2^3 - \rho^3 \right]^{\frac{1}{2}}}{\rho^2}$	$\frac{M \left[\rho^3 - \rho_1^3 \right]^{\frac{1}{2}}}{\rho^2}$	
CHARGE-DENSITIES $n(u_1) \sim p(u_1)$	$\frac{3}{4} \frac{V}{L^2} Q^{\frac{1}{2}} \left(1 - \frac{x}{L} \right)^{-\frac{1}{2}}$	$\frac{\rho_2^2}{PQ} \left[1 - \left[\frac{\rho}{\rho_2} \right]^2 \right]^{-\frac{1}{2}}$	$\frac{\rho_1^2}{PQ} \left[\left[\frac{\rho}{\rho_1} \right]^2 - 1 \right]^{-\frac{1}{2}}$	$\left[\frac{MN}{\rho_2^3 - \rho^3} \right]^{\frac{1}{2}}$	$\left[\frac{MN}{\rho^3 - \rho_1^3} \right]^{\frac{1}{2}}$	
DEFINITION OF SYMBOLS	L = Length H = Height A = Area ρ_1 = inside radius ρ_2 = outside radius ($\rho_2 > \rho_1$)	$z = \rho_2 / \rho_1$ $P = I / (2\pi H q \tau \mu_n \mu_p (p_o - n_o))$ $Q = \left[\frac{\mu_n \tau (p_o - n_o)}{b + 1} \right]^2$	$M = I / (6\pi q \tau \mu_n \mu_p (p_o - n_o))$ $N = \frac{9}{4} Q$			

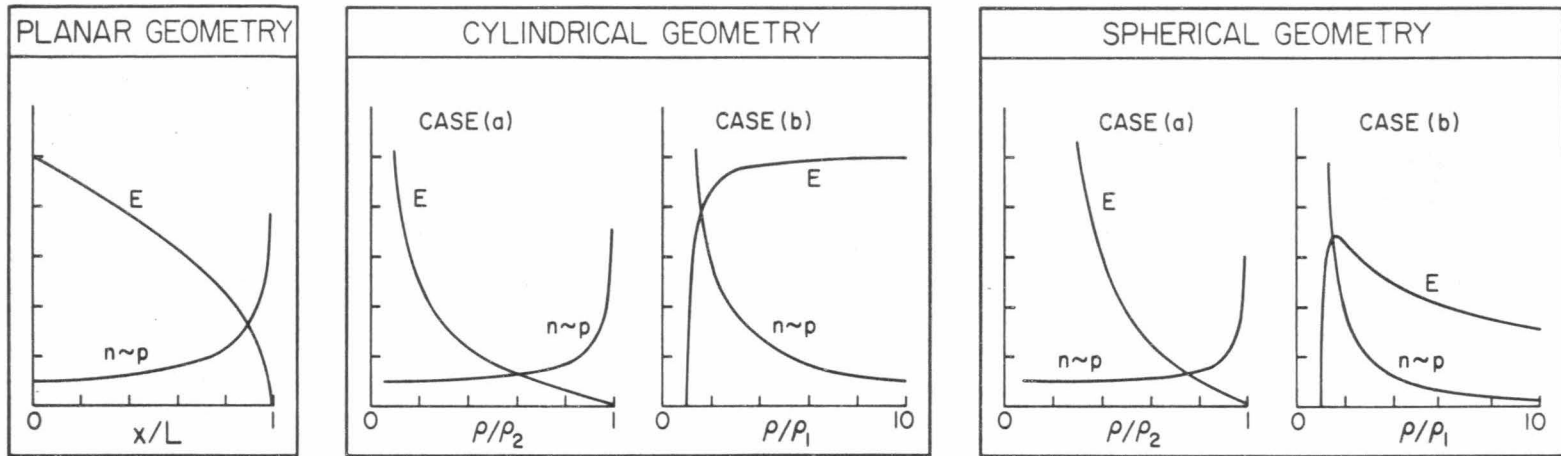


Figure 1.2.2. Qualitative representation of the electric field and charge distributions for the semiconductor regime double injection in planar, cylindrical and spherical configurations (ρ = radial variable).

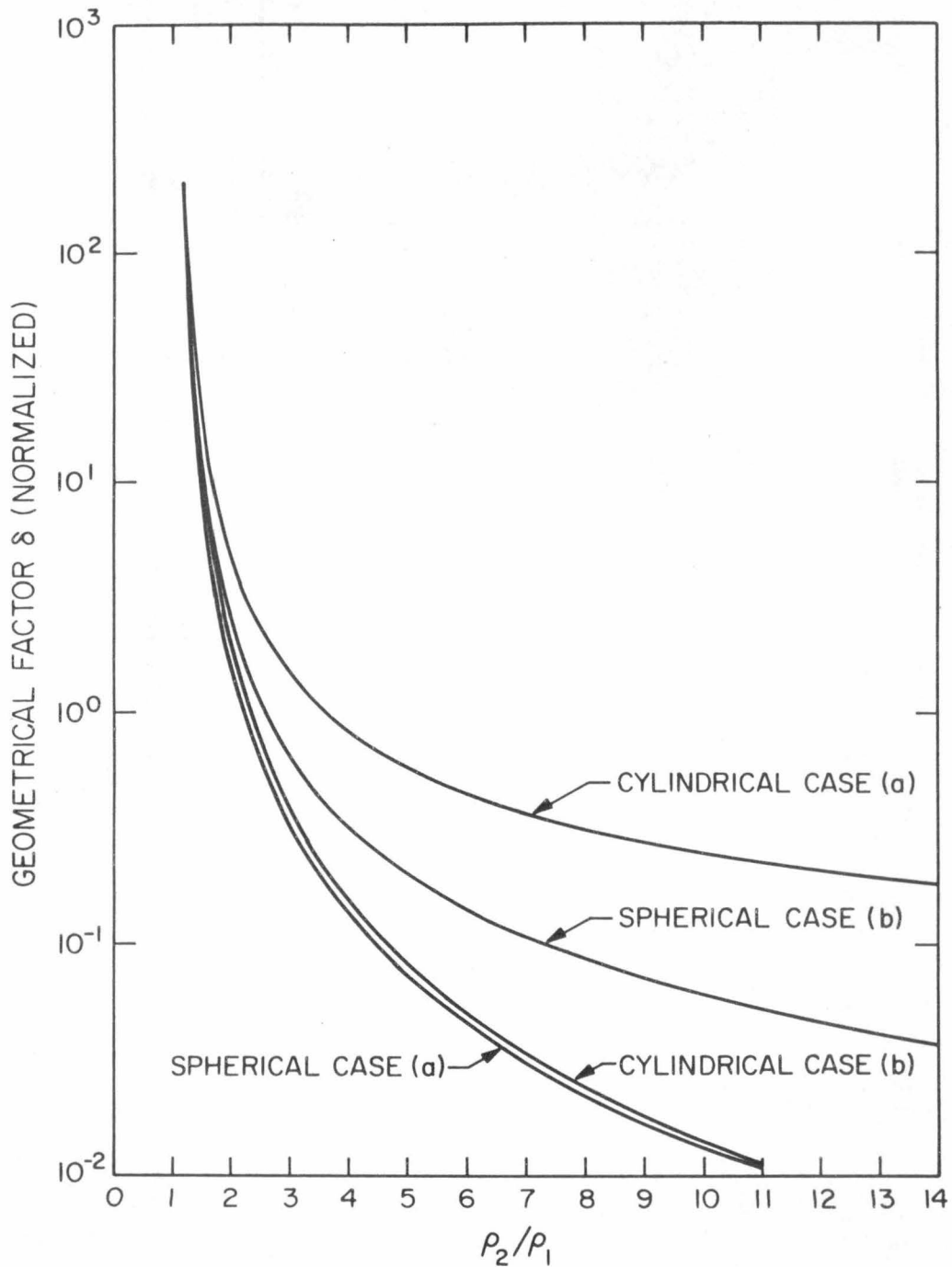


Figure 1.2.3. Normalized geometrical factor as a function of the radii ratio ρ_2/ρ_1 for cylindrical and spherical geometries.

and for the spherical case by

$$\left[\frac{I_b}{I_a} \right]_{\text{Spherical}} = \frac{\rho_2}{\rho_1} \left[\frac{\int_1^{\rho_1/\rho_2} \frac{(1-x^3)^{1/2}}{x^2} dx}{\int_1^{\rho_1/\rho_2} \frac{(x^3-1)^{1/2}}{x^2} dx} \right]^2 \quad (1.2.31)$$

Equation (1.2.30) and the numerical solution of Eq.(1.2.31) are plotted in Figure 1.2.4. Here, in each case, the current ratio I_b/I_a is a smoothly increasing function of the ratio of the radii. It is also noted that for a given radii ratio, the spherical geometry current ratio is always greater than that for the cylindrical geometry.

Since the same geometrical factors apply to unipolar space charge limited current (see Eq.(1.2.24)), Figures 1.2.3 and 1.2.4 are also valid for single injection structures.

1.2.3. Experimental Results on a Long Silicon $p^+ \pi n^+$ Structure from 140°K to 350°K. A planar double injection diode is made from high-resistivity float zone grown p-type silicon. The n^+ region is formed by lithium diffusion whereas the p^+ region is formed by evaporating aluminum and alloying. Electrical contact to the n^+ and p^+ region is accomplished by applying a mixture (1:1) of gallium and indium. Further construction details are presented in Ref. 1.10. Figure 1.2.5 contains the physical dimensions of the diode and approximate doping as specified by the manufacture. The measured current-voltage characteristics as a function of temperature is also shown in Figure 1.2.5.* The ambient temperature extends from 140°K to 350°K and all points are taken

* Appendix F contains the description of the experimental equipment and procedure for varying the ambient temperature.

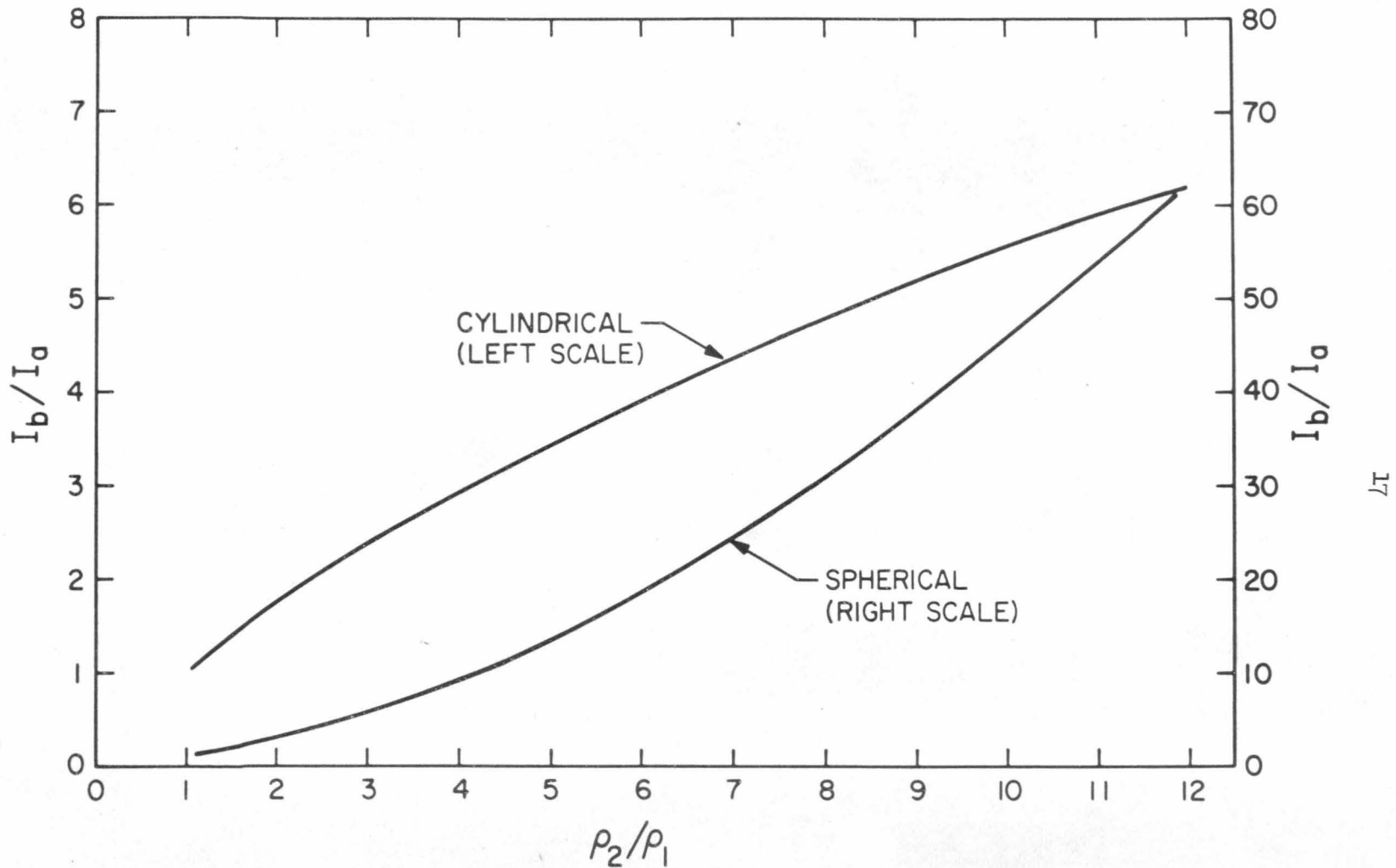


Figure 1.2.4. Current ratio I_b/I_a versus the radii ratio ρ_2/ρ_1 for cylindrical and spherical geometries.

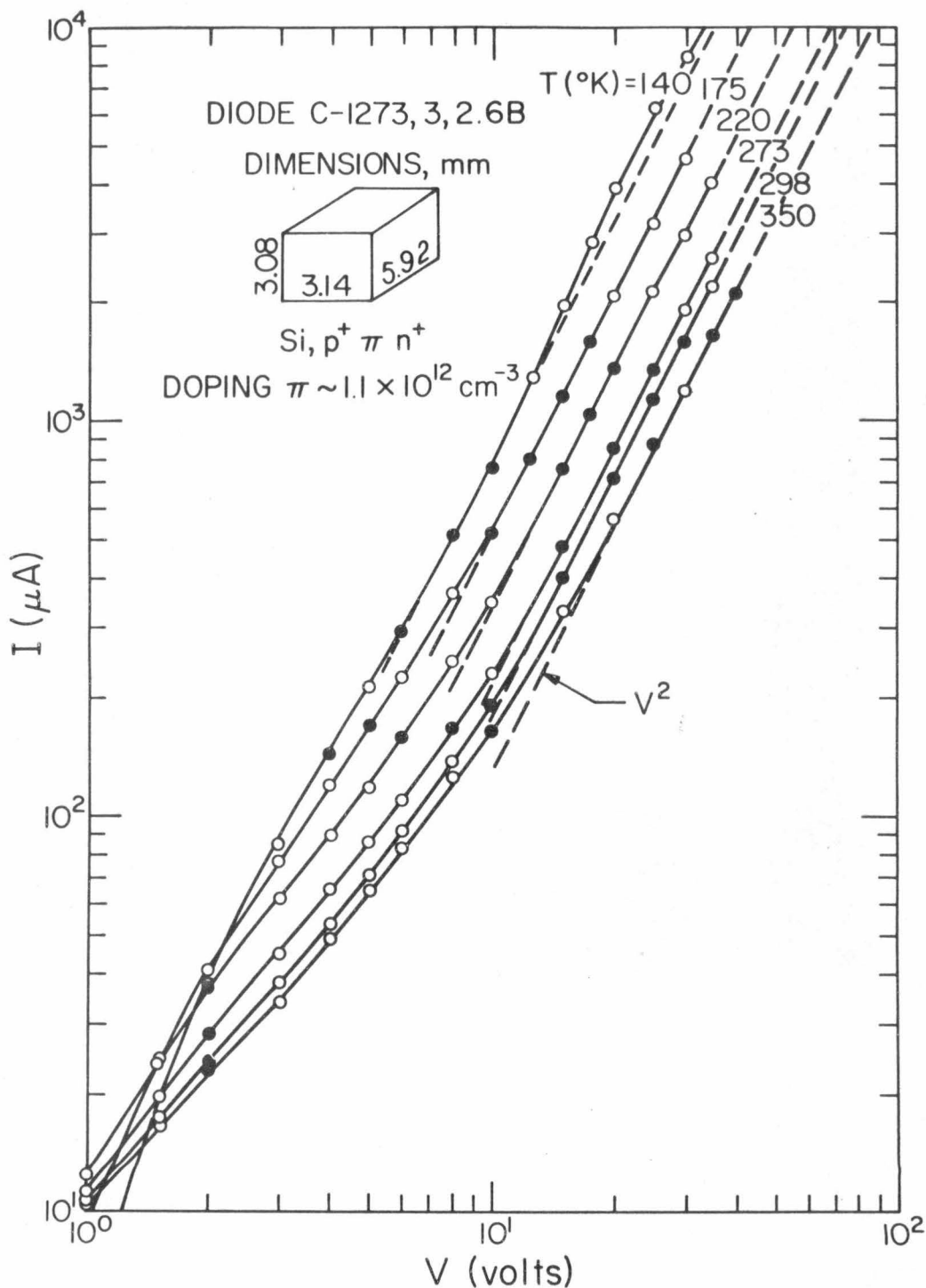


Figure 1.2.5. I-V characteristics of a silicon double injection diode between 140°K and 350°K ambient temperature. The solid dots indicate the operating points at which noise measurements have been made.

with the diode in the "dark". For the purpose of the ensuing noise measurement, a respectable square law range need exist. This criterion is met by the present diode since a quadratic behavior is observed over approximately a decade of current for each of the considered temperatures. At 140°K, the deviation from the square law (dashed line) at the higher current levels could possibly be due to diffusion or heating effects as discussed by R. Baron.^(1.12) The deviation from the ohmic behavior at low injection levels is attributed to junction effects. For a given voltage, the square law current is seen to increase with decreasing temperature. This behavior is expected since the electron and hole mobilities each possess this type of temperature variation. The temperature dependence of the double injection I-V characteristic in the semiconductor regime is treated in Chapter II.

Since the host material is π type, the thermal equilibrium hole concentration p_0 is much greater than the thermal equilibrium electron concentration n_0 . Therefore, Eq.(1.2.17) describing the semiconductor regime reduces to

$$I = A \frac{q}{8} \mu_p \mu_n \tau p_0 \frac{V^2}{L^3} . \quad (1.2.32)$$

The measured room temperature ($T = 298^\circ\text{K}$) values are $q \mu_p p_0 = 69.5 \times 10^{-6} \frac{\text{a}}{\text{v-cm}}$, $\mu_n = 1280 \frac{\text{cm}^2}{\text{v-s}}$, $\tau = 30.7 \times 10^{-6} \text{ s}$, $A = 9.67 \times 10^{-2} \text{ cm}^2$ and $L = 5.92 \times 10^{-1} \text{ cm}$. From Eq.(1.2.32) the theoretical double injection square law current at 30 volts is 1.4 ma. This theoretical value is approximately 14% below the measured value of 1.6 ma (see Figure 1.2.5). However, R. Baron

has shown that this is expected from the effects of diffusion and thermal generation. (1.12)

From Eq.(1.2.25) the ratio of the measured bulk high-level lifetime (30.6μ sec) to the calculated dielectric relaxation time (15.3 ns) is 2×10^3 . This illustrates the magnitude of two carrier injection current over that of single injection and provides further assurance that the dominant mode is double injection. The negative resistance regime discussed by M. A. Lampert and J. W. Mayer was not observed under any of the present experimental conditions described herein. (1.7, 1.8)

1.3. Differential Step Response of Double Injection.

As pointed out by R. Baron et.al., additional information on the properties of a double injection diode can be easily obtained from its differential step response. (1.16) Consider the case of an I-V characteristic as shown in Figure 1.3.1 where $I \propto V^2$. If the current is indeed entirely due to double injection as prescribed by Eq.(1.2.17), an incremental voltage step ΔV applied at $t = 0$ should generate the current response shown by the solid line of Figure 1.3.2. There is an instantaneous increase of current $\Delta i(0)$ at $t = 0^+$ followed by a second increase of $\Delta i(\infty)$ after several time constants τ_1 . The explanation of this behavior rests on the hypothesis that injected charge can not change instantaneously. Therefore, immediately after the application of the voltage pulse ΔV , the diode behaves as a series of resistive elements whose values depend on the amount of charge stored in every interval dx along the length L of the diode. At $t = 0^+$ the resistance is accordingly given by

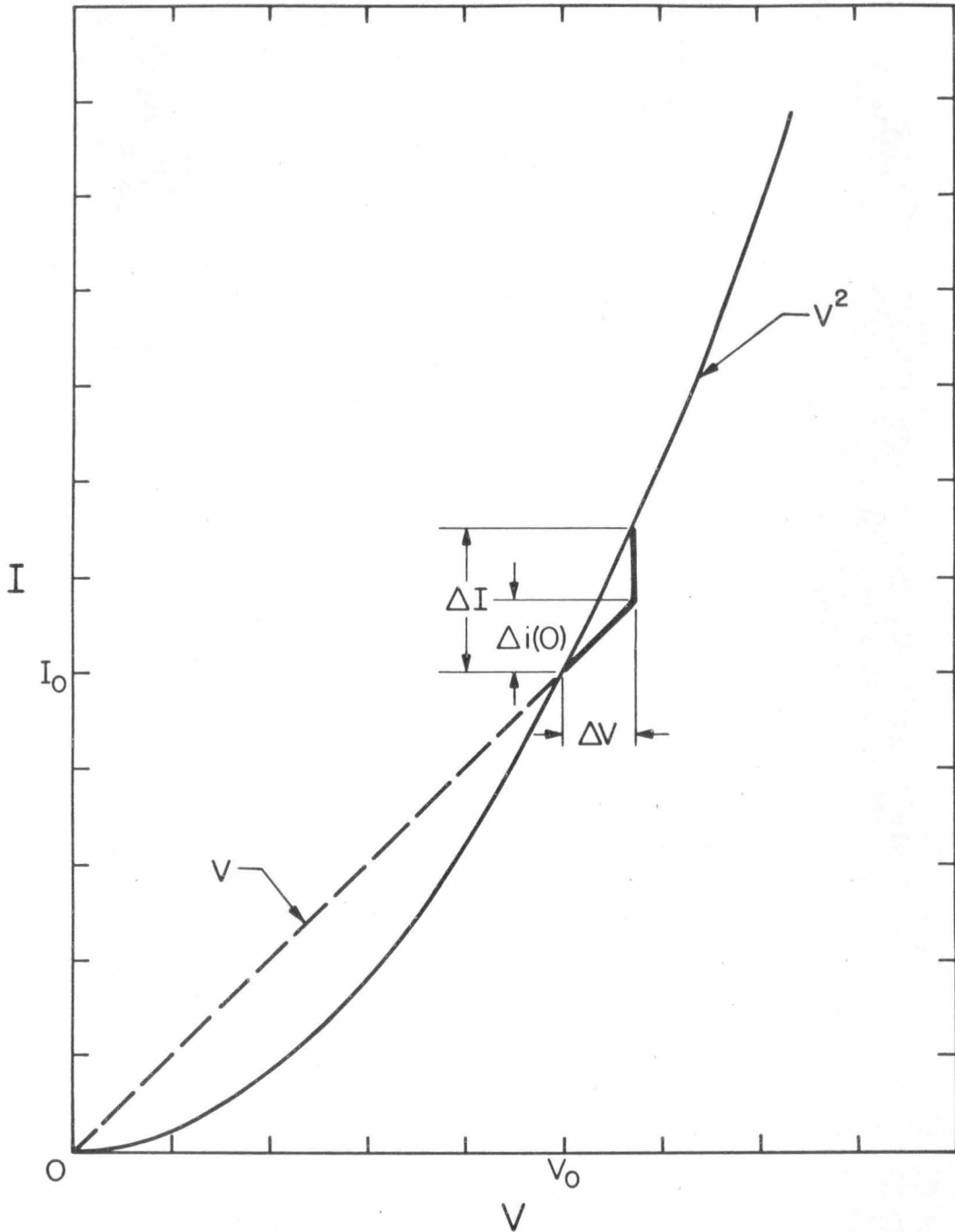


Figure 1.3.1. Ideal characteristics of a double injection diode in the semiconductor regime ($I \propto V^2$). (see text for details).

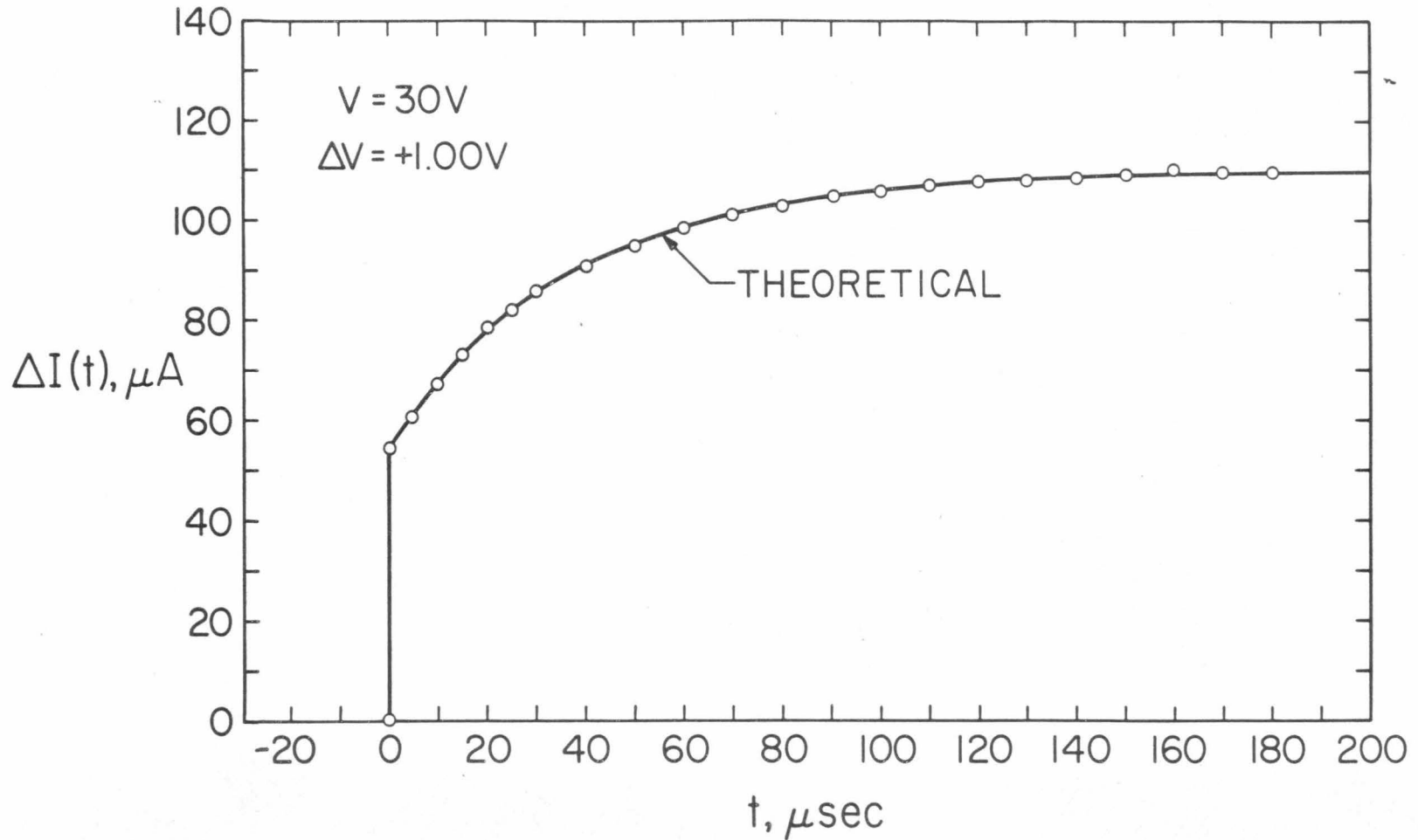


Figure 1.3.2. Current response of the diode of Figure 1.2.5 to a differential voltage step of + 1V at an operating point of 30V, 1.6 mA. The solid line is a least squares fit of $\Delta i(t) = \Delta i(0) + \Delta i(\infty) [1 - \exp(-t/\tau)]$ to the data.

$$r = \int_0^L [Aq(\mu_n n(t=0) + \mu_p p(t=0))]^{-1} dx = \int_0^L [A\sigma(t=0)]^{-1} dx \quad (1.3.1)$$

Since, in general, the densities n and p of the electrons and holes vary with the distance x , the requirement that the current $\Delta i(0)$ be free of divergence demands that the additional field $\Delta E(x)$ generated by ΔV will not be constant either. It will, in fact, have to adjust itself everywhere such that $\Delta E(x) \cdot A\sigma(t=0) = \Delta i(0)$ is constant. This is achieved by minute rearrangements of charge in the bulk which takes place within a time span of the order of the dielectric relaxation time $\theta = \epsilon/\sigma$. Hence, $\Delta E(x) \cdot A\sigma(t=0) = \Delta i(0)$ and $\int_0^L \Delta E(x) dx = \Delta V$. As long as diffusion contributes negligibly to the dc current, the dc value $E(x)$ of the electric field satisfies $E(x) \cdot A\sigma(t=0) = I_0$, and $\int_0^L E(x) dx = V_0$. It thus follows that

$$\frac{1}{r} = \frac{\Delta i(0)}{\Delta V} = \frac{I_0}{V_0}, \quad (1.3.2)$$

as indicated in Figure 1.3.1.

The relationship between the initial step and the second increment follows from the law $I \propto V^2$ and is

$$\Delta i(\infty) = \frac{\Delta V + V_0}{V_0} \Delta i(0) \quad (1.3.3)$$

where V_0 is the initial bias voltage as shown in Figure 1.3.1. If the incremental step voltage ΔV is much smaller than the bias voltage V_0 , then $\Delta i(\infty) \simeq \Delta i(0)$. In the limit as ΔV approaches zero (differential input), Eq.(1.3.3) reduces to the differential form

$$di(\infty) = di(0) \quad . \quad (1.3.4)$$

If the dc characteristic is of the form $I \propto V^n$, then similarly,

$$di(\infty) = (n-1) di(0) \quad . \quad (1.3.5)$$

By assuming the presence of a single linear recombination mechanism, this current transition will take place with a single time constant τ_1 which is equivalent to the previously defined high-level lifetime τ (i.e. $\tau_1 = \tau$); hence,

$$\Delta I(t) = \Delta i(0)[2-e^{-t/\tau}] \quad . \quad (1.3.6)$$

The step response of single injection space charge current contrasts with that of double injection in that the characteristic time scale is the transit time (of the order of $L^2/\mu V$) rather than a lifetime. It is also noted that the above argument is independent of the geometrical configuration of the double injection structure. It follows thusly, that Eqs.(1.3.2) and (1.3.5) are also valid for cylindrical and spherical geometries as well.

An experimental incremental pulse response of the double injection diode of Figure 1.2.5 biased at 30V and 1.6ma is shown in Figure 1.3.2 (open circles). The excellent agreement between the theoretical current response (Eq.(1.3.6)) and the experimental data indicates that the assumption of negligible diffusion is valid. The differential step response not only provides a convenient means for verifying the

double injection semiconductor regime but also provides a direct measurement of the high-level lifetime τ and high frequency differential resistance r .

1.4. AC Properties of the Semiconductor Regime.

1.4.1. Small Signal AC Equivalent Circuit. To facilitate the understanding of the noise properties of double injection, it is advantageous to obtain the small signal ac equivalent circuit of the diode. Of course, the transient analysis described in section 1.3 is an equally valid means with which to establish a small signal equivalent circuit. However, since the noise measurement involves a frequency spectrum, a more equivalent approach is to establish the properties of the double injection diode as a function of frequency.

The dc equations of Section 1.2.1 are generalized to include time dependent quantities (i.e. $E(t)$ and $p(t)$). With the same assumptions of high-level injection and negligible diffusion, the equations describing the semiconductor regime are given by

$$\vec{J} = q\mu_p p^{(b+1)} \vec{E} + \epsilon \frac{\partial \vec{E}}{\partial t} \quad (1.4.1)$$

and

$$(p_o - n_o) \nabla \cdot \vec{E} = - \frac{(b+1)}{\mu_n} \left[\frac{p}{\tau} + \frac{\partial p}{\partial t} \right] . \quad (1.4.2)$$

The charge density, electric field and current density are now written in the form

$$p = P_0 + P_1 e^{j\omega t} \quad (1.4.3a)$$

$$E = E_0 + E_1 e^{j\omega t} \quad (1.4.3b)$$

$$J = J_0 + J_1 e^{j\omega t} \quad (1.4.3c)$$

where each of the variables is assumed to be a function of only one spatial coordinate u_1 as in Section 1.2. By substituting these variables into Eqs.(1.4.1) and (1.4.2), the zero subscript values are easily seen to be the dc solutions. The ac equations are linearized by neglecting higher order $e^{j\omega t}$ terms. The resulting differential equation for the electric field is

$$\frac{d}{du_1} (h_2 h_3 E_1) - R_0 \varphi h_2 h_3 E_1 = - R_0 \psi I_1, \quad (1.4.4)$$

where

$$\varphi = \frac{\delta V_0}{AE_0} (1+j\omega\tau) \left[\frac{I_0}{E_0} + j\omega\epsilon A \right] h_1, \quad (1.4.4a)$$

$$\psi = \frac{\delta V_0}{AE_0} (1+j\omega\tau) h_1 h_2 h_3 \quad (1.4.4b)$$

and

$$R_0 = \frac{V_0}{I_0}.$$

The ac impedance Z_1 describing the double injection diode is subse-

quently determined by solving for the electric field and integrating this solution over u_1 (i.e. $V_1 = + \int_{R_1}^{R_2} E_1(u_1) du_1$) yielding (see Appendix B)

$$Z_1 = \frac{V_1}{I_1} = R_0 \int_{R_2}^{R_1} \left\{ \frac{\exp(R_0 \int \phi du_1)}{h_2 h_3} \left[\int_{R_2}^{u_1} \psi \exp(-R_0 \int \phi du_1) du_1 \right] \right\} du_1 \quad (1.4.5)$$

For the planar case ($h_1=h_2=h_3=1$), Eq.(1.4.5) takes the form

$$Z_1 = 3R_0(1+j\omega\tau) \int_0^1 du' \int_0^{u'} u' \left[\frac{u}{u'} \right]^{(1+j\omega\tau)} \exp[j\omega\Theta(1+j\omega\tau)(u-u')] du \quad (1.4.6)$$

where $\Theta = \frac{3}{2} R_0 C_0$ and C_0 is the geometrical capacitance. Here u and u' are dummy integration variables. Equation (1.4.6) is now evaluated for case (i) in which $\omega\Theta \ll 1$ and case (ii) where $\omega\Theta \gg 1$.

In case (i), the exponential term (Eq.(1.4.6)) is expanded in powers of $\omega\Theta$. Retaining terms of the order of $\omega\Theta$ and performing the integration gives

$$Z_1 \sim R_0 \frac{(1+j\omega\tau)}{(2+j\omega\tau)} \left[1 - \frac{j\omega\Theta 3}{4} \frac{(1+j\omega\tau)}{(3+j\omega\tau)} \right] \quad (1.4.7)$$

This expression for the ac impedance is synthesized into the equivalent circuit illustrated in Figure 1.4.1a and reduces to the circuit shown in Figure 1.4.1b when the geometrical capacitance C_0 and terms involving Θ/τ are considered negligible. At low frequencies ($\omega \ll 1/\tau$) the conductance is $g = 2/R_0 = \partial I/\partial V$, or just the dc differential conductance. Correspondingly, for high frequencies ($\omega \gg 1/\tau$, but $\omega \ll 1/\Theta$) the conductance is given by $g = 1/R_0$.

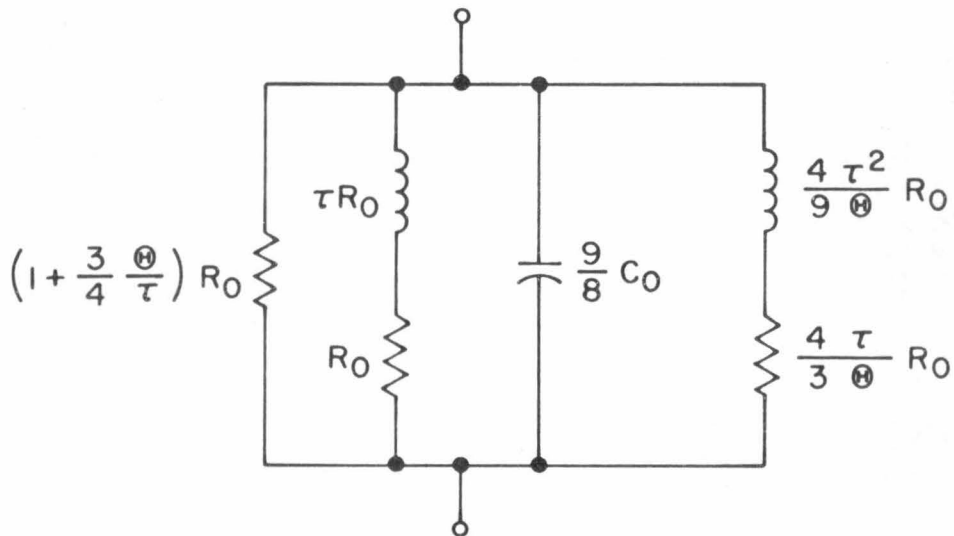


Figure 1.4.1a. Small signal ac equivalent circuit representation of a double injection diode in the semiconductor regime for frequencies less than $1/(2\pi\Theta)$ where $\Theta = \frac{3}{2} R_0 C_0$.

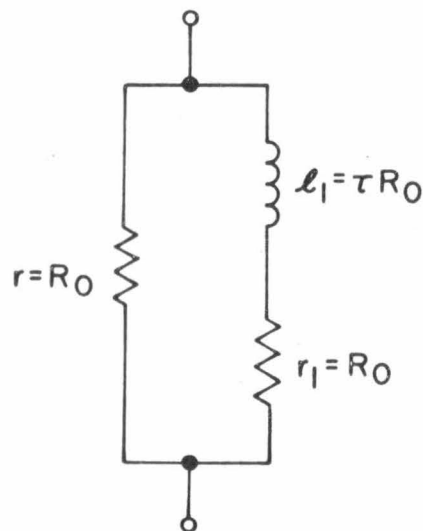


Figure 1.4.1b. First order small signal ac equivalent circuit as derived from Figure 1.4.1a when $\tau \gg \Theta$ and the geometrical capacitance C_0 is negligible.

These results are in agreement with the differential step response analysis of double injection given in Section 1.3. In fact, the current response of the first order ac equivalent circuit is just that of Eq.(1.3.6) and the high frequency behavior is given by $r = R_o$ (see Eq.(1.3.2)).

In case (ii), the integral is expanded in powers of $1/\omega\Theta$. The first two terms of the admittance are given by

$$Y_1 = \frac{4G_o}{3} + j\omega C_o \quad , \quad \omega \gg 1/\Theta \quad (1.4.8)$$

where $G_o = 1/R_o$. As R. Baron points out, the frequency is sufficiently high that (a) the space charge distribution cannot change thus, the capacitance becomes just the geometrical capacitance and (b) the conductance is given by the motion of the steady state carrier distribution in an excess electric field free of divergence. (1.17)

The first order equivalent circuit shown in Figure 1.4.1b is also valid for cylindrical double injection diodes.* However, the magnitude of the second order elements (components involving Θ in Figure 1.4.1a) are affected by geometrical factors. For frequencies $\omega \gg 1/\Theta$, the conductance ratio g/G_o of a cylindrical double injection structure is a function of the ratio of the radii which contrasts the result $g/G_o = 1$ for the frequency range $1/\tau < \omega < 1/\Theta$.

* A detailed discussion of the cylindrical case is presented in Appendix B.

Extension to the spherical case requires numerical methods; however, it is speculated that the first order equivalent circuit of Figure 1.4.1b is valid for this case also.

1.4.2. Experimental verification of Results. Experimental data demonstrating the validity of the first order equivalent circuit shown in Figure 1.4.1b are illustrated by the current response data of Figure 1.3.2. In order to test the validity of this equivalent circuit independently of the differential response, the real and imaginary parts of the diode admittance have been measured from 90Hz to 100MHz ($T = 298^{\circ}\text{K}$). These results are shown in Figures 1.4.2 and 1.4.3. Here, the dependences (solid lines) predicted from the first order equivalent circuit are given using a least squares fit. The agreement is quite good for frequencies between 90Hz and approximately 30MHz. Above 30MHz, the increasing conductance $\text{Re}(Y)$ (dashed lines) indicates that the approximation $\omega\tau \ll 1$ is no longer valid.* This is indeed the case since at the bias point of 30V, 1.6ma, the condition $\omega\tau = 1$ is satisfied at 33MHz. As a result, the conductance begins to increase towards the value of $(4/3) G_0$ for frequencies greater than 30MHz. In the differential step response data of Figure 1.3.2, bandwidth limitations of the measuring equipment precluded the detection of this effect.

In table 1.4.2, the values of r , ℓ_1 , and r_1 determined from the ac measurements are compared with those obtained from the differential step response at various operating points. The discrepancies

* In the frequency range from 30MHz to 100MHz, the errors in the conductance measurements which are obtained on a H.P. 250 RX bridge may be as large as 20%.

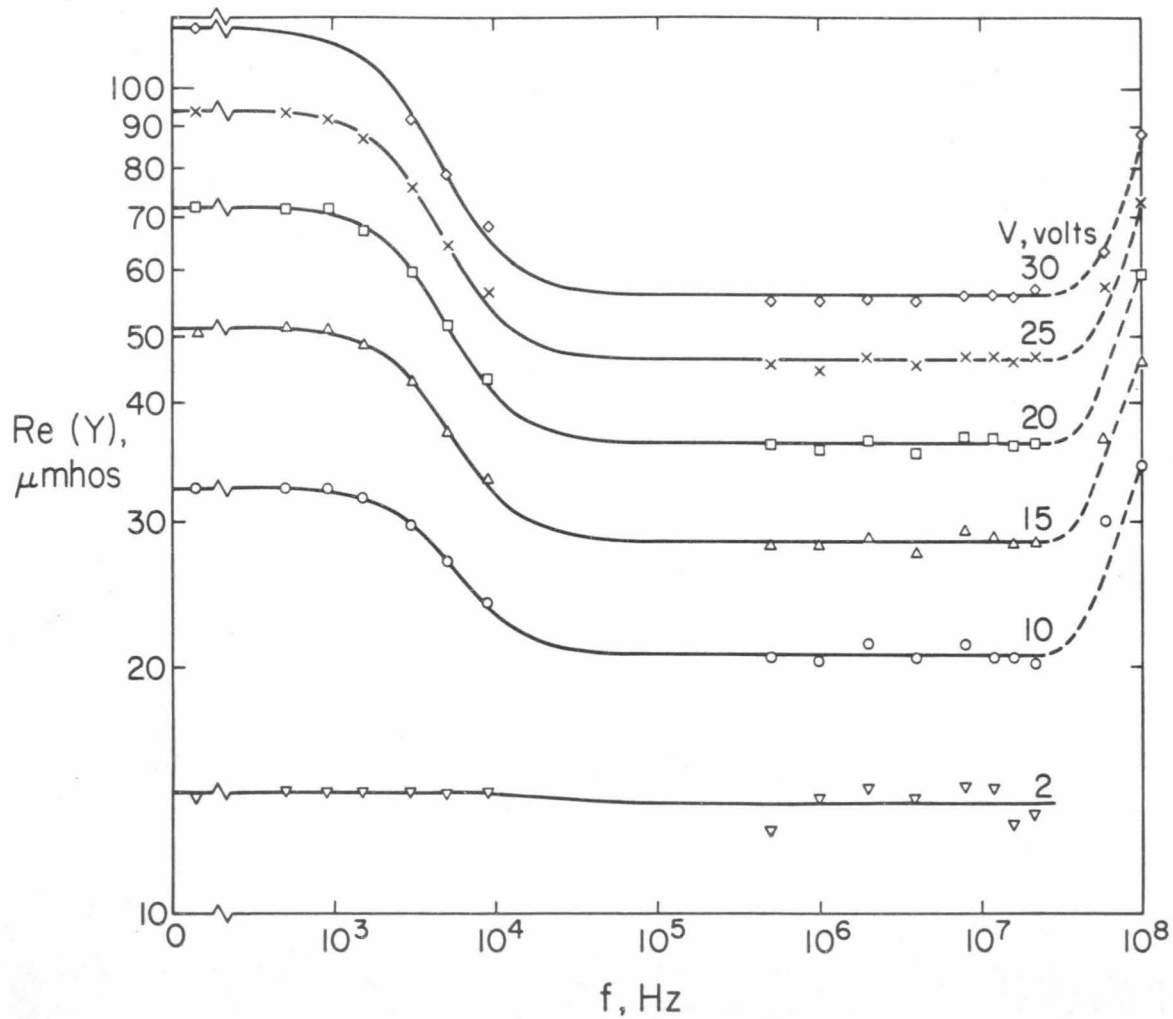


Figure 1.4.2. Real part of the diode admittance versus frequency. The solid lines are least-squares fits to the data. The fitting function is that derived from the equivalent circuit of Fig. 1.4.1b. The parameters obtained are given in Table 1.4.2.

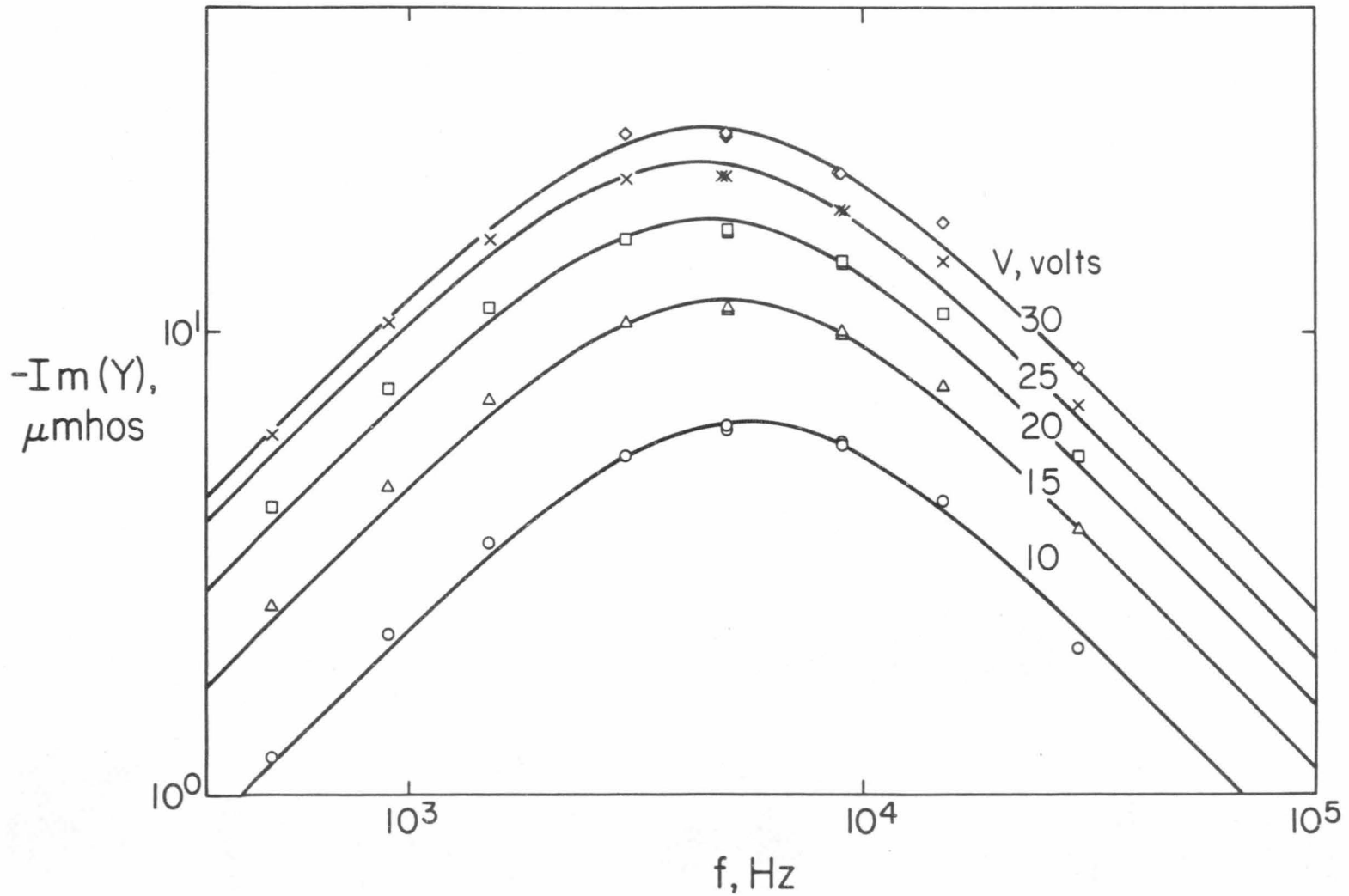


Figure 1.4.3. Imaginary part of the diode admittance versus frequency. The solid lines are least squares fits to the data. The fitting function is that derived from the equivalent circuit of Fig. 1.4.1b after subtraction of $\omega C = \text{Im}(Y)_{f \rightarrow \infty}$.

TABLE 1.4.2

Room temperature values of the parameters for the equivalent circuit of Figure 1.4.1b for the double injection diode of Figure 1.2.5.

Operating point		from step response			from frequency response				
V(V)	I(mA)	r(k Ω)	ℓ_1 (H)	r ₁ (k Ω)	Re(Y)			Im(Y)	
					r(k Ω)	ℓ_1 (Y)	r ₁ (k Ω)	ℓ_1 (Y)	r ₁ (k Ω)
30.0	1.60	18.1	0.70	18.5	17.8	0.69	16.8	0.63	17.9
25.0	1.12	21.2	0.83	22.5	21.4	0.86	21.2	0.80	21.4
20.0	0.710	26.7	1.08	29.7	27.0	1.08	28.7	1.01	28.5
15.0	0.405	34.5	1.54	43.5	35.4	1.52	43.5	1.39	42.5
10.0	0.196	47.1	2.4	81.9	48.7	2.6	81.4	2.3	78
2.0	0.024	68	--	--	73.5	--	--	--	--

nowhere exceed 10%. The large effective inductance (of the order of a henry) which increases as the operating point moves from the quadratic region towards the linear range is an especially interesting feature of double injection. Unfortunately, the Q , which is maximum at $f = 1/(2\pi\tau)$, is less than 1/2. Above 10V the ratios ℓ_1/r_1 for the lifetime τ all lie between 30μ sec. and 38μ sec. The simple first order equivalent circuit shown in Figure 1.4.1b thus adequately represents the small signal behavior of a double injection diode in the semiconductor regime from low frequencies up to over three decades above the transition point $\omega\tau = 1$.

When the ambient temperature of the device is monitored from 140°K to 350°K by means of a thermostat (see Appendix F), the transient and ac measurements are extended to six different temperatures. The solid dots displayed in the I-V characteristics of Figure 1.2.5 indicate the operating points at which these measurements are performed. Table 1.4.3 summarizes the results. Here, along with the measured lifetimes, the high frequency resistances as obtained by ac bridge measurements* are compared to the values determined from the differential step response. Agreement between these values is quite good for temperatures above 220°K , however, at the lower ambient temperatures ($T \leq 220^\circ\text{K}$) the difference is as large as 17%. This error at the lower temperatures is caused by an overshoot ($\leq 10\%$) in the step response at $t = 0^+$.

* Each value presented in Table 1.4.3 represents an average of eight measurements taken between 1MHz and 22MHz.

TABLE 1.4.3

Values of the high frequency resistance and high-level lifetime as a function of temperature for the double injection diode of Figure 1.2.5.

Temperature	Operating Point		r(k Ω) from frequency response	r(k Ω) from step response	τ (μ sec) from step response
	V(v)	I(ma)			
350 $^{\circ}$ K	40.0	2.10	17.4	17.4	44.9
	35.0	1.61	19.6	19.6	40.1
	25.0	0.868	26.8	27.0	39.9
	10.0	0.164	53.9	55.3	37.3
	2.0	0.023	77.6	77.0	39.5
298 $^{\circ}$ K	30.0	1.60	17.8	18.1	37.8
	25.0	1.12	21.4	21.2	35.9
	20.0	0.710	27.0	26.7	36.4
	15.0	0.405	35.4	34.5	35.4
	10.0	0.196	48.7	47.1	29.4
	2.0	0.024	73.5	68.0	-----
273 $^{\circ}$ K	25.0	1.35	18.5	18.5	26.3
	20.0	0.845	22.7	23.4	25.1
	15.0	0.480	30.8	30.8	23.5
	8.0	0.767	48.1	48.2	-----
	2.0	0.028	62.4	58.3	-----
220 $^{\circ}$ K	20.0	1.34	13.1	13.4	17.3
	17.5	1.02	15.1	15.4	16.9
	15.0	0.746	17.9	18.4	16.7
	6.0	0.160	31.2	26.2	-----
	2.0	0.037	37.4	36.8	-----
175 $^{\circ}$ K	17.5	1.58	7.9	8.3	11.0
	15.0	1.15	9.4	10.1	11.3
	12.5	0.800	11.0	12.0	10.8
	10.0	0.520	13.1	14.6	10.9
	5.0	0.170	17.8	20.8	9.2
140 $^{\circ}$ K	10.0	0.760	6.9	7.4	8.6
	8.0	0.510	7.9	8.3	8.0
	6.0	0.292	9.2	9.4	6.4
	4.0	0.145	10.2	10.4	-----

1.4.3. Nonlinear Effects. In deriving the small signal equivalent circuit for double injection, the nonlinear aspects of the diode are of course neglected. Moreover, the ac measurements used to verify the equivalent circuit are obtained with an impedance bridge which employs a frequency tuned detector, thus the nonlinear properties of the diode are also suppressed in the experimental case.

In order to investigate the nonlinearity, consider the double injection diode to be biased at V_o , I_o and let the sinusoidal voltage $v = v_1 \cos \omega t$ be applied across the diode. If the frequency is sufficiently low, the R.M.S. current will consist of a component at the applied frequency ω and a component at twice the fundamental frequency (i.e. 2ω). These components are given by

$$\langle i^2(\omega t) \rangle^{1/2} = 2\delta q \mu_n \mu_p (p_o - n_o) \tau V_o \bar{v}_1 \quad (1.4.9)$$

and

$$\langle i^2(2\omega t) \rangle^{1/2} = \sqrt{2} \delta q \mu_n \mu_p (p_o - n_o) \tau \bar{v}_1^2 \quad (1.4.10)$$

where $\bar{v}_1 = v_1/\sqrt{2}$. The ratio of these components,

$$\frac{\langle i^2(\omega t) \rangle^{1/2}}{\langle i^2(2\omega t) \rangle^{1/2}} = \frac{\sqrt{2} V_o}{\bar{v}_1}, \quad (1.4.11)$$

is independent of any physical properties of the device (i.e. geometry, doping, mobility, etc.) and the derivation only requires that the current-voltage characteristic be quadratic. From Eq.(1.4.11), the

second harmonic component of the current will be small when

$$\sqrt{2} V_o / \bar{v}_1 \gg 1.$$

The output of a signal generator operating at a frequency of 100Hz is applied to the double injection diode of Figure 1.2.5 which is biased at $V_o = 30\text{v}$ and $I_o = 1.6\text{ma}$ ($T = 298^\circ\text{K}$). In Figure 1.4.4, the measured R.M.S. current at the fundamental and the second harmonic frequencies is given as a function of the voltage \bar{v}_1 and \bar{v}_1^2 respectively. Here, the current component at the generator frequency (fundamental) is shown to be directly proportional to the R.M.S. value of the applied signal, whereas the second harmonic is proportional to the square of the applied R.M.S. signal. When the period of the applied ac signal is comparable or greater than the high-level lifetime τ , the magnitude of the second harmonic should decrease. The experimental data presented in Figure 1.4.5 demonstrate this attenuation of second harmonic generation of the diode as a function of frequency. Even though the nonlinearity under practical operating conditions is quite small (see Figure 1.4.4) it loses these properties altogether at sufficiently high frequencies. As a consequence, the small signal ac equivalent circuit of Figure 1.4.1b is also valid for large signals when the frequency is greater than $1/\tau$ as expected from the discussion of the transient response (Section 1.3).

1.5. High Frequency Noise in Double Injection Silicon Diodes.

1.5.1. Generalities. In performing the noise measurements, the unknown noise from the double injection diode is compared to that of a standard calibrator shot noise source. Schottky's theorem states that the shot noise developed across a temperature limited vacuum diode for

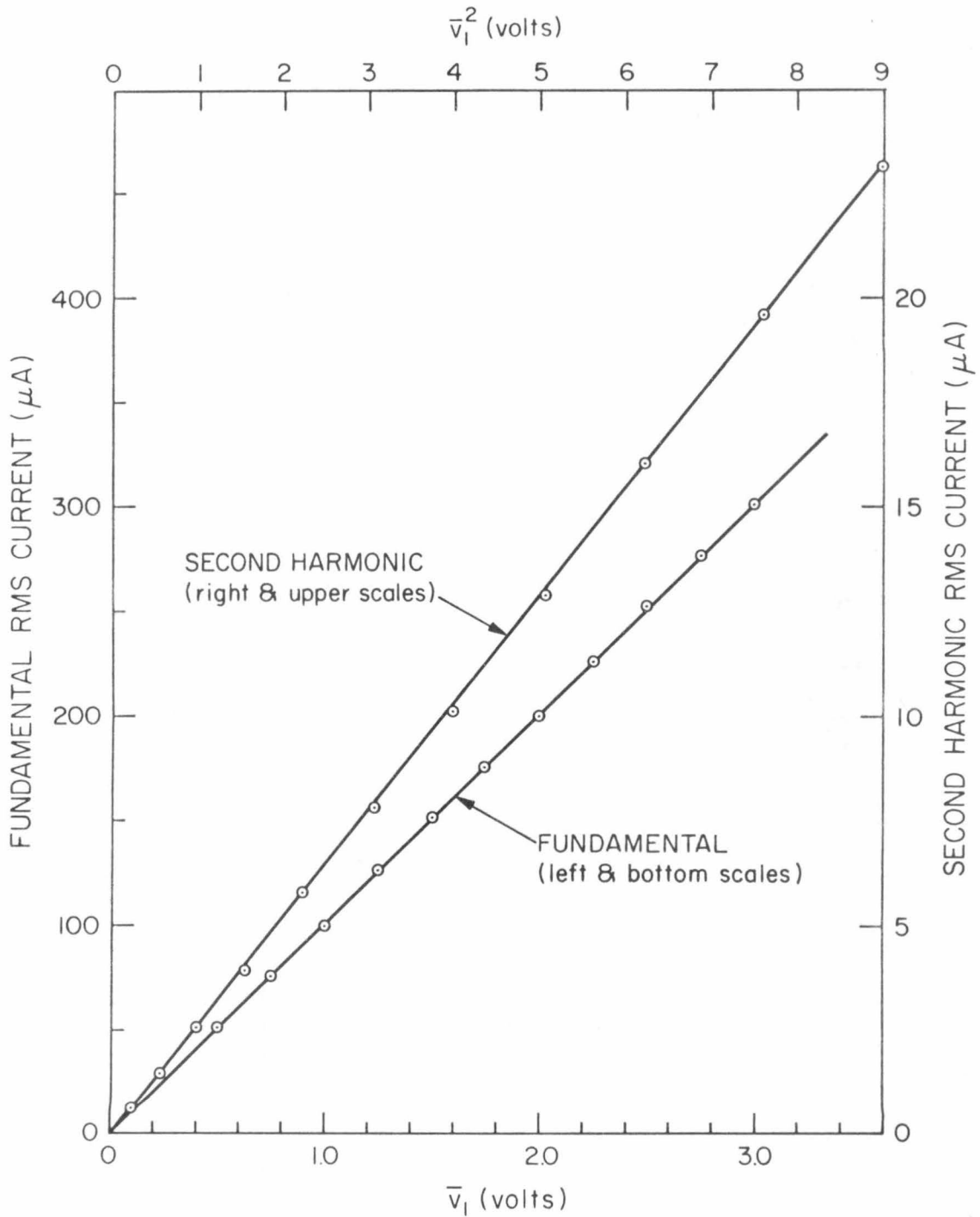


Figure 1.4.4. Fundamental and second harmonic ac current response of the double injection diode given in Figure 1.2.5. The data are corrected to account for the small amount of second harmonic content in the applied signal (H.P. 200CD generator).

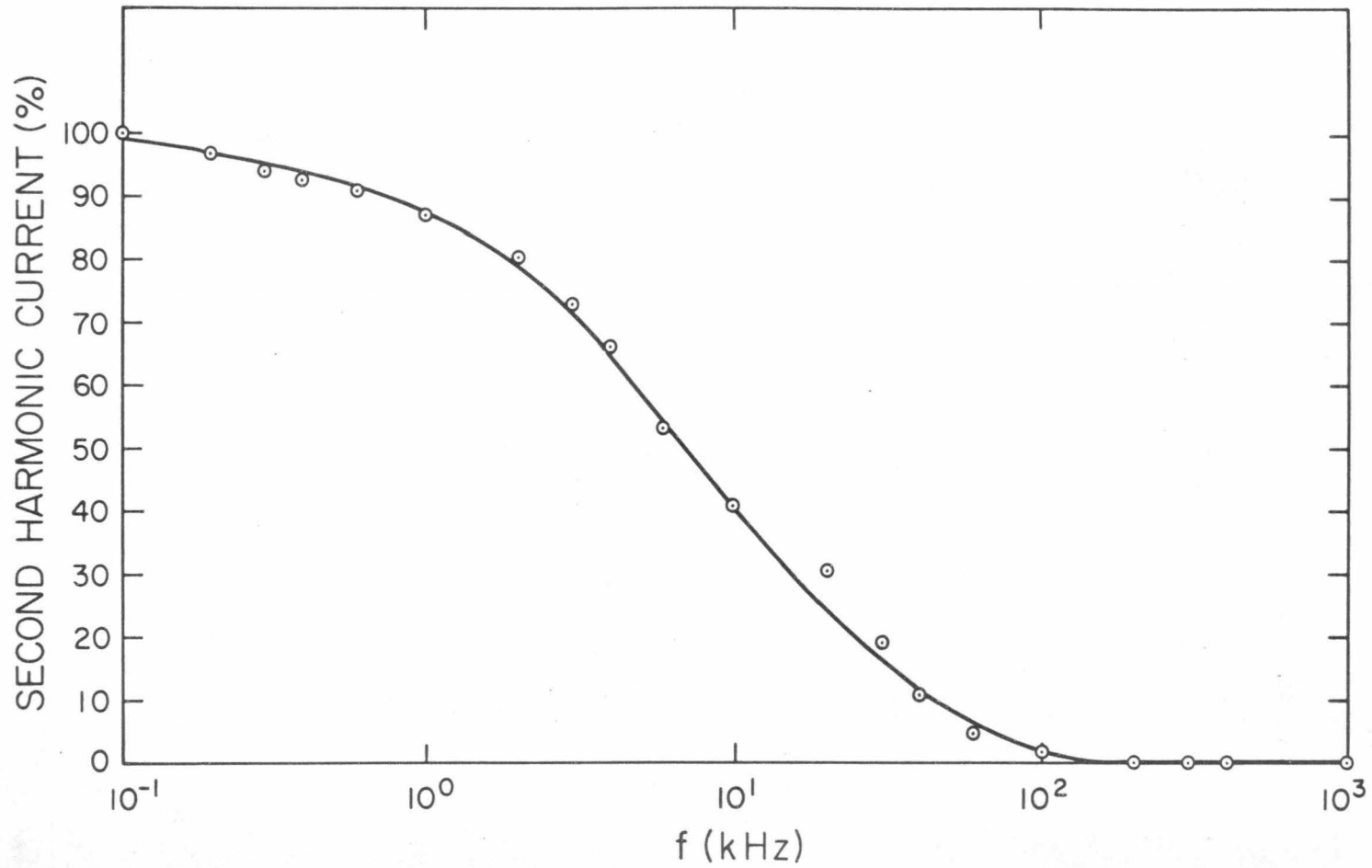


Figure 1.4.5. Percentage of second harmonic current as a function of frequency.

frequencies less than τ_T (τ_T is the carrier transit time) is given by

$$\langle i^2 \rangle = 2q I_c \Delta f , \quad (1.5.1)$$

where I_c is the dc operating current. (1.18) The experimental technique of comparing an unknown noise source to a known noise source provides an accurate means with which to obtain the noise spectral density of a two terminal device.*

Motivated by experimental evidence, a thermal noise hypothesis is introduced in discussing the high frequency fluctuation phenomena occurring in double injection. Recently, it has been deduced that the thermal noise in a passive resistance $R(f)$ at the ambient temperature T is represented by

$$\langle v^2 \rangle = 4 \int R(f) [hf/2 + hf/(\exp(hf/kT)-1)] df \quad (1.5.2)$$

where $\langle v^2 \rangle^{1/2}$ is the open circuit noise voltage fluctuation. (1.19)

When quantum mechanical effects are negligible (i.e. $hf \ll kT$)

Eq.(1.5.2) reduces to Nyquist's result

$$\langle v^2 \rangle = 4kT R \Delta f , \quad (1.5.3)$$

* A detailed description of the experimental arrangement, procedure, and calibration of the entire noise measurement system is contained in Appendix C through G.

where the frequency interval Δf is sufficiently small that the resistance $R(f)$ is constant over this bandwidth. "Thermal noise" is adopted here to refer also to quasithermal noise of quasilinear systems in which $\langle v^2 \rangle = 4kT r \Delta f$, where r is a linear element characterizing a (nonlinear) system which is not in true thermal equilibrium.

1.5.2. Model of High Frequency Noise in Double Injection. A model of the diode noise is now developed from the physical properties of the device. In the equivalent circuit shown in Figure 1.4.1b, the ℓ_1 - r_1 branch has a time constant τ_1 equal to the lifetime of the carriers (i.e. $\tau_1 = \tau$). This means, physically, that the recombination processes, which play a dominant role in establishing the static characteristic, are too slow to affect the current at frequencies $\omega \ll 1/\tau$. Thus, at high frequencies, the fluctuations are not affected by the recombination processes either.

The total high frequency noise voltage developed across the double injection diode arises from fluctuations associated with the junctions ($p^+ - n$, $n - n^+$) and the long high resistivity region.* Van der Ziel has shown that for a p-n junction with the I-V characteristic

$$I_d = I_s (\exp(qV/kT) - 1) \quad (1.5.4)$$

* Any noise associated with surface phenomena is considered negligible at high frequencies.

the noise voltage developed across the junction under forward bias ($V \gg kT/q$) is approximately^(1.20)

$$\langle v_j^2 \rangle \simeq 2kT(kT/qI_d) \Delta f \quad . \quad (1.5.5)$$

If the long high resistivity section of the double injection diode is assumed to exhibit only thermal noise at high frequencies, then one may further assume that the noise voltage developed across this region is of the order of

$$\langle v_\pi^2 \rangle \simeq 4kT(V_o/I_o) \Delta f \quad (1.5.6)$$

where V_o/I_o is the dc resistance of the diode. From Eqs.(1.5.5) and (1.5.6), the noise voltage developed across the injecting contacts will be negligible when the bias voltage V_o is much greater than kT/q (i.e. $V_o \gg 25\text{mv}$ at 298°K). From Figure 1.2.5, this condition is fulfilled for all cases in which the diode is operating in the semiconductor regime ($V_o > 10\text{v}$).

When the diode is forward biased into the quadratic range, it is not in strict thermal equilibrium. If, regardless of conduction, (i) there is a stationary distribution of thermal velocities and (ii) this distribution involves only a small perturbation of the distribution from a Maxwellian, the diode can be considered to be in a state of quasithermal equilibrium. Since the thermal velocity of the charge carriers ($\sim 10^7$ cm/s) is, in the present case, much greater than the drift velocity ($\sim 7 \times 10^4$ cm/s), this picture of quasithermal

equilibrium appears quite justifiable for double injection. With this "thermal hypothesis", the high frequency noise current of the double injection then becomes simply

$$\langle i^2 \rangle = 4kT g \Delta f \quad (1.5.7)$$

where g is the conductance of the diode at high frequencies. In terms of an equivalent saturated shot noise diode current (I_{eq}), the noise spectral density is given by (see also Appendix C)

$$I_{eq} = \frac{2kT}{q} g . \quad (1.5.8)$$

Using the high frequency conductance of the diode derived in Section 1.4, the equivalent noise current of double injection is thus given by Eq.(1.5.8) where

$$g \approx \frac{I_0}{V_0} , \quad 1/\tau < \omega < 1/\theta \quad (1.5.8a)$$

and

$$g \approx \frac{4}{3} \frac{I_0}{V_0} , \quad 1/\theta < \omega < 1/\tau_c \quad (1.5.8b)$$

(τ_c is the mean time between thermal scatterings).

A different approach to the explanation of the high frequency noise is developed from the transient response. Here, the current step $\Delta i(0)$ is determined by the electron and hole concentrations n and p immediately before the voltage step Δv is applied. Electrons

and holes contribute independently to the flow at that instant and without changing their concentration. Van der Ziel and van Vliet proved recently that carriers of a single type injected into a volume element of a device will generate thermal noise. If, however, recombination is the only mechanism coupling the holes to the electrons and becomes ineffective at $\omega \gg 1/\tau$, van der Ziel and van Vliet's results applies to both electrons and holes independently. One must then expect

$$\langle i^2 \rangle = 4kT[A \sigma_n(\omega)/L + A \sigma_p(\omega)/L] \Delta f \quad (1.5.9)$$

$$= 4kT g \Delta f \quad 1/\tau < \omega < 1/\theta \quad . \quad (1.5.10)$$

This result is in agreement with Eq.(1.5.8).

Figure 1.5.1 summarizes the noise spectral density of a planar double injection diode based on the thermal hypothesis for frequencies greater than $1/\tau$.

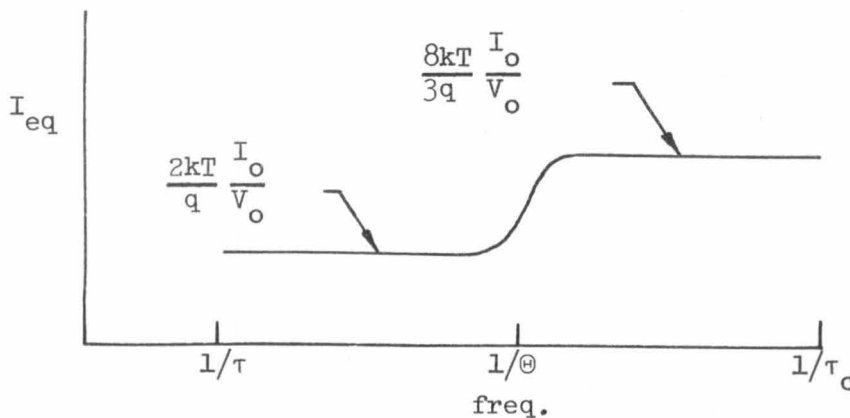


Figure 1.5.1. Equivalent noise current versus frequency for a planar double injection diode.

Since the first order equivalent circuit given in Figure 1.4.1b is independent of diode geometry, the equivalent noise current for the cylindrical and spherical geometries in the frequency range $1/\tau < \omega < 1/\theta$ is also given by Eqs.(1.5.8) and (1.5.8a) (see Appendix B). However, for the frequency range $1/\theta < \omega < 1/\tau_c$, the value of the diode conductance and thus the equivalent noise current will, in general, depend upon geometrical terms.*

1.5.3. Measured Spectral Noise Density. The measured dc characteristics and ac properties of the diode described in Figure 1.2.5 have been shown in Sections 1.2, 1.3 and 1.4 to closely conform to the predictions of the model for double injection. Thus, this double injection silicon diode provides a sound basis with which to test the thermal noise theory presented in Section 1.5.2.

To compare this theoretical model with the actual experimental noise of the device the measurements should cover as wide a frequency range as possible. This not only extends the amount of information but also helps minimize the possibility of systematic errors. From the conductance measurements illustrated in Figure 1.4.2, the ideal frequency range over which the spectral density should be measured extends from 500Hz to over 50 MHz. It is quite difficult to perform noise measurements over five decades of frequency and still optimize

* The functional dependence of the conductance g on the geometrical factors for the cylindrical double injection configuration is given in Appendix B.

the apparatus (impedance, system noise, etc.) to yield the maximum amount of information about the noise of the device. Nevertheless, with the measurement system described in Appendix C through G, the equivalent noise current of the device can be obtained from 10kHz to 22MHz. Provision in the experimental arrangement allows variation of the ambient temperature of the device and thus extends the noise measurements over a factor of two in absolute temperature.

The solid dots displayed in the I-V characteristics of Figure 1.2.5 indicate the operating points at which the noise measurements (and conductance) are performed. There is at least one point at every temperature where the diode is operating in the quadratic range. Figures 1.5.2a, b, c, d, e, f show the spectra in terms of an equivalent noise current for the temperatures 350, 298, 273, 220, 175 and 140°K. It is seen that at all operating points and for all temperatures the noise spectra reach a constant level. The solid lines have been obtained by the least squares fitting of an assumed dependence

$$I_{eq} = C_1 + \frac{C_2}{\left[\frac{C_3}{f} \right]} \quad (1.5.11)$$

to the data as described in Appendix G. At 140°K, the low frequency noise is attenuated for the 10v and 8v spectra to prevent amplifier saturation. This is accomplished by the insertion, at the amplifier input, of an L-C network which is tunable from 5MHz to 22MHz (see Appendix D).

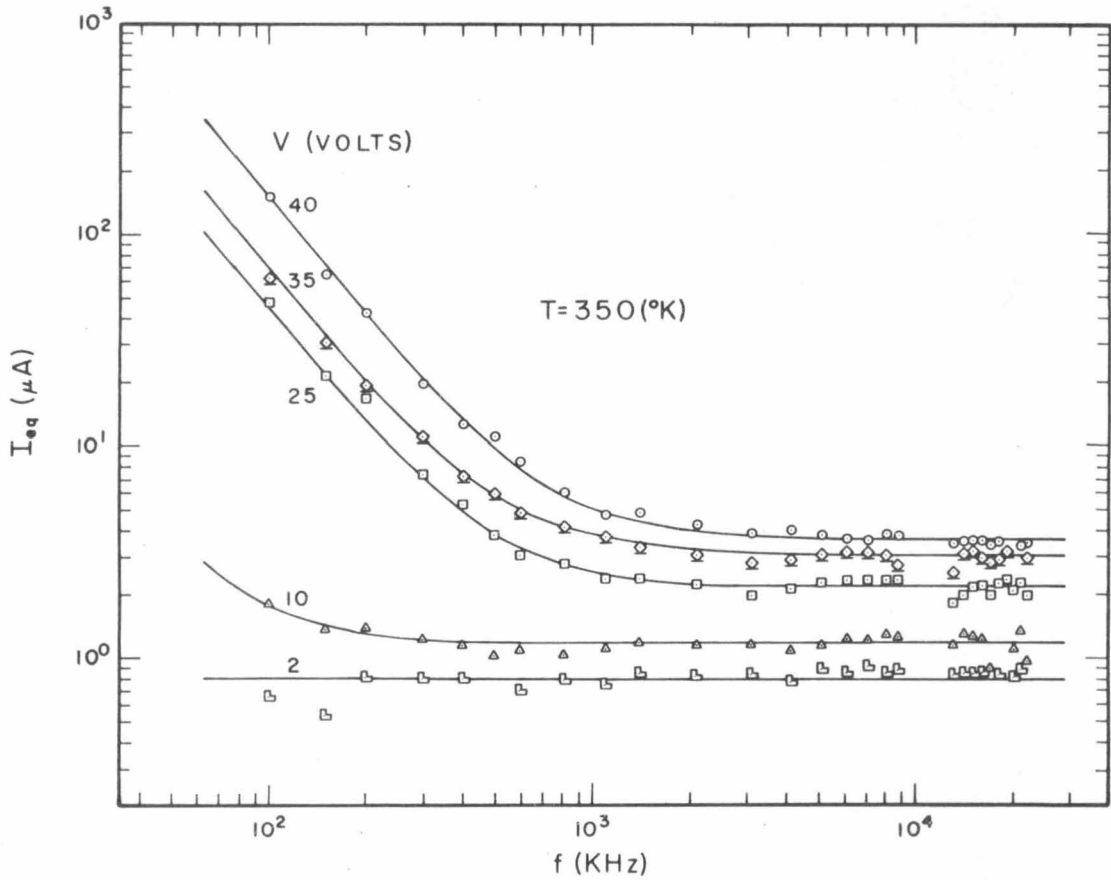


Figure 1.5.2a. Equivalent noise current (I_{eq}) versus frequency at five operating points for the double injection silicon diode given in Figure 1.2.5. ($T = 350$ K).

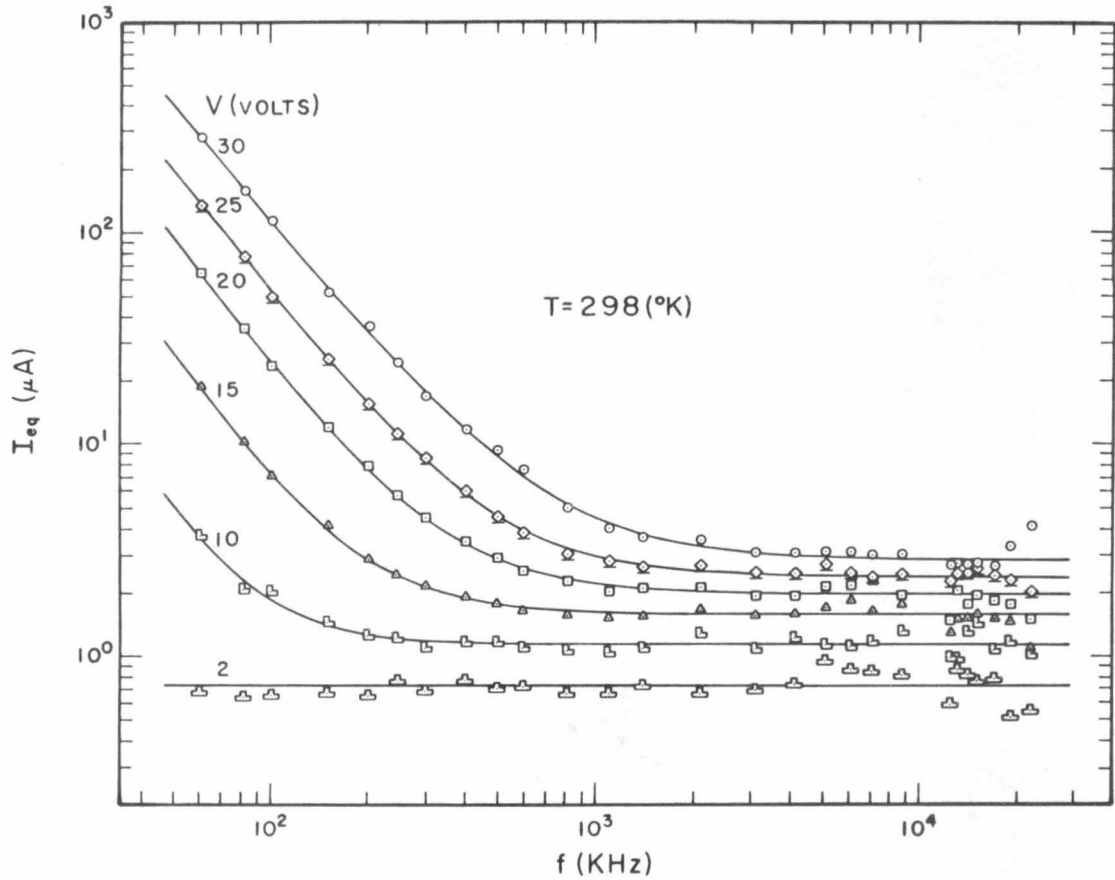


Figure 1.5.2b. Equivalent noise current (I_{eq}) versus frequency at six operating points for the double injection silicon diode given in Figure 1.2.5. ($T = 298^\circ\text{K}$).

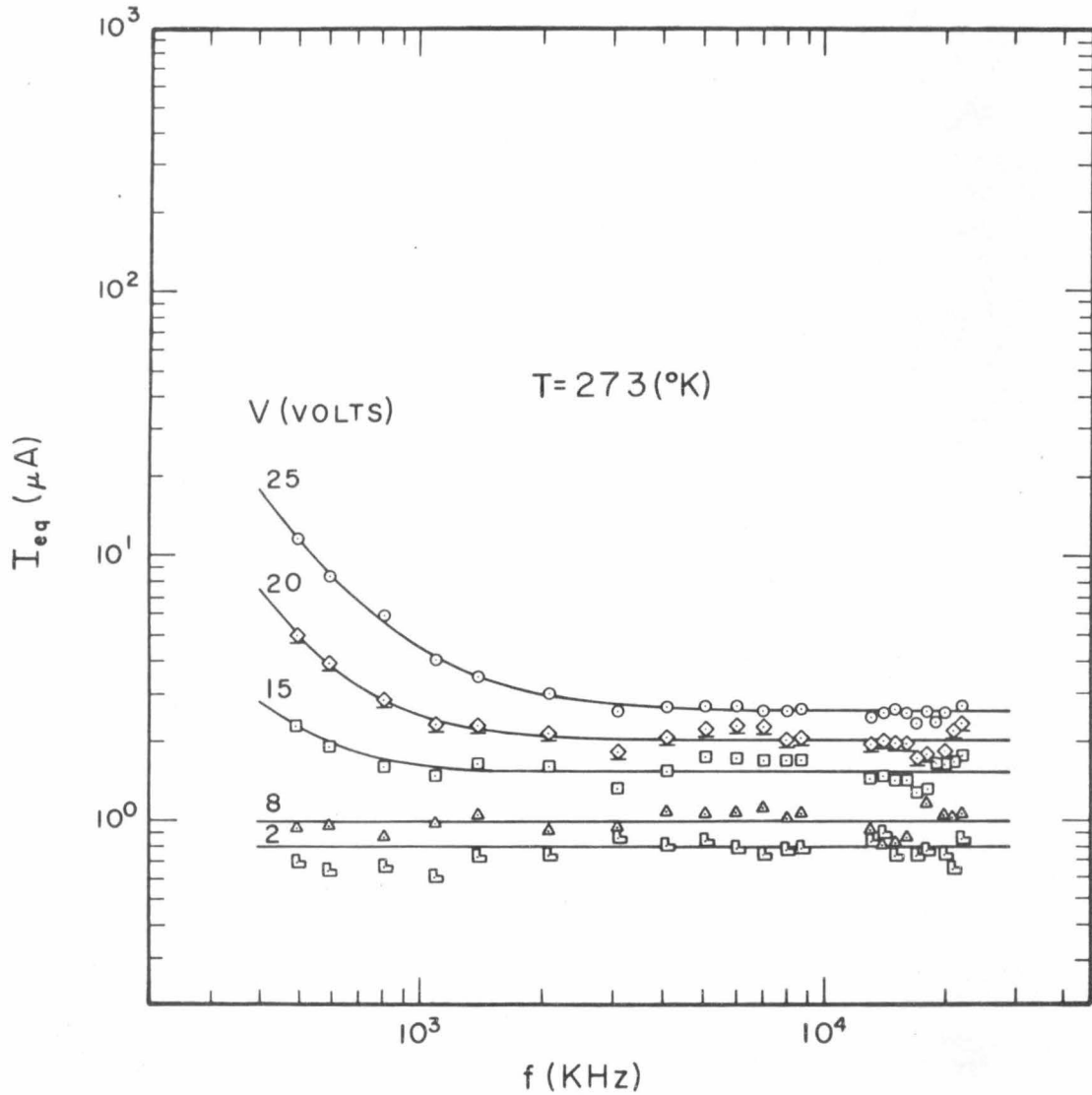


Figure 1.5.2c. Equivalent noise current (I_{eq}) versus frequency at five operating points for the double injection silicon diode given in Figure 1.2.5 ($T = 273^{\circ}\text{K}$).

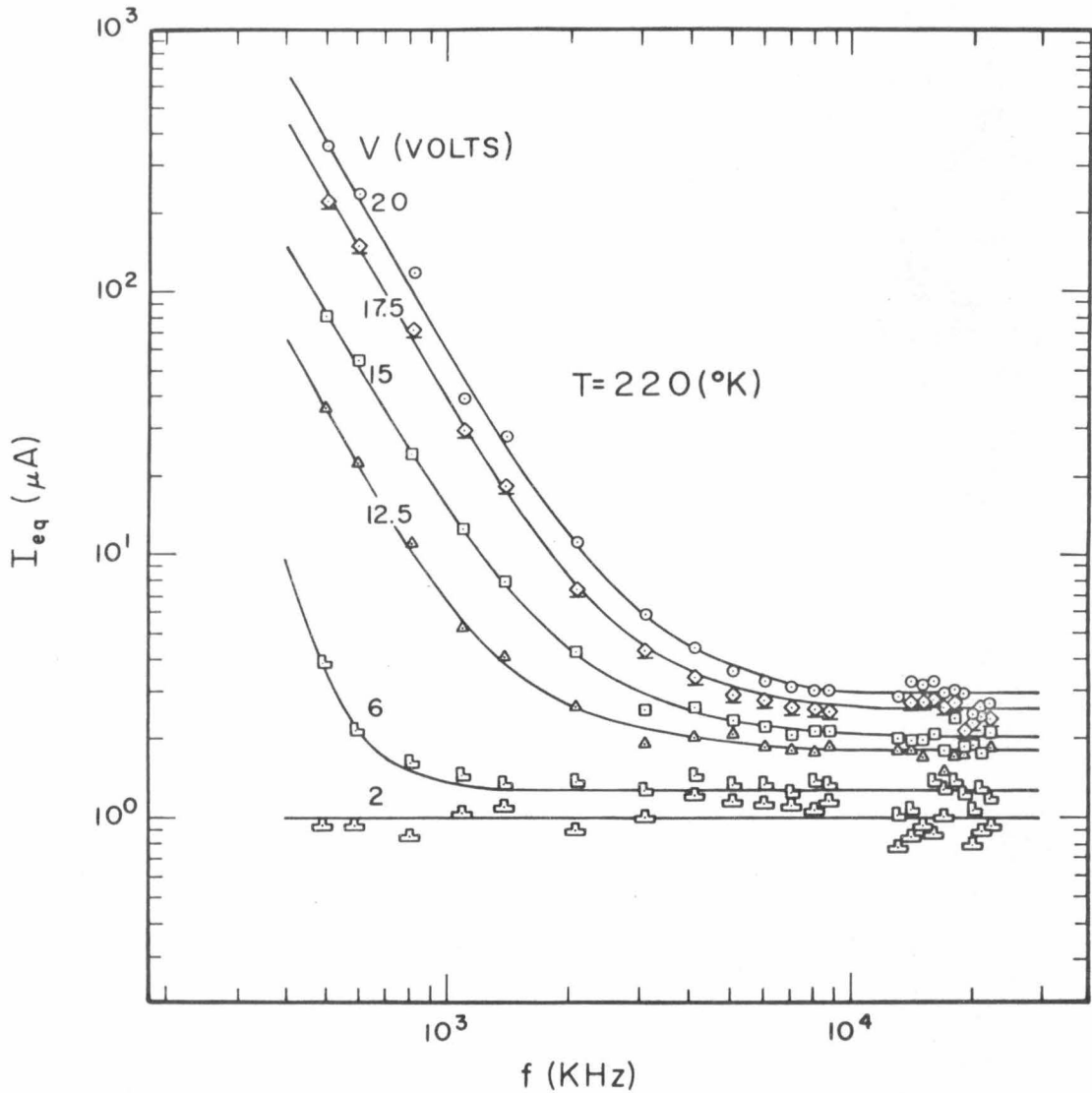


Figure 1.5.2d. Equivalent noise current (I_{eq}) versus frequency at six operating points for the double injection silicon diode given Figure 1.2.5 ($T = 220^\circ K$).

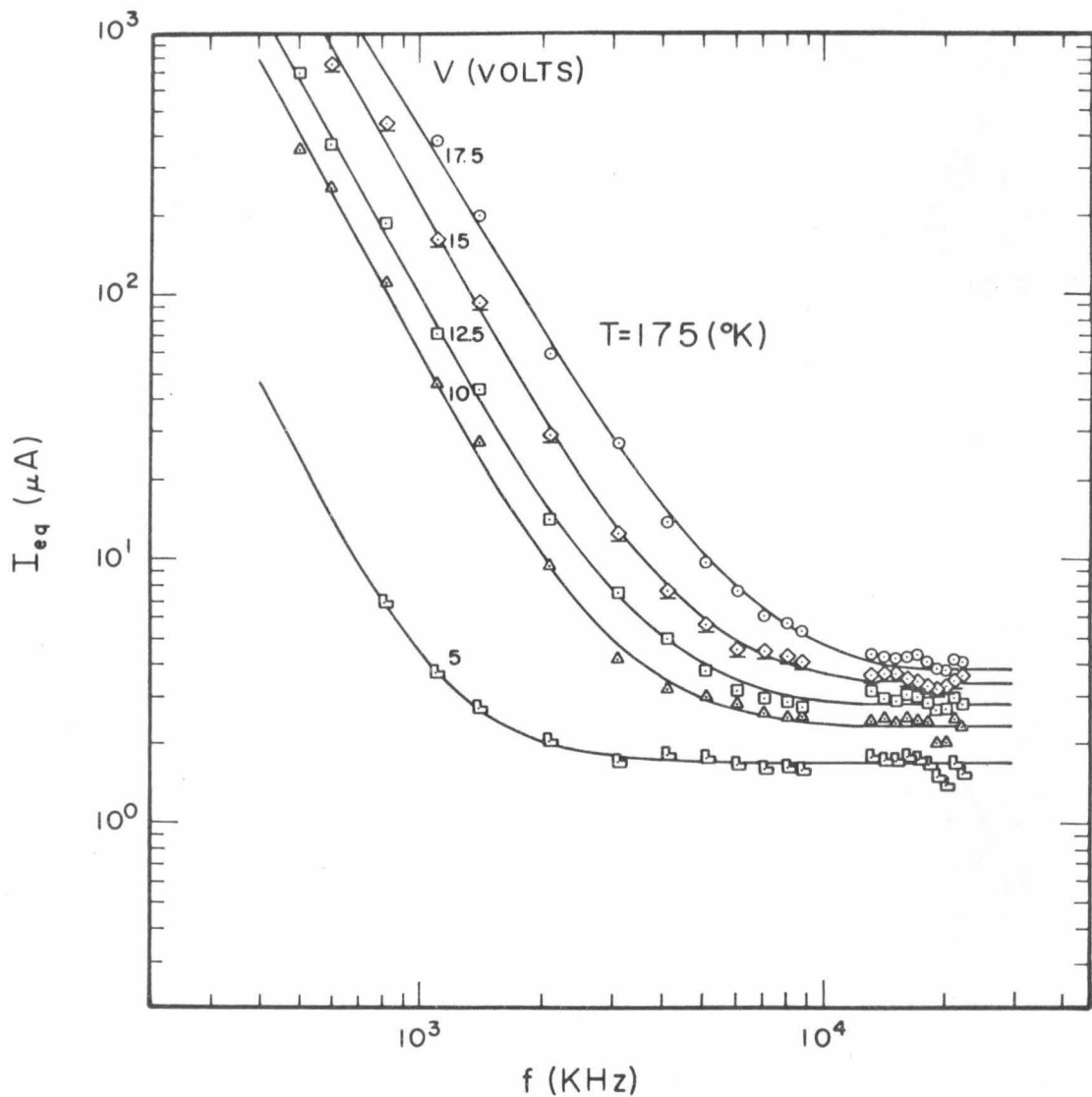


Figure 1.5.2e. Equivalent noise current (I_{eq}) versus frequency at five operating points for the double injection silicon diode given in Figure 1.2.5 ($T = 175^\circ\text{K}$).

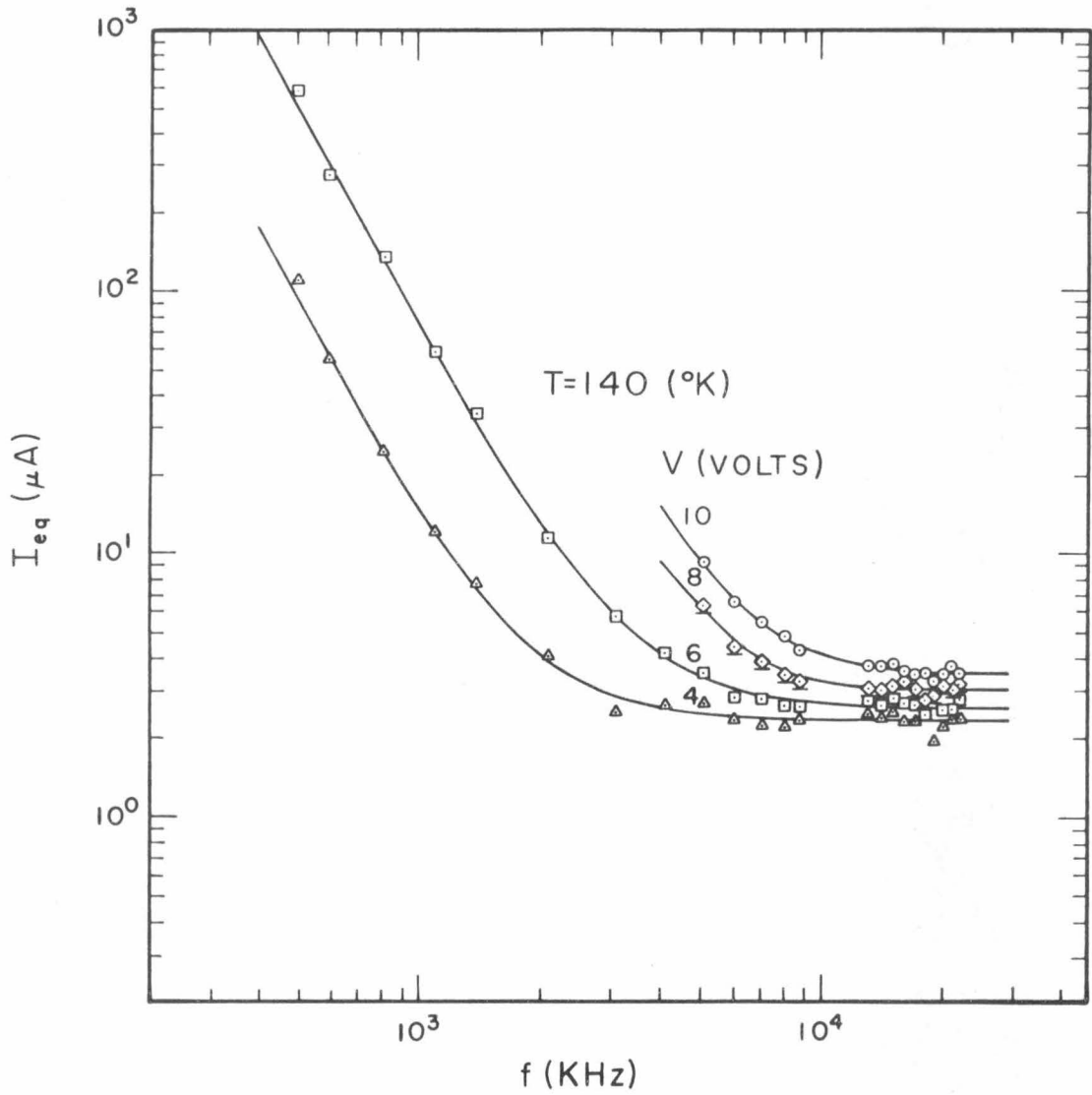


Figure 1.5.2f. Equivalent noise current (I_{eq}) versus frequency at four operating points for the double injection silicon diode given in Figure 1.2.5 ($T = 140^{\circ}\text{K}$).

1.6. Evaluation of Results and Conclusion. From the constant C_1 of Eq.(1.5.11), the measured equivalent noise resistance of the diode is given by

$$r_{eq} = \frac{2kT}{qC_1} . \quad (1.6.1)$$

Table 1.6.1 compares the values of r_{eq} determined from the noise measurement with the high frequency resistance r of the diode for each operating point and over a temperature range from 140°K to 350°K. Here, the high frequency resistance r is measured throughout the frequency range in which the equivalent noise current is constant and corresponds to the values "from the frequency response" in Table 1.4.3. The very close agreement between r_{eq} and the real part r of the diode impedance at high frequencies indicates that

$$\langle i^2 \rangle = \alpha \cdot 4kT g \Delta f \quad (1.6.2)$$

with α close to unity and $g = 1/r$. A better estimate of the value for α is obtained from a plot of the experimental values of I_{eq} versus g as a function of ambient temperature as shown in Figure 1.6.1. Also shown there (dashed lines) are the dependencies predicted from the equation

$$I_{eq} = \frac{2kT}{q} g . \quad (1.6.3)$$

The ratios of the experimental values of I_{eq} to this predicted value

TABLE 1.6.1

Comparison of the real part r of the diode impedance with the equivalent noise resistance r_{eq} at high frequencies.

Temperature	Operating Point		r (k Ω)	r_{eq} (k Ω)
	V(v)	I(ma)		
350 $^{\circ}$ K	40.0	2.10	17.4	16.6
	35.0	1.61	19.6	19.9
	25.0	0.868	26.8	27.7
	10.0	0.164	53.9	51.6
	2.0	0.023	77.6	74.3
298 $^{\circ}$ K	30.0	1.60	17.8	18.0
	25.0	1.12	21.4	21.6
	20.0	0.710	27.0	26.1
	15.0	0.405	35.4	32.6
	10.0	0.196	48.7	45.1
	2.0	0.024	73.5	70.5
273 $^{\circ}$ K	25.0	1.35	18.5	18.3
	20.0	0.845	22.7	23.5
	15.0	0.480	30.8	30.4
	8.0	0.767	48.1	47.6
	2.0	0.028	62.4	59.6
220 $^{\circ}$ K	20.0	1.34	13.1	13.1
	17.5	1.02	15.1	15.1
	15.0	0.746	17.9	19.1
	6.0	0.160	31.2	30.4
	2.0	0.037	37.4	38.0
175 $^{\circ}$ K	17.5	1.58	7.4	8.2
	15.0	1.15	9.4	8.9
	12.5	0.800	11.0	10.9
	10.0	0.520	13.1	13.3
	5.0	0.170	17.8	18.1
140 $^{\circ}$ K	10.0	0.760	6.9	6.9
	8.0	0.510	7.9	7.9
	6.0	0.292	9.2	9.3
	4.0	0.145	10.2	10.3

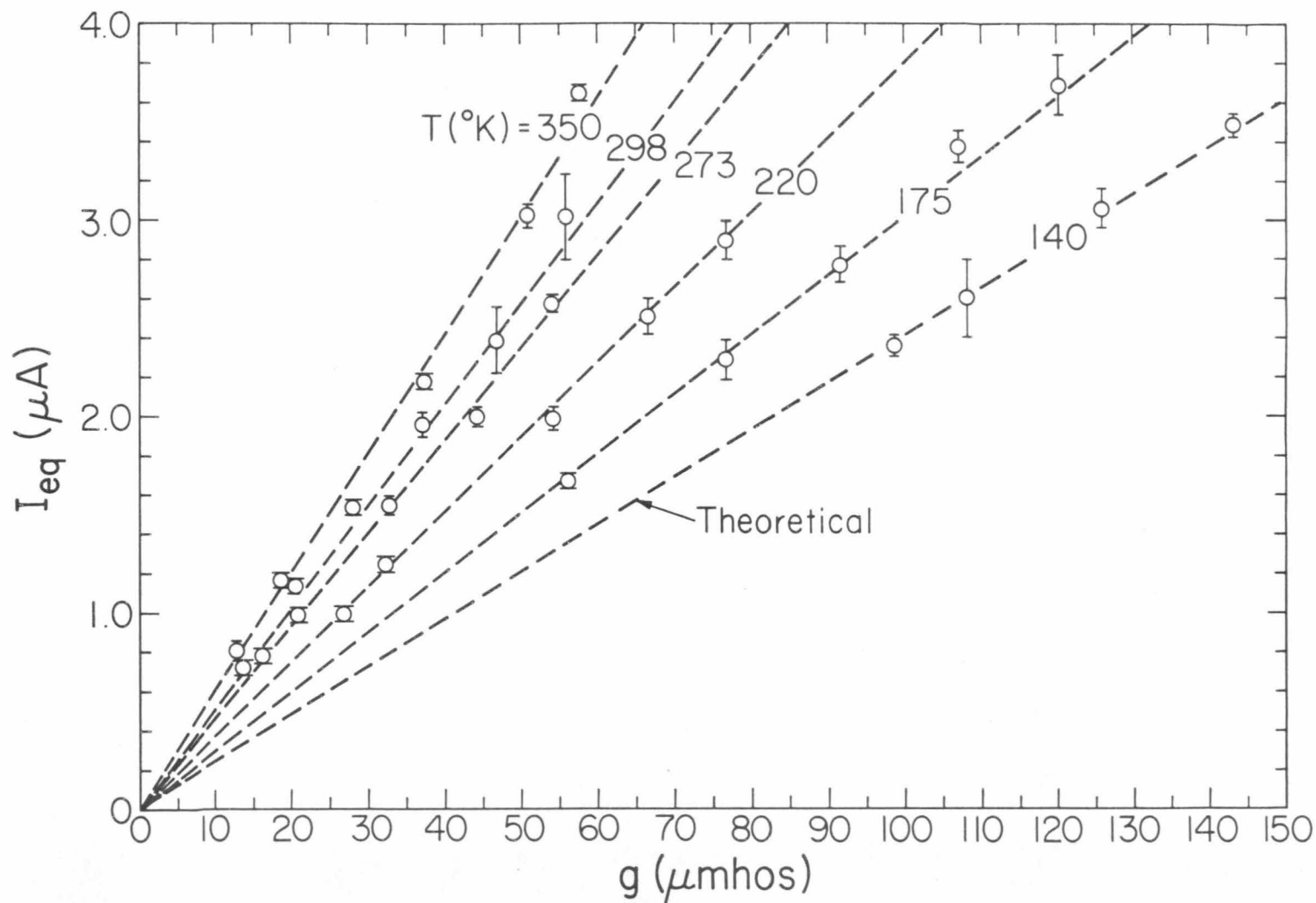


Figure 1.6.1. Equivalent noise current (I_{eq}) versus the high frequency conductance of the silicon double injection diode at the operating points indicated in Figure 1.2.5.

of $\frac{2kT}{q} g$ (i.e. α) have been evaluated by least squares fits as 1.00, 1.00, 1.01, 1.01, 1.04, and 1.03 ± 0.05 for 140, 175, 220, 273, 298 and 350°K respectively. This established that $\alpha \equiv 1$ to within 5% and thus the high frequency noise is given by

$$\langle i^2 \rangle = 4kT g \Delta f \quad , \quad 1/\tau < \omega < 1/\theta \quad (1.6.4)$$

where $140^\circ\text{K} \leq T \leq 350^\circ\text{K}$ and g is the high frequency conductance of the device at the lattice temperature T . The quoted error of 5% is attributable to experimental causes, as indicated by the errors of individual values of r_{eq}^* . It is also noted that for a given temperature the thermal noise expression (Eq.(1.6.4)) is valid for every operating point, even where the square law does not hold. This again agrees with the idea of thermal noise. The overall conclusion is therefore drawn that Eq.(1.6.4) describes the noise of double injection accurately as long as recombination effects and diffusion are negligible. The thermal noise current source $\langle i^2 \rangle = 4kT g \Delta f$ in the first order equivalent circuit shown in Figure 1.6.2 expresses these ideas formally.

At lower frequencies, the equivalent noise currents as illustrated in the spectra of Figures 1.5.2, etc., have a "1/f" frequency dependence. Prompted by these results, Bilger, et al, have investigated the low

* The error associated with the determination of C_1 at each of the six ambient temperatures is an R.M.S. deviation σ_1 of the fitted curve from the data (see Appendix G) and is generally less than 1%. Since the error in the lattice temperature of the diode is of the order of 3%, the stated error of 5% is a conservative estimate.

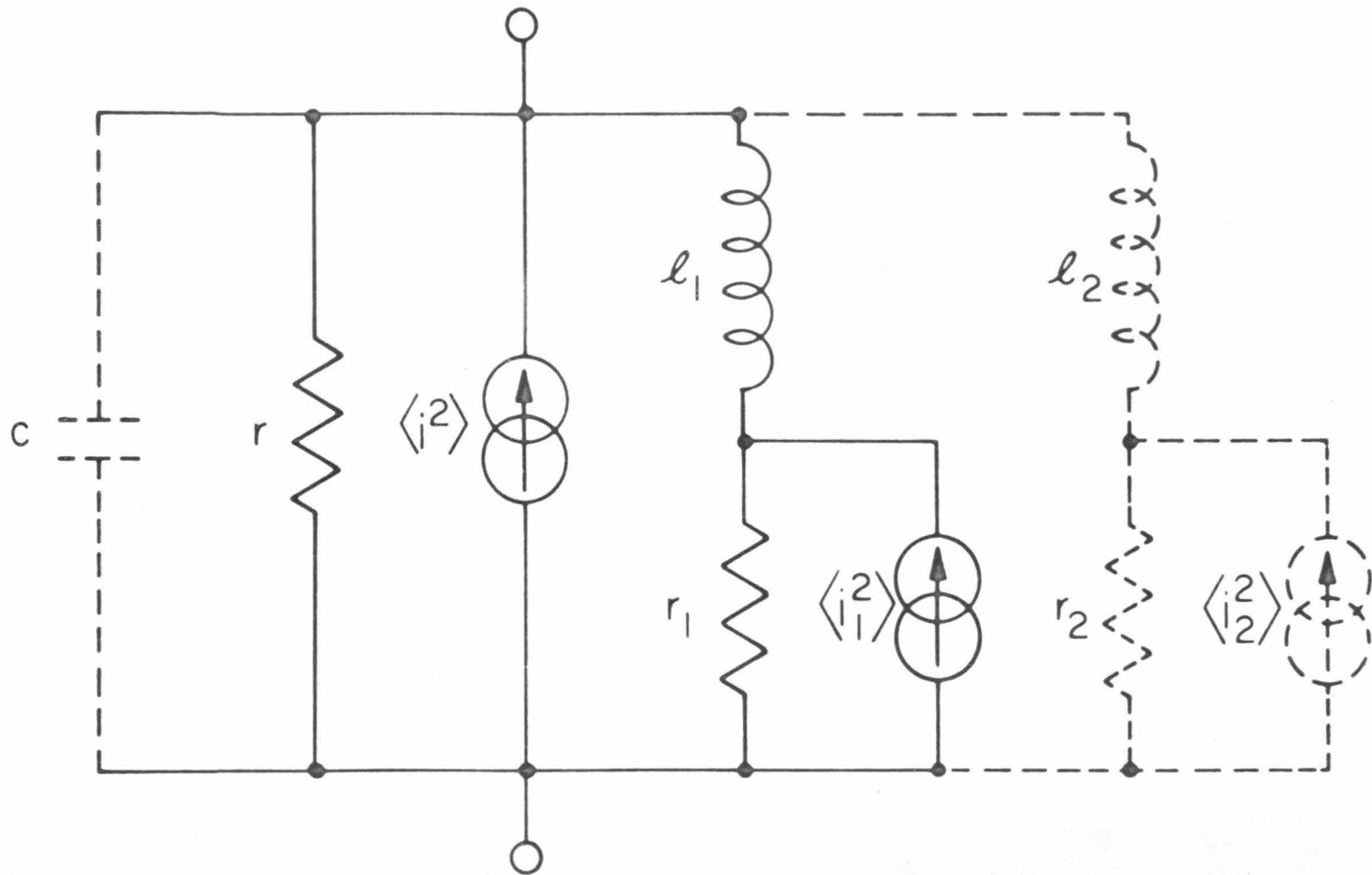


Figure 1.6.2. Equivalent circuit containing internal noise sources of a double injection diode operating in the semiconductor regime.

frequency noise of a $p^+ \nu n^+$ structure down to a few hertz. (1.22)

The spectra reveal qualitatively that the noise can be explained for frequencies $\omega \ll 1/\tau$ in terms of generation-recombination (g-r) effects. Therefore, in the equivalent circuit of Figure 1.6.2, this effect can be formally expressed by associating $\langle i_1^2 \rangle$ and $\langle i_2^2 \rangle$ with g-r noise.* Figure 1.6.3 shows the g-r equivalent noise current $I_{eq,g-r}$ measured at 100kHz as a function of the double injection diode current I .** It is noted, however, that the noise measurements presented in Figure 1.6.3 are not obtained with currentless probe contacts which eliminate unwanted contact noise; therefore, the absolute magnitude of the g-r noise may be in error.

1.7. Discussion and Outlook. The conclusion that $\langle i^2 \rangle = 4kT g \Delta f$ at $1/\tau < \omega < 1/\theta$ necessitates the rejection of alternative theories advanced to explain high frequency noise in double injection. (1.23, 1.24, 1.25) According to van der Ziel

$$\langle i^2 \rangle = \alpha \cdot 4kT g \Delta f \quad (1.7.1)$$

* A careful experimental analysis revealed traces of a second time constant τ_2 of about $1/4 \tau_1$, but the effect was judged to be sufficiently small to be neglected.

** The low-frequency double injection current noise theory of A. Fazakas and A. Friedman predicts (1.23) $I_{eq,g-r} \propto I^2$. Reference 1.22, however, predicts $I_{eq,g-r} \propto I^{3/2}$ for diodes operating in the semiconductor regime.

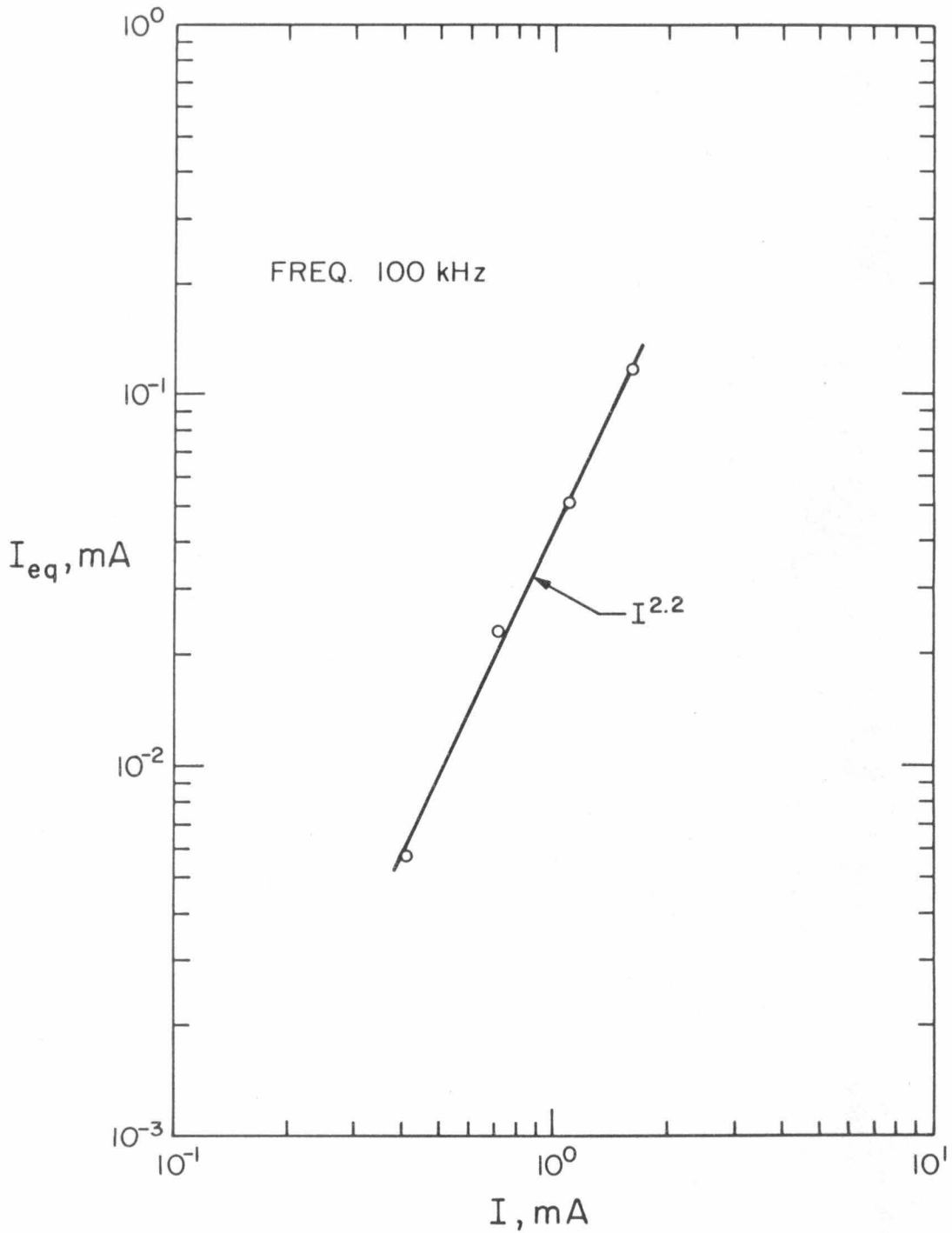


Figure 1.6.3. Observed g-r noise at 100kHz versus diode current at four operating points ($T = 298^{\circ}\text{K}$).

where

$$\alpha = \frac{4\mu_p \mu_n}{(\mu_p + \mu_n)^2} \quad . \quad (1.7.1a)$$

From the measured temperature dependencies of the electron mobility $\mu_n (\mu_n \propto T^{-1.75})$ and the hole mobility $\mu_p (\mu_p \propto T^{-2.18})$ of the silicon double injection diode presented in Chapter II, the representation $\alpha = 4\mu_p \mu_n / (\mu_p + \mu_n)^2$ must be rejected because it is inconsistent with the result $\alpha = 1.00 \pm .05$ throughout the temperature range from 140°K to 350°K . Other reported noise measurements, although difficult to cast into the light of an ac equivalent circuit owing to the lack of experimental data, are in agreement with the thermal noise model as expressed by Eq.(1.6.4.)* (1.1, 1.2, 1.3) However, the recent experimental results of J. H. Liao on a germanium $p^+ \nu n^+$ structure seem to indicate that van der Ziel's result (Eqs.(1.7.1), (1.7.1a)) is correct at $T = 298^\circ\text{K}$. (1.25) Unfortunately, insufficient data on the dc characteristics and high frequency properties of the device preclude the verification of semiconductor regime double injection.**

* Since the correct relationship between the low frequency conductance G_0 and the high frequency conductance g is $g = \frac{1}{2} G_0$, the term "noise suppression" of Ref. 1.3 is not appropriate in double injection as long as it refers to thermal noise.

** The germanium diode reported on by Liao exhibits an $I \propto V^2$ from approximately 0.1v to 0.5v. The observed noise, therefore, may be largely influenced by diffusion and contact effects.

There is no physical reason why the noise should not be thermal for frequencies above $1/\theta$ since this characteristic time pertains to the macroscopic phenomenon of dielectric relaxation. One thus expects that Eq.(1.6.4) is valid at least up to frequencies of the order of $1/\tau_c$. Moreover, there is no physical reason why the noise should not be thermal for temperatures above 350°K and below 140°K as long as the double injection diode can be characterized by the Lampert model. Therefore, when recombination and diffusion effects are negligible, it is predicted that the thermal noise model for double injection given by $\langle i^2 \rangle = 4kT g \Delta f$ holds for any double injection device at any temperature and for all operating points over the frequency range $1/\tau < \omega < 1/\tau_c$.

Extension to various diode geometries is accomplished through the relationship between the geometrical factors (i.e. δ) and the high frequency conductance of the diode. Thus, over the frequency range $1/\tau < \omega < 1/\theta$, the equivalent noise current for the cylindrical and spherical geometries as a function of the radii ratio is given by Figure 1.2.3 to within the normalized scale factor. For the frequency range $1/\theta < \omega < 1/\tau_c$, the conductance and thus the noise of the cylindrical configuration is determined by geometrical terms as discussed in Appendix B, whereas in the spherical case, the conductance must be resolved by numerical methods.

At frequencies below $1/\tau$, the noise can be explained in terms of generation-recombination effects.^(1.22) Therefore, the conclusion is drawn that the observed low frequency equivalent noise current is due primarily to g-r noise. It is also noted from Figures 1.5.2 a-f

that the frequency at which the g-r noise and thermal noise levels are equal increases with decreasing temperature. A more qualitative investigation of the low frequency noise in double injection is presently being pursued to establish the form of $I_{eq,g-r}$.

With the high frequency noise in double injection reduced to thermal causes, an interesting question now arises as to when α ceases to be unity. Since times of the order of the mean free time τ_c between collisions is needed to "thermalize" the carrier motion, one would expect therefore noise which is quite different from Nyquist noise at frequencies $\omega_c \sim 1/\tau_c$. Unfortunately, ω_c is usually in the microwave range and complicates the experimental situation. The violation of quasithermal equilibrium provides another possibility for $\alpha \neq 1$. Therefore, double injection structures operating under large current densities may offer unique opportunities to study fluctuations of tepid and hot charge carriers in a solid. As discussed in Section 1.5.2 and illustrated in the experimental data of Figures 1.5.2 a-f, the high frequency noise associated with the p^+-n , $n-n^+$ contacts is indeed negligible for the long silicon double injection diode of Figure 1.2.5. A. van der Ziel has demonstrated both theoretically and experimentally that the noise developed in a p-n junction is shot like noise due to the diffusing of carriers. Therefore, by progressively shortening the physical length L of a double injection diode, a transition in the spectral noise density from thermal noise to semiconductor shot noise is expected. Presumably the transition range can be expressed in terms of the overall physical length L of the device and the ambipolar diffusion length L_a . An investigation of

this nature may yield valuable information in estimating the influence of diffusion on thermal noise.

CHAPTER IITEMPERATURE DEPENDENCE OF THE COMMON HIGH-LEVEL LIFETIME
AND CONDUCTIVITY MOBILITY OF CARRIERS IN SILICON FROM DOUBLE INJECTION2.1. Introduction.

The purpose of this chapter is, in part, to explain the temperature dependence of the I-V characteristic from 140°K to 350°K for a double injection silicon diode operating in the semiconductor regime. In Lampert's model for two-carrier injection into a semiconductor, the magnitude of the current is given by $I = \delta \mu_n \mu_p \tau (p_0 - n_0) V^2$. Therefore, the explanation presented in Section 2.2 of the measured I-V characteristics involves investigating the temperature variation of the charge carrier lifetime and mobility. Section 2.3 thus gives the measured temperature dependence of the common high-level lifetime as determined by differential step response techniques. In Section 2.4, the temperature dependence of the conductivity mobility μ_p of the majority carrier is determined.* In addition, the absolute values of μ_p and μ_n are measured at room temperature with the Hall-Effect (for μ_p) and with the large signal transient method of R. H. Dean (for μ_n).^(2.1) These measurements in conjunction with the I-V characteristic provide a means with which to determine the temperature dependence of the minority carrier mobility μ_n from 140°K to 350°K. The excellent agreement with other independent values found in the

* No distinction is made between conductivity and drift mobility since they are considered equivalent throughout this discussion.

literature for the variation of the electron mobility with temperature provides further support for the model of double injection and validates the approximations of the Lampert representation.^(2.2) This shows that trap-free double injection current can be used to study the common high-level carrier lifetime and conductivity mobility in high-resistivity materials.

2.2. Temperature Dependence of the Current-Voltage Characteristic for Double Injection.

In Figure 1.2.5, the measured I-V characteristic for the silicon double injection diode C-1273, 3, 2.6. B is given at six ambient temperatures from 140°K to 350°K. The long high-resistivity π region is boron doped with an impurity concentration of approximately $1.1 \times 10^{12} \text{ cm}^{-3}$. Therefore, with the acceptor level (0.045eV) fully ionized over the considered temperature range, the number of thermal equilibrium majority carriers (p_0) is constant and equal to the number of acceptor impurities N_a . From the discussion of Section 1.2.3, the I-V characteristic of the diode is properly represented by

$$I = A[9/8]q \mu_p \mu_n \tau N_a \frac{V^2}{L^3} . \quad (2.2.1)$$

Over the range from 140°K to 350°K, the temperature variation of τ , μ_p and μ_n can (approximately) be described by the power-law dependences

$$\tau = \tau^{(0)} \left[\frac{T}{T_0} \right]^\gamma , \quad (2.2.2)$$

$$\mu_p = \mu_p^{(o)} \left[\frac{T_o}{T} \right]^{\alpha_p}, \quad (2.2.3)$$

$$\mu_n = \mu_n^{(o)} \left[\frac{T_o}{T} \right]^{\alpha_n}, \quad (2.2.4)$$

where the room temperature (T_o) values are designated by the zero superscript and the terms γ , α_p and α_n are constants. (2.2,2.3) Such dependences seem characteristic of drift mobilities dominated by lattice scattering. (2.4) Rewriting Eq.(2.2.1) in terms of the applied current and substituting the expressions (2.2.2) to (2.2.4) gives

$$V^2 = \left[\frac{T}{T_o} \right]^{-\gamma + \alpha_p + \alpha_n} \left\{ \frac{I L^3}{A [9/8] \mu_p^{(o)} \mu_n^{(o)} \tau^{(o)} N_a} \right\}. \quad (2.2.5)$$

Figure 2.2.1 gives the values of the square of the voltage from 140°K to 350°K for currents between 2ma and 0.6ma. The measurements are performed under constant current conditions to eliminate the deviation from the $I \propto V^2$ law at 140°K for current levels greater than 2ma. The average of these four slopes is 2.0; therefore,

$$-\gamma + \alpha_p + \alpha_n = 2.0 \quad . \quad (2.2.6)$$

2.3. Common High-Level Lifetime Versus Temperature in Si.

The measured common high-level lifetimes tabulated in Section 1.4 (Table 1.4.3) for temperatures from 140°K to 350°K are obtained by the differential step response method described in Section 1.3. These measurements indicate that when the operating points of the diode are

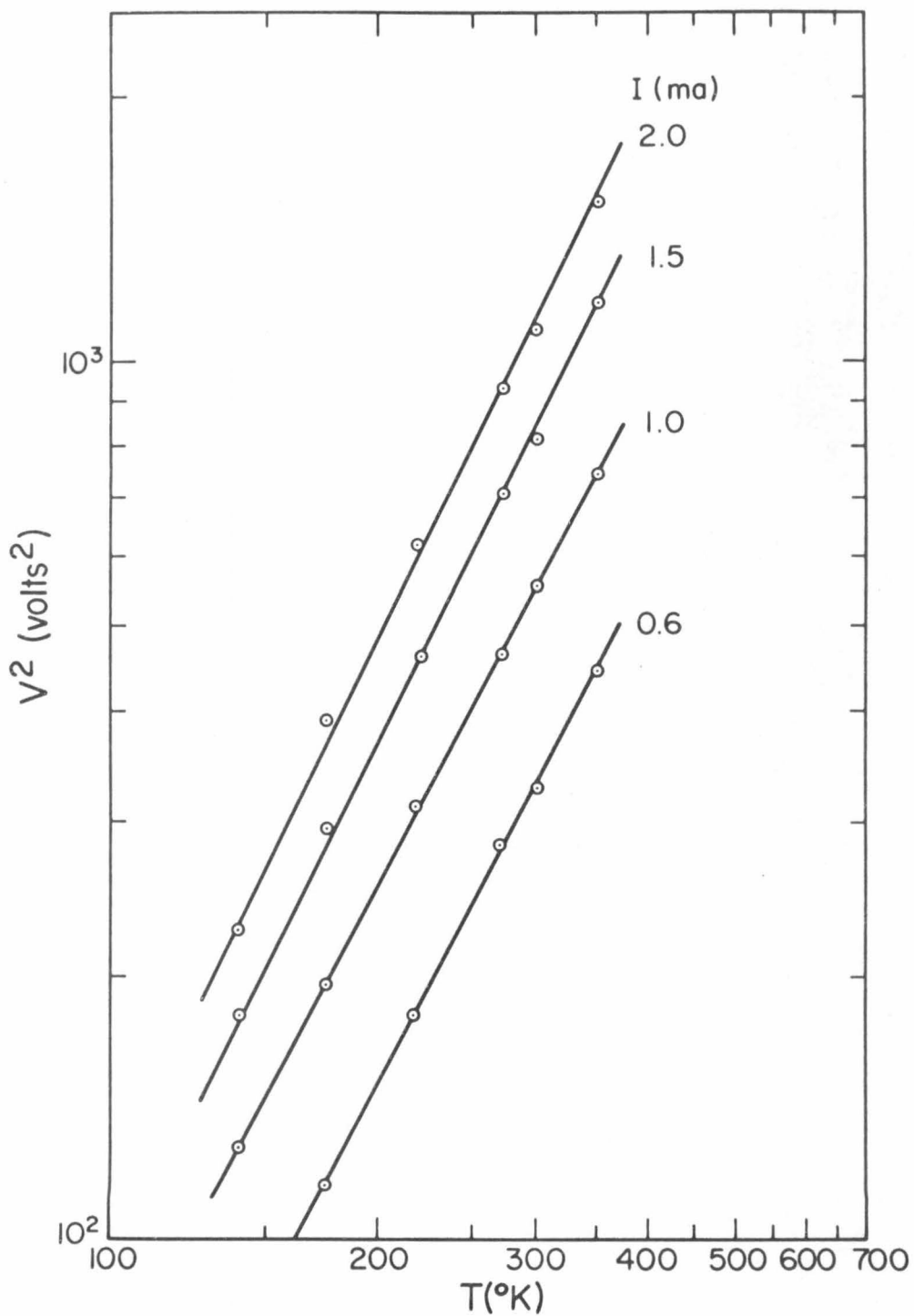


Figure 2.2.1. Square of the dc voltage from 140 $^{\circ}$ K to 350 $^{\circ}$ K for the double injection constant current levels 2.0, 1.5, 1.0 and 0.6ma.

in the square law range, the common high-level lifetime for all temperatures considered does not vary appreciably with injection level. This proves that it is indeed valid to introduce a common high-level lifetime which is independent of the magnitude and spatial distribution of the charge carriers as is done in the high-level approximations of Section 1.2. In Figure 2.3.1, the measured lifetime values are given as a function of temperature. It is seen that Eq.(2.2.2) properly represents the temperature dependence of the common high-level lifetime. Thus, γ equals 1.93 and the room temperature value $\tau^{(o)}$ is equal to 30.7μ sec, so that

$$\tau = (30.7 \times 10^{-6}) \left[\frac{T}{298} \right]^{1.93} \text{sec} . \quad (2.3.1)$$

The nearly square law behavior of the lifetime versus temperature is in excellent agreement with previous measurements by D. M. Evans. (2.3)

2.4. Majority and Minority Carrier Mobility Versus Temperature in High Resistivity Silicon.

From Section 2.2 and 2.3 the temperature dependence of the product of the mobilities $\mu_p \mu_n$ is given by $\mu_p^{(o)} \mu_n^{(o)} \left[\frac{T}{T_o} \right]^{\alpha_p + \alpha_n}$ where $\alpha_p + \alpha_n = 3.93$. The procedure now is to determine individually the room temperature magnitudes $(\mu_p^{(o)}, \mu_n^{(o)})$ and the temperature dependences (α_p, α_n) of the carrier conductivity mobilities.

In the ohmic range (low level injection, Eq.(1.2.18)),

$$I = \mu_p^{(o)} \left[\frac{T_o}{T} \right]^{\alpha_p} [A q N_a \frac{V}{L}] . \quad (2.4.1)$$

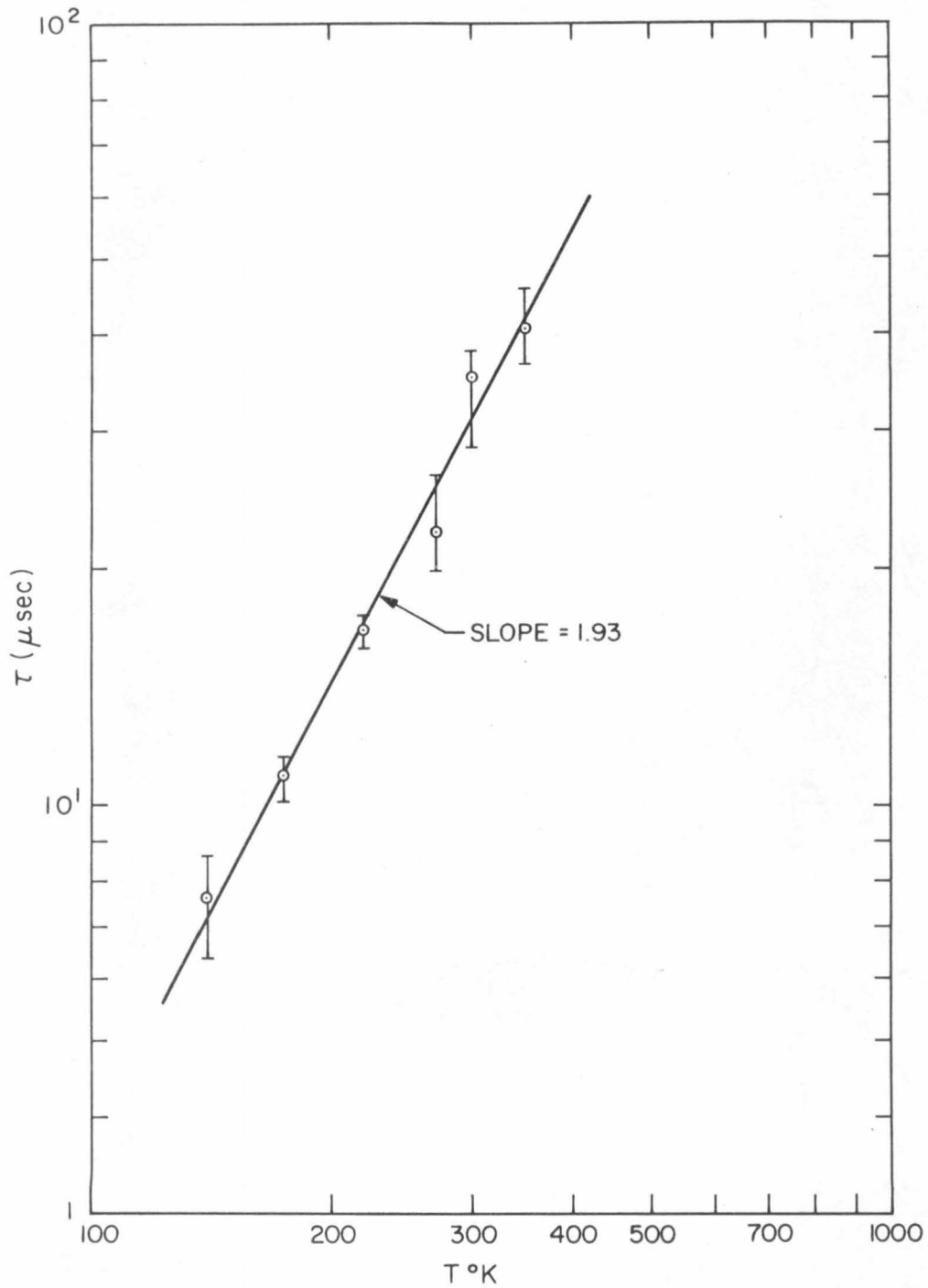


Figure 2.3.1. Measured common high-level lifetime of charge carriers in Si from 140°K to 350°K .

Equation (2.4.1) thus provides a means with which to determine α_p and $\mu_n^{(o)}$. Unfortunately, the ohmic regime, as illustrated in Figure 1.2.5, is not well defined throughout the complete temperature range (140^oK - 350^oK). This is due to the onset of the semiconductor regime and junction effects. Figure 2.4.1 shows potential probe measurements (open dots) with the double injection diode biased at 0.3V. These measurements are made by placing the diode in a fixture containing a tungsten probe which is mounted in a micromanipulator and traversing along a lapped (3200 mesh alumina) side of the structure. The potential does not decrease uniformly across the entire diode but is greatly influenced by the π -n⁺ junction. Similar probe measurements with the diode biased into the semiconductor regime are also shown in Figure 2.4.1 (solid dots). These measurements are in accordance with potential distributions obtained by J. W. Mayer et al.^(2.5) The difficulty encountered with the π -n⁺ junction in the ohmic range precludes the use of the double injection diode in establishing the majority carrier mobility.* This problem is circumvented by fabricating a p⁺ π p⁺ structure (semiconductor resistor) from the same high-resistivity π type silicon. Here, the p⁺ contacts are made by evaporating aluminum onto chemically etched end surfaces (3.17 x 3.14mm) and heating to the alloy temperature. Potential probe measurements

* The resistivity and thus the majority carrier mobility ($\mu^{(o)}$) can be determined from the potential probe measurements of the p⁺ double injection diode given in Figure 2.4.1 (0.3V). However, similar probe measurements proved to be intractable at low temperatures (T < 298^oK).

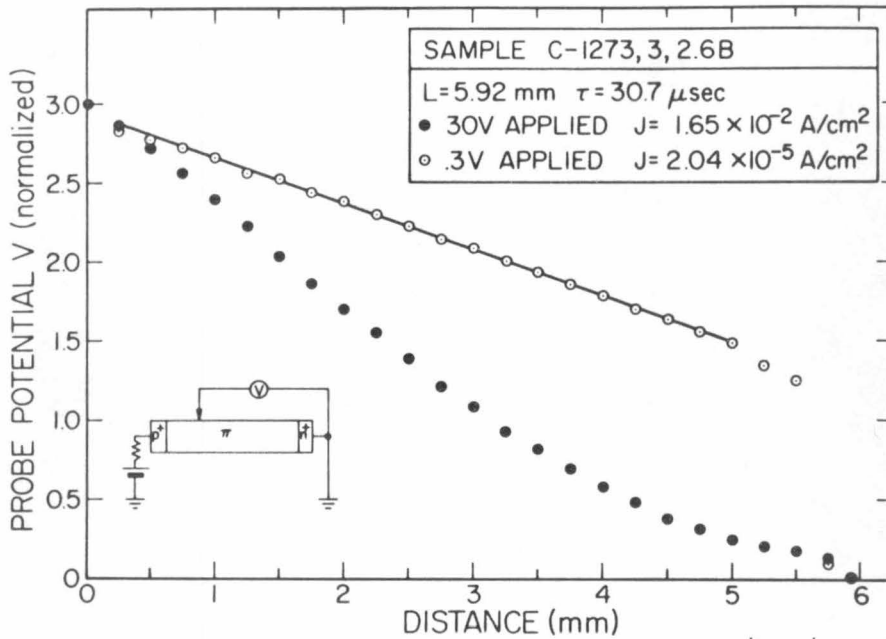


Figure 2.4.1. Potential distribution along a $p^+ \pi n^+$ diode forward biased into the ohmic regime, open data points, and into the semiconductor regime, solid points. Insert illustrates diode orientation.

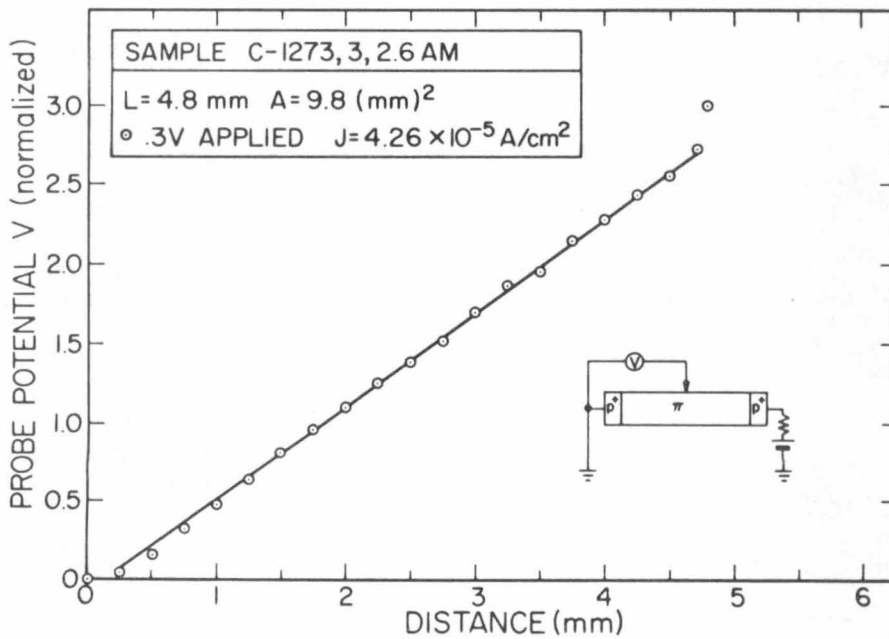


Figure 2.4.2. Potential distribution along a $p^+ \pi n^+$ structure. Insert illustrates the orientation of the experimental arrangement.

shown in Figure 2.4.2 illustrate the nearly ohmic behavior of the $p^+ \pi p^+$ structure. The resistivity of the π type silicon as determined by the ohmic device is $14.2 \text{ k}\Omega\text{-cm}$. By varying the temperature of the $p^+ \pi p^+$ structure under constant voltage bias, the current according to Eq.(2.4.1) will exhibit the temperature dependence of the majority carrier conductivity mobility (μ_p). Figure 2.4.3 shows the measured current of this semiconductor resistor over a temperature range from 140°K to 350°K . The slope of this curve is equal to 2.18 (i.e. $\alpha_p = 2.18$). Since $\alpha_p + \alpha_n = 3.93$, the temperature dependence of the electron mobility (μ_n) is equal to 1.75 (i.e. $\alpha_n = 1.75$). These values are in good agreement with measurements reported in the literature which give $2.3 \leq \alpha_p \leq 2.7$ and $1.5 \leq \alpha_n \leq 2.6$.(2.2)

The absolute values of the conductivity mobilities $\mu_p^{(o)}$ and $\mu_n^{(o)}$ are now considered. R. H. Dean has shown that when a step voltage from zero bias to a point in the semiconductor regime is applied to a double injection diode, the derivative of the resulting current response contains a "cusp". The time t_a at which this cusp occurs is related to the minority carrier mobility $\mu_n^{(o)}$ by

$$\mu_n^{(o)} = \frac{5 L^2}{6 t_a V} \left[\frac{p_o + b n_o}{p_o - n_o} \right] \quad (2.4.2)$$

which reduces to

$$\mu_n^{(o)} = \frac{5 L^2}{6 t_a V} \quad (2.4.3)$$

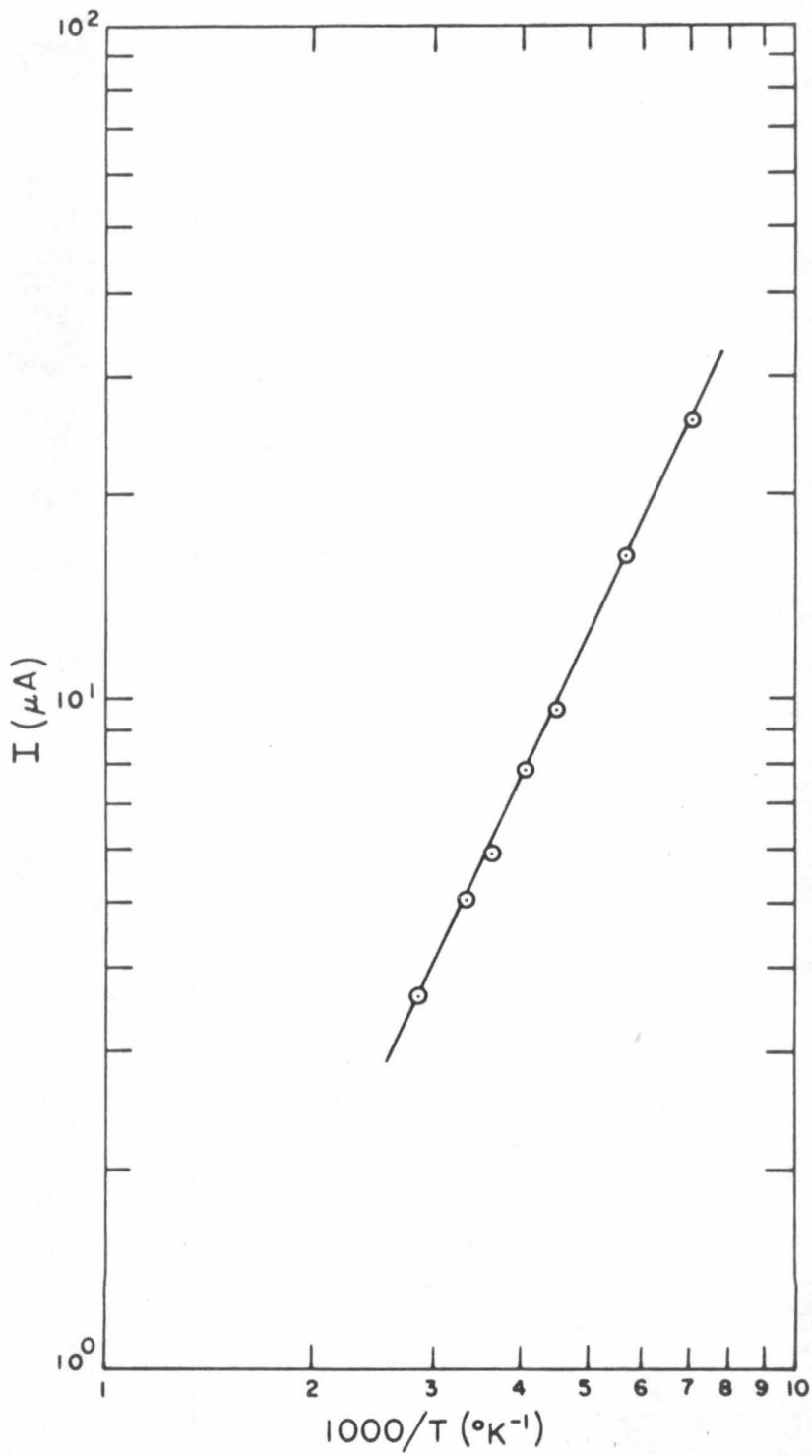


Figure 2.4.3. Measured current of the $p^+ \pi p^+$ structure (C-1273, 3.2.6 AM) from 140 K to 350 K.

for $p_o \gg n_o$.

A large signal step voltage is therefore applied across the double injection silicon diode and the derivative of the current response is measured. The result of such a measurement is shown in Figure 2.4.4. The cusp occurs at 3.25μ sec. From Eq.(2.4.3), the minority carrier mobility is calculated to be $\mu_n^{(o)} = 1280 \frac{\text{cm}^2}{\text{v-s}}$ which is within 6% of the average value obtained by Ludwig and Watters ($\mu_n^{(o)} = 1350 \frac{\text{cm}^2}{\text{v-s}}$). (2.6)

The majority carrier mobility $\mu_p^{(o)}$ is now calculated from the measured resistivity and the doping concentration quoted by the manufacturer ($1.1 \times 10^{12} \text{ cm}^{-3}$) to be $\mu_p^{(o)} = 405 \frac{\text{cm}^2}{\text{v-s}}$. (2.7) As an alternative check, a Hall mobility measurement is performed on the structure using a 3900 gauss magnetic field. With the device operating at a dc current of $3\mu\text{A}$, the measured Hall mobility is $\mu_{p\text{Hall}}^{(o)} = 348 \frac{\text{cm}^2}{\text{v-s}}$. Using the value for the ratio of the Hall hole mobility to the drift mobility of 0.84 as determined by J. Messier and M. Flores in $8\text{k}\Omega\text{-cm}$ silicon, the calculated hole mobility is $\mu_p^{(o)} = 415 \frac{\text{cm}^2}{\text{v-s}}$. (2.8) This value is in good agreement with the hole mobility obtained from the resistivity and doping level. Therefore, the average hole mobility of $410 \frac{\text{cm}^2}{\text{v-s}}$ is taken as the absolute room temperature ($T = 298^\circ\text{K}$) value.

In summary, the high-level lifetime and majority and minority conductivity mobilities in high-resistivity silicon as measured from double injection are

$$\tau = (30.7 \times 10^{-6}) \left[\frac{T}{298} \right]^{1.93} \text{ sec,} \quad (2.4.4)$$

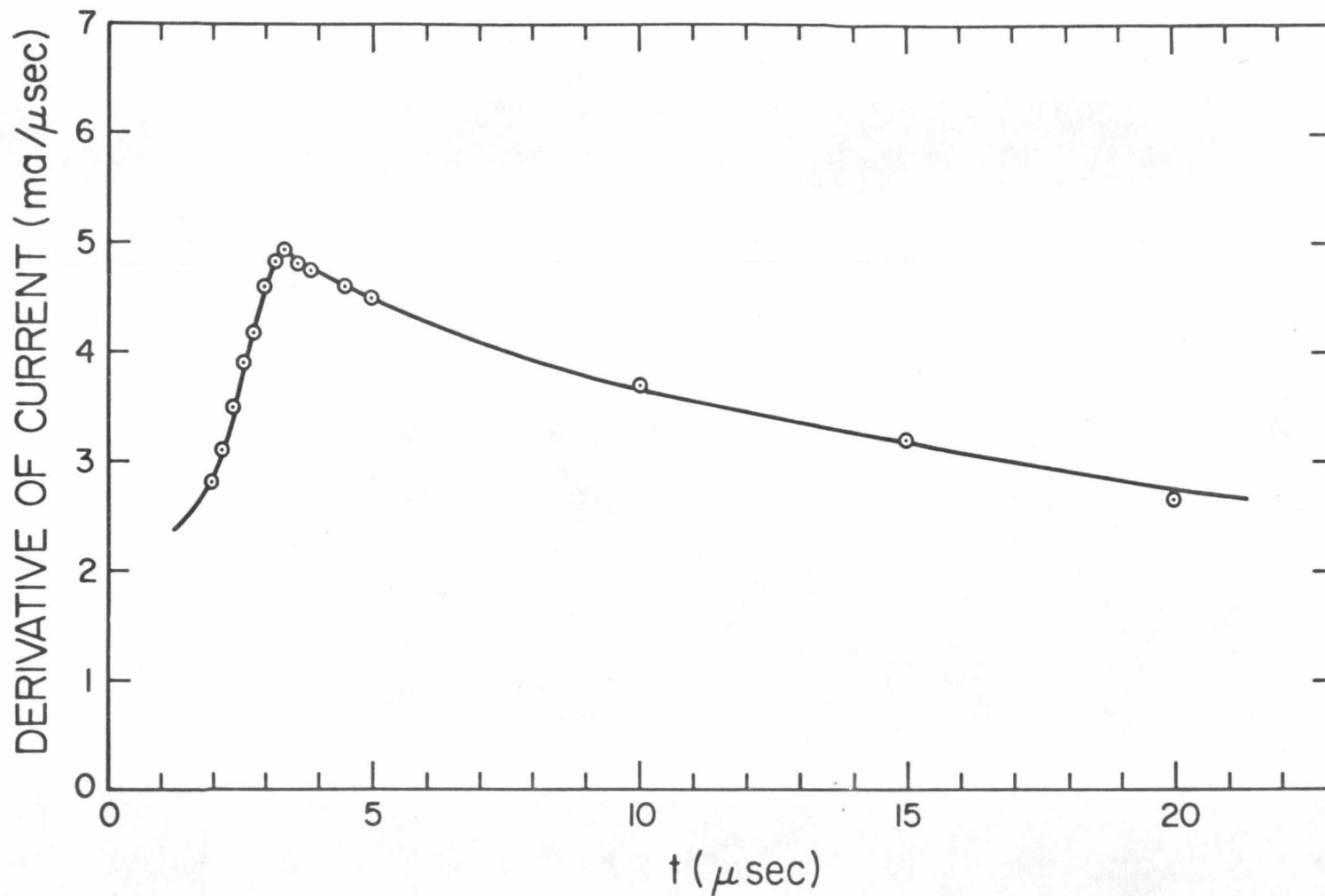


Figure 2.4.4. Derivative of the current response for an applied step voltage (70v) to the double injection silicon diode of Figure 1.2.5. A passive RC network is used to perform the differentiation.

$$\mu_p = 410 \left[\frac{298}{T} \right]^{2.18} \frac{\text{cm}^2}{\text{v-s}}, \quad (2.4.5)$$

$$\mu_n = 1280 \left[\frac{298}{T} \right]^{1.75} \frac{\text{cm}^2}{\text{v-s}} \quad (2.4.6)$$

where $140^\circ\text{K} \leq T \leq 350^\circ\text{K}$. An estimate of the error in all determined values $(\tau, \mu_p, \mu_n, \gamma, \alpha_p, \alpha_n)$ is $\leq 6\%$. Figure 2.4.5. illustrates the electron and hole conductivity mobility given by Eqs.(2.4.5) and (2.4.6). The excellent agreement between these measured quantities and the values quoted in the literature indicate that the temperature dependence of the I-V characteristic from 140°K to 350°K of double injection semiconductor regime diodes is determined entirely by the temperature variation of the common high-level lifetime and the majority and minority carrier conductivity mobilities.

2.5. Conclusion.

It is established that from 140°K to 350°K the dependence of the I-V characteristic of a silicon double injection diode on the lattice temperature is consistent with Eq.(2.2.1) and the variation of $\mu_p(T)$, $\mu_n(T)$ and $\tau(T)$ quoted in the literature. Thus, the validity of Lampert's representation for two-carrier injection in high resistivity p-type silicon is demonstrated throughout the temperature range from 140°K to 350°K . The excellent agreement found between theory and experiment suggests that double injection, once its presence has been established, offers access to the values of $\mu_p(T)$, $\mu_n(T)$ and $\tau(T)$ by relatively simple dc and pulse measurements. To assure the presence of trap-free double injection current may, however, not be an easy

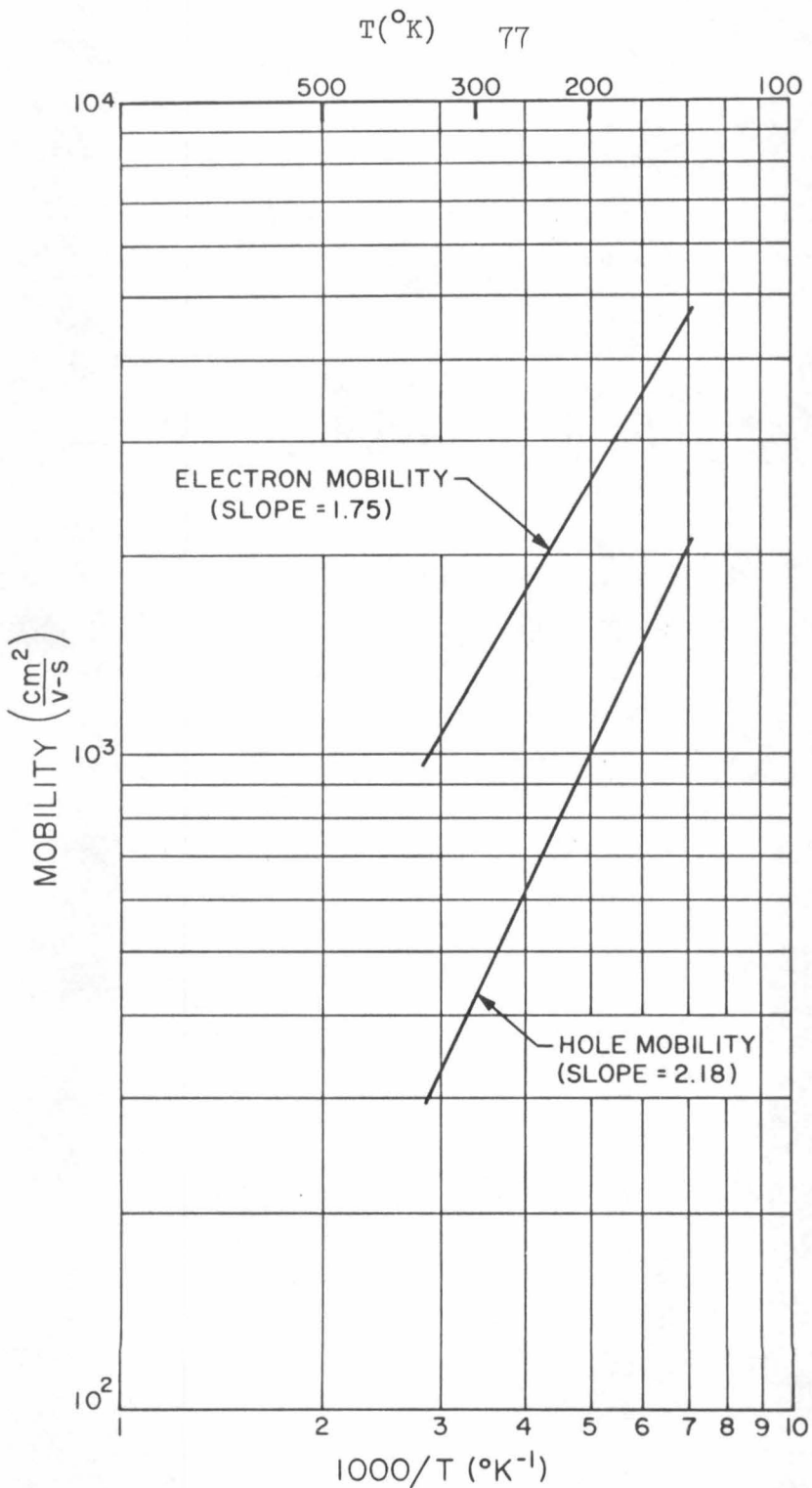


Figure 2.4.5. Electron and hole conductivity mobility from 140°K to 350 K in high-resistivity silicon (> 3KΩ-cm) as determined from double injection.

task, in general. Nevertheless, from the results presented herein, the properties of two carrier injection may possibly be used in the future as a primary tool for investigating the transport behavior of carriers in high-resistivity materials.

APPENDIX ASOLUTION FOR GEOMETRICAL FACTOR

Equation (1.2.20) is written as

$$\frac{1}{h_1 h_2 h_3} \frac{d}{du_1} \left[\frac{E(u_1)}{h_1} \frac{d}{du_1} (h_2 h_3 E(u_1)) \right] = 0 \quad (\text{A.1})$$

which is easily integrated once resulting in

$$\frac{E(u_1)}{h_1} \frac{d}{du_1} (h_2 h_3 E(u_1)) = C_1 \quad (\text{A.2})$$

where C_1 is the integration constant. With the substitution of $w(u_1) = E^2(u_1)$, Eq.(A.2) is reduced to

$$\frac{dw}{du_1} + \frac{2w}{h_2 h_3} \frac{d(h_2 h_3)}{du_1} = \frac{2h_1 C_1}{h_2 h_3} \quad (\text{A.3})$$

Solving (A.3) for $w(u_1)$, and subsequently the electric field, results in

$$E(u_1) = C_1^{1/2} F \quad (\text{A.4})$$

where

$$F = \frac{1}{h_2 h_3} \left[\int_{R_2}^{u_1} 2h_1 h_2 h_3 du_1 \right]^{1/2} \quad (\text{A.5})$$

Since $\vec{J} = -q\mu_p n \tau (p_o - n_o) (\nabla \cdot \vec{E}) \vec{E}$, the constant C_1 is evaluated as

$$C_1 = \left[\frac{-J}{q\mu_p \mu_n \tau (p_0 - n_0) (\nabla \cdot \vec{F} e_1) F} \right] \cdot \quad (\text{A.6})$$

Substituting this value of C_1 into Eq.(A.4) gives

$$\vec{E}(u_1) = \left[\frac{-IF}{Aq\mu_p \mu_n \tau (p_0 - n_0) \nabla \cdot \vec{F} e_1} \right]^{1/2} \vec{e}_1 \quad (\text{A.7})$$

where $I/A = J$. The current-voltage characteristic is determined from Eq.(1.2.21) and the boundary condition (ii). That is,

$$V = \int_{R_1}^{R_2} \left[\frac{-IF}{Aq\mu_p \mu_n \tau (p_0 - n_0) \nabla \cdot \vec{F} e_1} \right]^{1/2} du_1 \quad (\text{A.8})$$

and finally

$$I = \delta q\mu_p \mu_n \tau (p_0 - n_0) V^2 \quad (\text{A.9})$$

where

$$\delta = \left[\int_{R_1}^{R_2} \left[\frac{-F}{A \nabla \cdot \vec{F} e_1} \right]^{1/2} du_1 \right]^{-2} \cdot \quad (\text{A.10})$$

APPENDIX B

SOLUTION OF AC SMALL SIGNAL IMPEDANCE

The linearized ac equations which result from the substitution of Eqs.(1.4.3 a,b,c) into Eqs.(1.4.1) and (1.4.2) are given by

$$J_1 = [(b+1)q\mu_p P_o + j\omega\epsilon] E_1 + (b+1) q\mu_p E_o P_1 \quad (B.1)$$

and

$$\frac{P_T}{h_1 h_2 h_3} \frac{\partial}{\partial u_1} (h_2 h_3 E_1) = - \frac{(b+1)}{\mu_n \tau} [1+j\omega\tau] P_1 \quad (B.2)$$

where $P_T = p_o - n_o$. Solving Eq.(B.1) for $P_1(u_1)$ and substituting into (B.2) yields

$$\frac{d}{du_1} (h_2 h_3 E_1) - \frac{(1+j\omega\tau)(I_o/E_o + j\omega\epsilon A) h_1 h_2 h_3 E_1}{q p_T \mu_p \mu_n \tau A E_o} = \frac{- h_1 h_2 h_3 [1+j\omega\tau] I_1}{q p_T \mu_p \mu_n \tau A E_o} \quad (B.3)$$

where $J_1 = I_1/A$ and $J_o = AqP_o\mu_p E_o(b+1)$. Since $I_o = \delta q\mu_p \mu_n \tau P_T V_o^2$ (see Eq.(A.9)), Eq.(B.3) can be rewritten as

$$\frac{d}{du_1} (h_2 h_3 E_1) - \frac{\delta V_o R_o}{A E_o} (1+j\omega\tau)(I_o/E_o + j\omega\epsilon A) h_1 h_2 h_3 E_1 = - \frac{\delta V_o R_o}{A E_o} h_1 h_2 h_3 [1+j\omega\tau] I_1 \quad (B.4)$$

where $R_o = V_o/I_o$. This equation is now placed in the form

$$\frac{dF_1}{du_1} - R_o \varphi F_1 = - R_o \psi I_1 \quad (B.5)$$

where $F_1 = h_2 h_3 E_1$, $\varphi = \frac{\delta V_o}{A E_o} (1+j\omega\tau)(I_o/E_o + j\omega\epsilon A) h_1$, and

$\psi = \frac{\delta V_o}{AE_o} (1+j\omega\tau) h_1 h_2 h_3$. The solution of Eq.(B.5) and therefore the electric field is easily found to be

$$E_1 = \frac{-R_o I_1 \exp(R_o \int \varphi du_1)}{h_2 h_3} \left[\int_{R_1}^{u_1} \psi \exp(-R_o \int \varphi du_1) du_1 \right] \quad (B.6)$$

By integrating the electric field along u_1 from R_1 to R_2 , the voltage V_1 and subsequently the ac impedance $Z_1 = \frac{V_1}{I_1}$ is determined. The result is

$$Z_1 = R_o \int_{R_2}^{R_1} \left\{ \frac{\exp(R_o \int \varphi du_1)}{h_2 h_3} \left[\int_{R_2}^{u_1} \psi \exp(-R_o \int \varphi du_1) du_1 \right] \right\} du_1 \quad (B.7)$$

which is Eq.(1.4.5).

Consider the cylindrical geometry (case (a)) discussed in Section 1.2.2. From Eq.(B.7), the ac impedance Z_1 after some manipulation is brought into the form

$$Z_1 = \left[\frac{\delta}{2\pi H} \right]^{1/2} \left\{ (1+j\omega\tau) R_o \int_0^{(\rho_2^2 - \rho_1^2)^{1/2}} \frac{u' du'}{\rho_2^2 - u'^2} \int_0^{u'} \left[\frac{u}{u'} \right]^{(1+j\omega\tau)} \exp[j\omega\hat{\Theta}(1+j\omega\tau)(u-u')] du \right\} \quad (B.8)$$

where H is the height of the diode and $\hat{\Theta} = \epsilon R_o (2\pi H \delta)^{1/2}$. Expanding the integral (Eq.(B.8)) in powers of $\omega\hat{\Theta}$ to $O(\omega\hat{\Theta})^2$ and integrating, the resultant expression for the ac impedance is given by

$$Z_1 = \frac{R_o (1+j\omega\tau)}{(2+j\omega\tau)} \left[1 - \frac{j\omega\hat{\Theta}^2}{4} \frac{(1+j\omega\tau)}{(3+j\omega\tau)} \right] \quad (B.9)$$

where

$$\bar{\Theta} = \frac{[4/3] \pi H e R_o [2 \ln_e z + z^{-2} - 1]}{\left[\ln_e (z + (z^2 - 1)^{1/2}) - (1 - z^{-2})^{1/2} \right]^2} \quad (\text{B.10})$$

Case (a)

and $z = \rho_2/\rho_1$. In this case, the impedance (B.9) is formally identical to the expression for the planar geometry impedance (Eq.(1.4.7)). The difference arises in the magnitude of the second order terms which involve the factor " $\bar{\Theta}$ ". In the planar configuration the ratio $\bar{\Theta}/(R_o C_o)$ is constant and equal to $3/2$ (i.e. $\bar{\Theta}/(R_o C_o) = 3/2$). However, for the cylindrical configuration the ratio $\bar{\Theta}/(R_o C_o)$ where C_o is the geometrical capacitance of the cylindrical diode, is not constant but depends upon the value of the radii ratio ρ_2/ρ_1 as shown in Figure B.1. As ρ_2/ρ_1 approaches unity the ratio $\bar{\Theta}/(R_o C_o)$ tends toward the value $3/2$ which is anticipated from the planar result. The form of the ac impedance for case (b) is identical with Eq.(B.9) except $\bar{\Theta}$ is now given by

$$\bar{\Theta} = \frac{[4/3] \pi H e R_o [z^2 - 1 - 2 \ln_e z]}{\left[(z^2 - 1)^{1/2} - \cos^{-1}(1/z) \right]^2} \quad (\text{B.11})$$

Case (b)

From Figure B.1, the ratio $\bar{\Theta}/(R_o C_o)$ in each case (a and b) is a rather insensitive function of the radii ratio and can thus be approximated by the constant value $3/2$ when $\rho_2/\rho_1 < 10$.

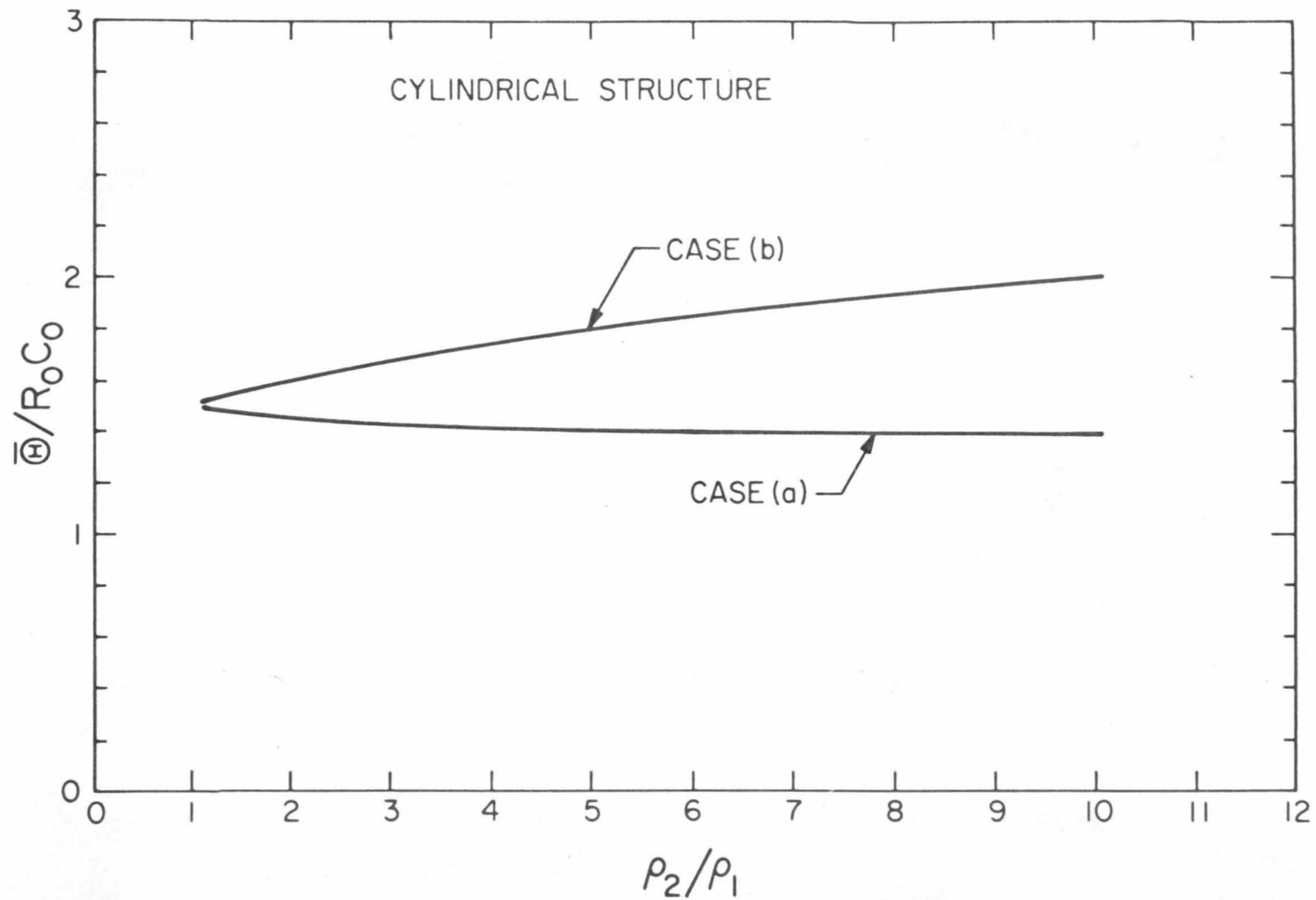


Figure B.1. Ratio $\frac{\bar{\theta}}{R_o C_o}$ versus the radii ratio $\frac{\rho_2}{\rho_1}$ for the cylindrical configuration.

When the second order terms involving $\hat{\Theta}$ are negligible, the first order small signal equivalent circuit shown in Figure 1.4.1b represents both the planar and cylindrical geometries. This is in agreement with the step response analysis of Section 1.3 which is independent of any arguments based on geometrical properties of the double injection diode. The ac impedance for the spherical geometry must be determined from Eq.(B.7) by numerical techniques. Nevertheless, by analogy to the planar and cylindrical cases, it is assumed that the first order equivalent circuit illustrated in Figure 1.4.1b is applicable to the spherical geometry also.

For frequencies $\omega \gg 1/\hat{\Theta}$, Eq.(B.8) is expanded in powers of $1/(\omega\hat{\Theta})$ through $O(\omega\hat{\Theta})^{-2}$. The small signal admittance for the cylindrical configuration is thus given by

$$Y_1 = g + j\omega C_0, \quad \omega \gg 1/\hat{\Theta} \quad (B.12)$$

where

$$g = \frac{[\ln_e(z+(z^2-1)^{1/2}) - (1-z^{-1})^{1/2}][\tanh^{-1}(1-z^{-2})^{1/2}]}{(\ln_e z)^2} G_0 \quad (B.13)$$

Case (a)

$$g = \frac{[(z^2-1)^{1/2} - \cos^{-1}(1/z)][\tan^{-1}(z^2-1)^{1/2}]}{(\ln_e z)^2} G_0 \quad (B.14)$$

Case (b)

and C_0 (the geometrical capacitance) is given by

$$C_o = \frac{2\pi H\epsilon}{\ln_e z} \cdot$$

In the planar geometry, the ratio g/G_o is constant and equal to $4/3$ (i.e. $g/G_o = 4/3$). However, for the cylindrical configuration the ratio g/G_o is not constant but depends upon the value of the radii ratio ρ_2/ρ_1 as shown in Figure B.2. For both cases (a and b), the ratio g/G_o tends toward the value $4/3$ as ρ_2/ρ_1 approaches unity. The conductance g in the frequency range $1/\hat{\Theta} < \omega < 1/\tau_c$ now depends upon geometrical terms and contrasts the result for the first order equivalent circuit given in Figure 1.4.1b.

Numerical means must be used to determine the ac admittance from Eq.(B.7) when the geometrical configuration is spherical.

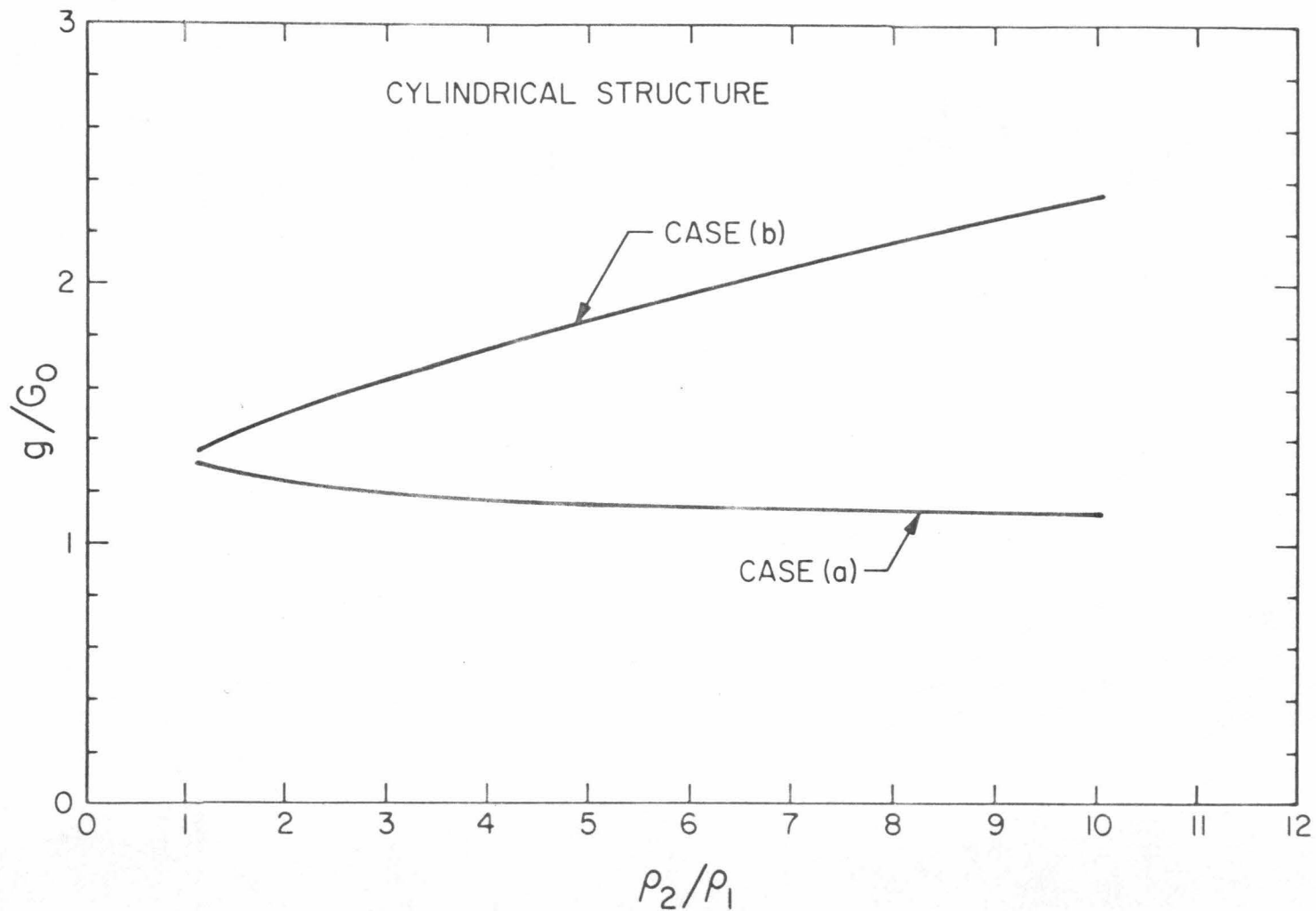


Figure B.2. The conductance ratio g/G_0 versus the radii ratio ρ_2/ρ_1 where g is determined over the frequency range $1/\theta < \omega < 1/\tau_c$.

APPENDIX CTHEORY OF NOISE MEASUREMENT AND EXPERIMENTAL PROCEDURE

C.1. Noise Spectral Density. For a two-terminal network, the noise in a frequency interval Δf can be represented by an equivalent noise voltage $\langle v^2 \rangle^{1/2}$ in series with the network or alternatively by an equivalent noise current generator $\langle i^2 \rangle^{1/2}$ in parallel with the network. (C.1) In general, the network will consist of both passive and active elements. Another representation of the noise current is obtained by introducing $\langle i^2 \rangle$ per unit bandwidth

$$\langle i^2 \rangle / \Delta f = S_i(f) \quad , \quad (C.1.1)$$

where $S_i(f)$ is the "noise spectral density".

In the measurement procedure, the unknown noise source of the device is compared to a known shot noise diode calibrator source. Thus, an alternative representation of the noise current is

$$\langle i^2 \rangle = 2 q I_{eq} \Delta f \quad (C.1.2)$$

where I_{eq} is an "equivalent" saturated noise diode current giving the same mean square value of the short-circuit noise current in the frequency interval Δf . From equations (C.1.1) and (C.1.2), the noise spectral density is given by

$$S_i(f) = 2 q I_{eq} \quad . \quad (C.1.3)$$

I_{eq} will be used throughout the remainder of this discussion as a measure of the noise current spectral density.

C.2. Measurement System. A block diagram of the measurement system is outlined in Figure C.2.1. In this case, noise signals from the device are passed through an amplifier and wave analyzer. The wave analyzer consists of a variable narrow bandpass filter and a linear half-wave rectifier. The rectified output voltage is integrated and displayed on a digital voltmeter. By activating a shot noise calibrator source, the equivalent noise current of the device is subsequently compared to that of a known noise source.^(C.2) This technique eliminates the need for accurate amplifier gain and filter bandpass measurements. The temperature of the device is varied by the temperature control unit. This allows measurements to be made as a function of ambient temperature.

C.3. Small Signal AC Equivalent Circuit and Notation. The small signal ac equivalent circuit along with the pertinent noise sources of the amplifier input are shown in Figure C.3.1. The device noise is represented by a noise generator $\langle i^2 \rangle^{1/2}$, where $\langle i^2 \rangle$ is given by Eq.(C.1.2).

The following notation and symbols are defined as:

$q = |q|$, magnitude of the electronic charge, 1.6×10^{-19}
coulombs.

$T =$ Temperature, $^{\circ}\text{K}$

$k =$ Boltzmann's constant, 1.38×10^{-23} joule/ $^{\circ}\text{K}$

$\Delta f =$ Frequency interval of narrow bandpass filter

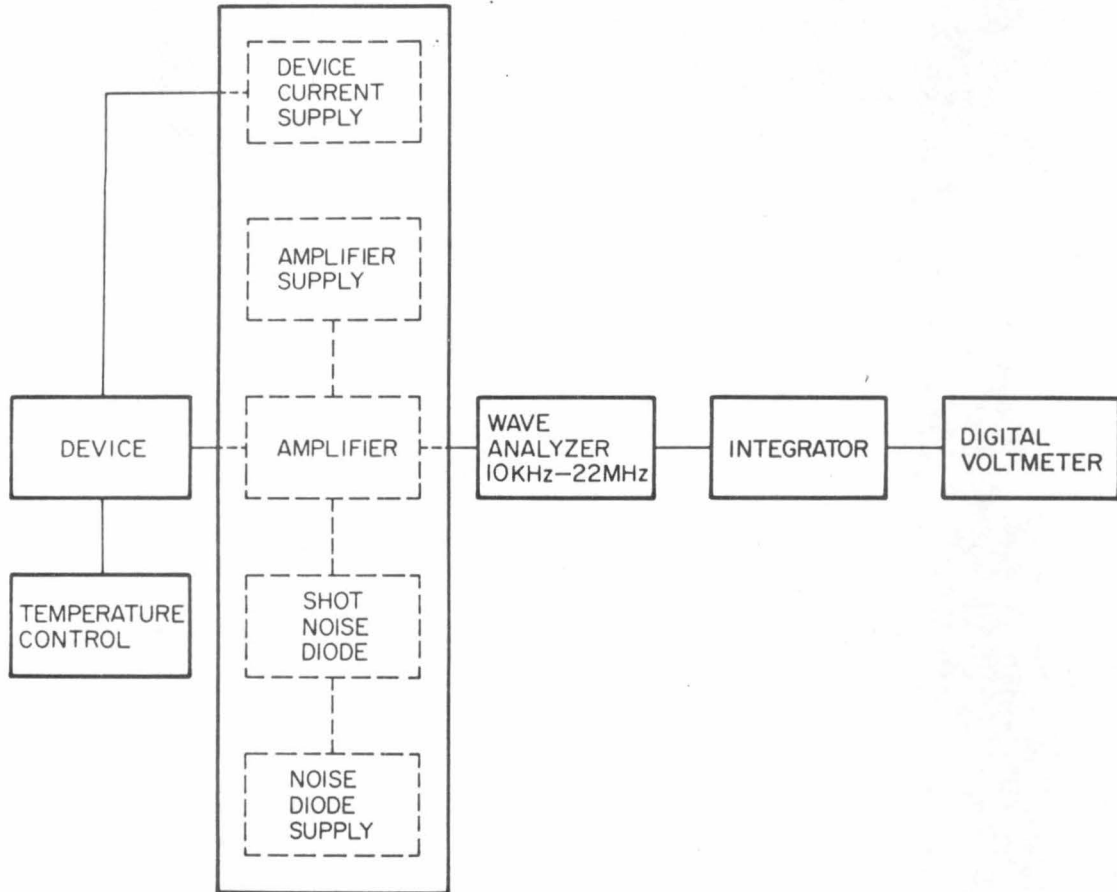


Figure C.2.1. Block diagram of experimental noise measurement apparatus.

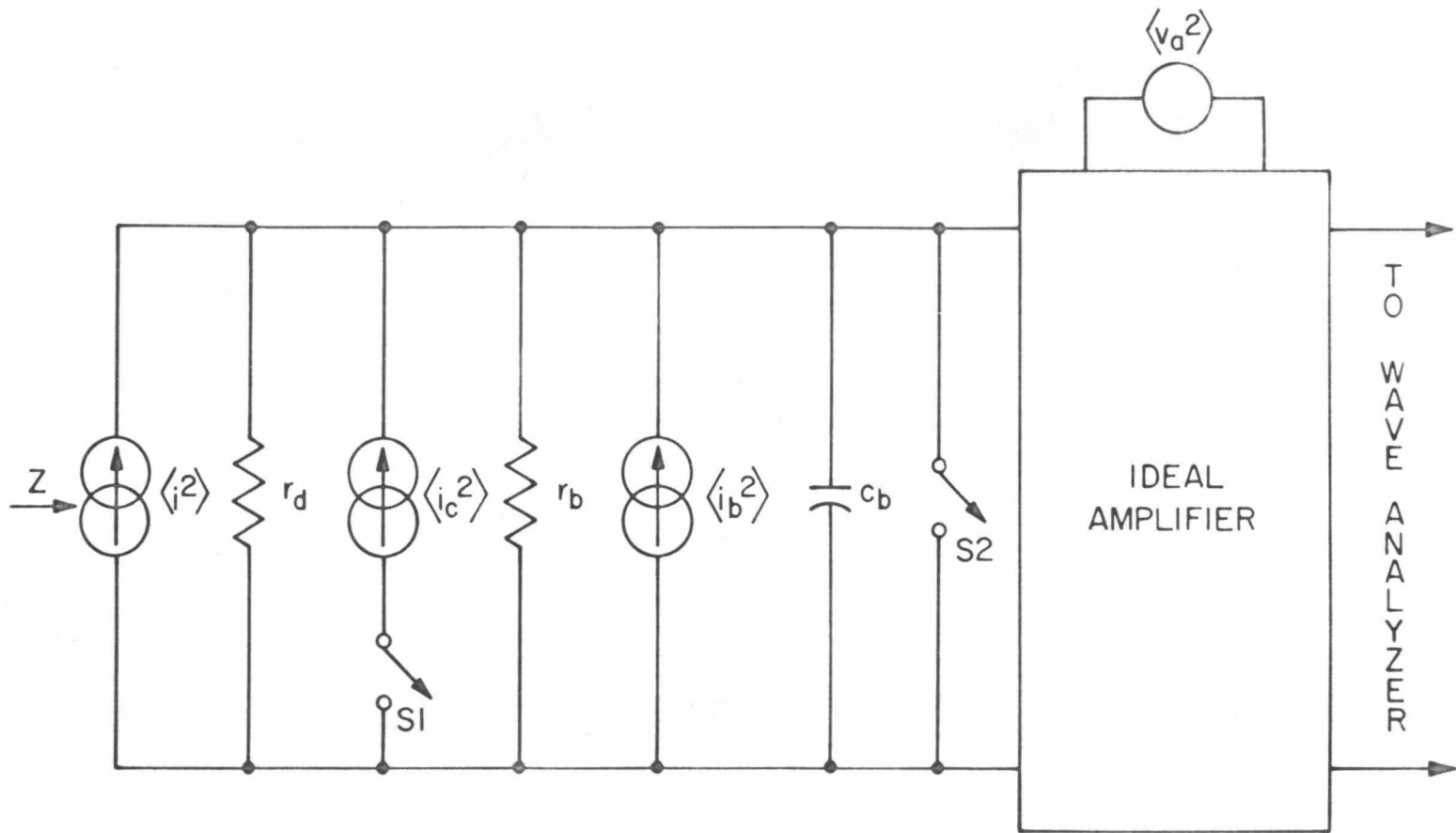


Figure C.3.1. Small signal ac equivalent noise circuit of amplifier input and shot noise source.

$\langle i_c^2 \rangle$ = Shot noise current generator of the temperature limited diode (5722 vacuum tube), $\langle i_c^2 \rangle = 2 q I_c \Delta f$ where I_c is the dc plate current of the diode (C.3)

r_d = Real part of the dynamic impedance of the device

r_b = Real part of amplifier input impedance

c_b = Total input capacitance of amplifier (includes device capacitance)

$\langle i_b^2 \rangle$ = Thermal noise current generator due to r_b ; $\langle i_b^2 \rangle = 4kT(1/r_b) \Delta f$ (C.4)

$\langle v_a^2 \rangle$ = Equivalent noise voltage source of amplifying system. The location of $\langle v_a^2 \rangle$ in Figure C.3.1 expresses the fact that this noise source is found experimentally to be insensitive to the amplifier input impedance Z and the plate current I_c (see Section D.5)

S1 = Switch which activates shot noise source. This is illustrated symbolically in Figure C.3.1 by a switch in series with the noise source $\langle i_c^2 \rangle$

S2 = Shorting switch at amplifier input

Z = Total input impedance (includes r_d)

G_a = Voltage gain of system with $\langle v_a^2 \rangle$ as the source. This gain is experimentally found to be insensitive to the input impedance Z and plate current I_c (see Section D.5)

G_1 = Voltage gain of system with $\langle i_c^2 \rangle$ and $\langle i_b^2 \rangle$ as sources, S1 open, S2 open

G_2 = Voltage gain of system with $\langle i^2 \rangle$, $\langle i_c^2 \rangle$ and $\langle i_b^2 \rangle$ as sources, S_1 closed, S_2 open

η = Gain ratio, $\eta = |G_1|^2 / |G_2|^2$. The introduction of η is motivated by experimental evidence indicating that in general $G_1 \neq G_2$

C.4. Measurement Procedure. The variable narrow bandpass filter

(wave analyzer) is set at a center frequency f_o and the output noise voltages $\langle v_a^2 \rangle^{1/2}$, $\langle v_1^2 \rangle^{1/2}$ and $\langle v_2^2 \rangle^{1/2}$ are measured by employing the following procedure (see Figure C.3.1):

- (i) With S_1 open, S_2 closed, measure $\langle v_a^2 \rangle^{1/2}$
- (ii) With S_1 open, S_2 open, measure $\langle v_1^2 \rangle^{1/2}$
- (iii) With S_1 closed, S_2 open, measure $\langle v_2^2 \rangle^{1/2}$
and the noise diode plate current I_c (i.e. I_c is adjusted such that $\langle v_2^2 \rangle^{1/2} \gg \langle v_1^2 \rangle^{1/2}$, see Appendix D.1.1)
- (iv) The device is removed from the input. Steps (i), (ii) and (iii) are now repeated yielding $\langle \tilde{v}_a^2 \rangle^{1/2}$, $\langle \tilde{v}_1^2 \rangle^{1/2}$, $\langle \tilde{v}_2^2 \rangle^{1/2}$ and \tilde{I}_c .

By repeating this procedure for various f_o 's, these eight measured quantities in conjunction with the value η are sufficient to obtain a measure of the device noise spectral density I_{eq} .

C.5. Analysis. Since r_d , r_b , c_b , G_a , G_1 and G_2 are smoothly varying functions of frequency, they can be considered to be constant over a sufficiently small frequency interval Δf . The voltage gain G_a

of the amplifier equivalent noise source is assumed to be independent of the input impedance Z .^{*} With these assumptions, the noise voltages $\langle V_a^2 \rangle$, $\langle V_1^2 \rangle$ and $\langle V_2^2 \rangle$ are expressed as

$$\langle V_a^2 \rangle = \langle v_a^2 \rangle |G_a|^2 \quad (C.5.1)$$

$$\langle V_1^2 \rangle = \langle v_a^2 \rangle |G_a|^2 + \langle i^2 \rangle |Z|^2 |G_1|^2 + \langle i_b^2 \rangle |Z|^2 |G_1|^2 \quad (C.5.2)$$

$$\langle V_2^2 \rangle = \langle v_a^2 \rangle |G_a|^2 + \langle i^2 \rangle |Z|^2 |G_2|^2 + \langle i_b^2 \rangle |Z|^2 |G_2|^2 + \langle i_c^2 \rangle |Z|^2 |G_2|^2 \quad (C.5.3)$$

Here, for example, the terms in Eq.(C.5.3) represent the amplifier noise, device noise, amplifier input resistance noise and the shot noise sources respectively. Solving Eqs.(C.5.1), (C.5.2), and (C.5.3) for the equivalent noise current I_{eq} of the device gives

$$I_{eq} = \left[\frac{\langle V_1^2 \rangle - \langle V_a^2 \rangle}{\eta \langle V_2^2 \rangle - \langle V_1^2 \rangle} \right] \left[1 - \frac{(1-\eta) \langle V_a^2 \rangle}{\eta \langle V_2^2 \rangle - \langle V_1^2 \rangle + (1-\eta) \langle V_a^2 \rangle} \right] I_c - \frac{2kT}{qr_b} \quad (C.5.4)$$

The second term of Eq.(C.5.4) is recognized as the equivalent noise current ($I_{eq,b}$) of r_b , where

$$I_{eq,b} = \frac{2kT}{qr_b} \quad (C.5.5)$$

* Any change in the system gain due to "Miller effect" is found experimentally to be negligible (see Appendix D).

This equivalent noise current is experimentally determined by invoking step (iv) of the measurement procedure (C.4). That is, $I_{eq} = 0$ and

$$I_{eq,b} = \left[\frac{\langle \tilde{v}_1^2 \rangle - \langle \tilde{v}_a^2 \rangle}{\tilde{\eta} \langle \tilde{v}_2^2 \rangle - \langle \tilde{v}_1^2 \rangle} \right] \left[1 - \frac{(1-\tilde{\eta}) \langle \tilde{v}_a^2 \rangle}{\tilde{\eta} \langle \tilde{v}_2^2 \rangle - \langle \tilde{v}_1^2 \rangle + (1-\tilde{\eta}) \langle \tilde{v}_a^2 \rangle} \right] \tilde{I}_c \quad (C.5.6)$$

Thus, Eq.(C.5.4) becomes

$$I_{eq} = \left[\frac{\langle v_1^2 \rangle - \langle v_a^2 \rangle}{\eta \langle v_2^2 \rangle - \langle v_1^2 \rangle} \right] \left[1 - \frac{(1-\eta) \langle v_a^2 \rangle}{\eta \langle v_2^2 \rangle - \langle v_1^2 \rangle + (1-\eta) \langle v_a^2 \rangle} \right] I_c - I_{eq,b} \quad (C.5.7)$$

At the center frequency f_o , the equivalent noise current is now totally determined by experimentally measured quantities. When the value of η (see Appendix D) is equal to 1.0, Eq.(C.5.7) simplifies to

$$I_{eq} \Big|_{\eta=1} = \left[\frac{\langle v_1^2 \rangle - \langle v_a^2 \rangle}{\langle v_2^2 \rangle - \langle v_1^2 \rangle} \right] I_c - \left[\frac{\langle \tilde{v}_1^2 \rangle - \langle \tilde{v}_a^2 \rangle}{\langle \tilde{v}_2^2 \rangle - \langle \tilde{v}_1^2 \rangle} \right] \tilde{I}_c . \quad (C.5.8)$$

In this case, I_{eq} does not depend upon the characteristics of the system gain.

APPENDIX DREALIZATION OF NOISE MEASUREMENT APPARATUS

D.1. Description of Amplifier and Input Circuitry. The amplifier, shot noise calibrator diode and associated power supplies are illustrated in Figures D.1.1 and D.1.2. Here, S1, S2, Q1 and the parallel combination of R1, R2 and R3 represent respectively the elements S1, S2, $\langle i_c^2 \rangle$ and r_b (to first order) in the ac equivalent circuit shown in Figure D.3.1. The resistors R1, R2 and R3 constitute the input biasing networks and are considered as part of the input impedance of the amplifier. The vacuum tube Q1 (type 5722), which operates as a temperature limited diode, is used as the shot noise calibrator source. ^(D.1) This noise source is activated by the switch S1 located in the filament supply. A 200vdc supply in conjunction with R1 provides the device current, whereas a similar voltage supply with R2 provides the plate current I_c for the shot noise diode. By adjusting the filament current via R62, the equivalent noise current (I_c) of the shot noise diode can be varied from 0 to 500 μ A (see table D.1.1). Metering circuits M1 and M2 continuously monitor the device current and noise diode plate current respectively. The first stage of amplification, which is denoted by Q2 and Q3, is a standard cascode arrangement and the output stage Q12 is an emitter follower. The somewhat unusual mid-stage gain section is differential. This is done to provide an option for having a differential input. However, this possibility was not exploited since the single ended cascode arrangement proved adequate.

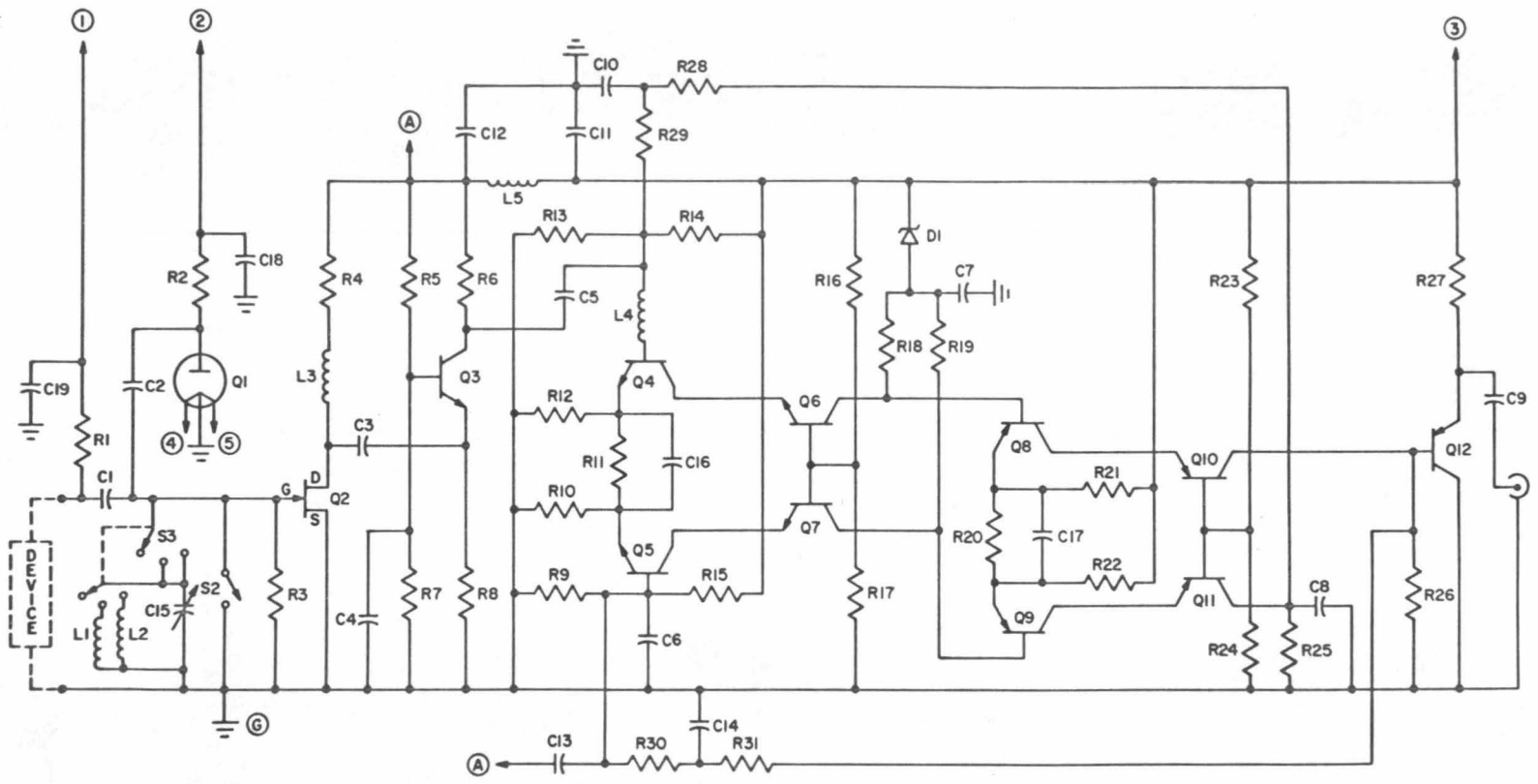


Figure D.1.1. Input amplifier and shot noise source.

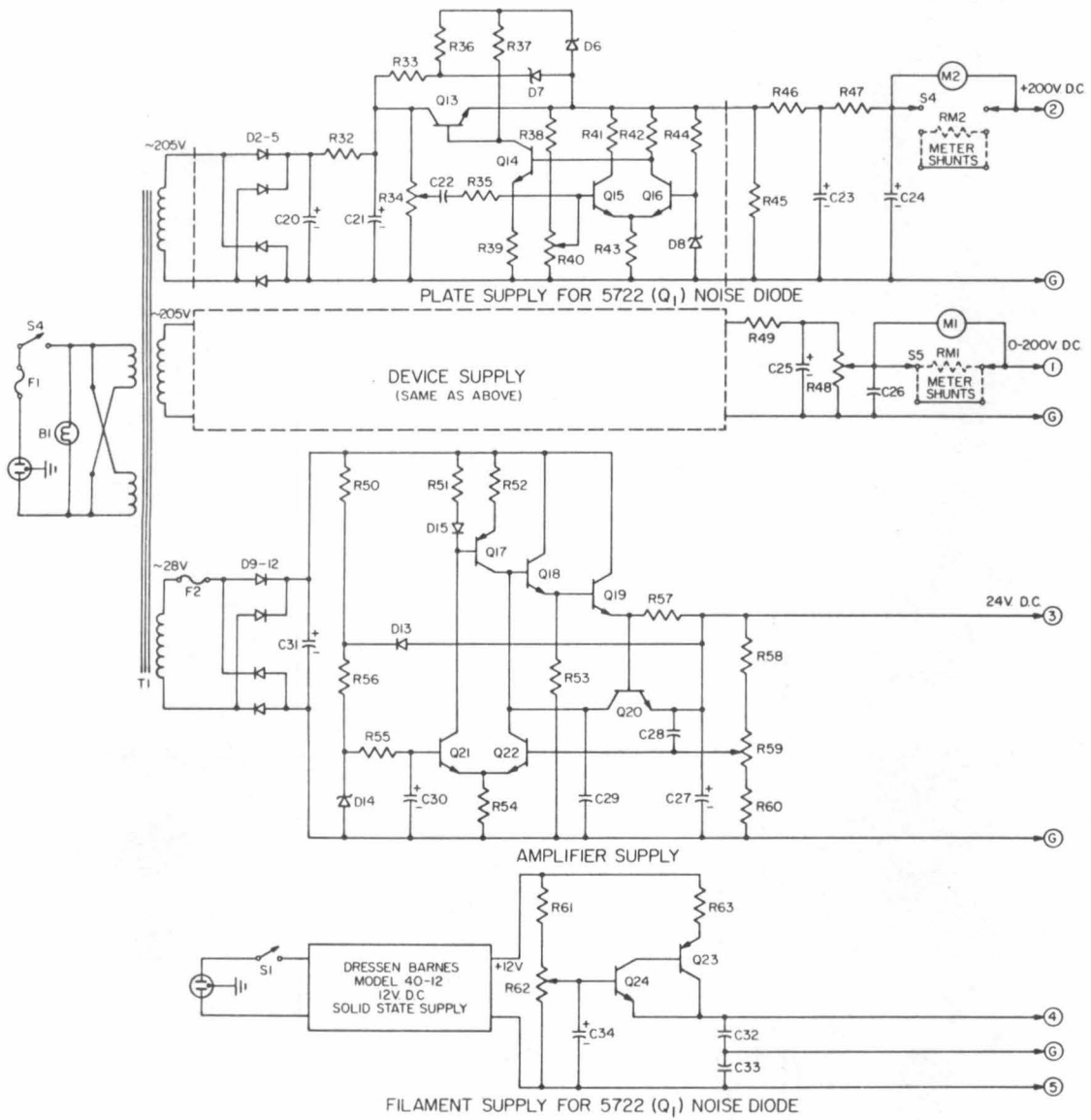


Figure D.1.2. Power supplies for amplifier, shot noise calibrator source and device.

TABLE D.1.1

Parts list for amplifier and power supplies.

RESISTORS*

R1	100k, 1/2w, MF
R2	100k or 300k, 1/2w, MF
R3	10M Ω , 1/2w, MF
R4, 5, 16, 23	1.5k, 1/2w, MF
R6	3.48k, 1/4w, MF
R7, 17, 21, 22, 24	750, 1/4w
R8	10.7k, 1/4w, MF
R9, 13	10k, 1/4w, MF
R10, 12	620, 1/4w
R11	39, 1/4w
R14, 15	40.2k, 1/2w, MF
R18, 19	221, 1/8w, MF
R20	24, 1/4w
R25, 26	267, 1/8w, MF
R27, 54	2k, 1/2w
R28, 29, 30, 31	8.2k, 1/2w, MF
R32	1k, 1/1w
R33	4.7k, 1/1w
R34	1M Ω , 1w
R35	680k, 1/2w
R36	2.2k, 1/2w
R37	4.7k, 1/2w
R38	110k, 1/2w
R39	100k, 1/2w
R40	10k, trim.pot.
R41	47k, 1/2w
R42	68k, 1/2w
R43	2.4k, 1/2w
R44	120k, 1/2w
R45	10k, 10w
R46, 47	5k, 1w
R48	10k, Helipot
R49	10k, 1w
R50	3.3k, 1/2w
R51, 52	470, 1/2w
R53	27k, 1/2w
R55, 60	1k, 1/2w
R56	2.8k, 1/2w
R57	3, 1/2w
R58	1.82k, 1/2w
R59	510 trim.pot.
R61	1.1k, 1w
R62	500 Helipot
R63	2.15, 25w
RM1	{selected meter shunts
RM2	{1/2w, MF

Table D.1.1 (Continued)

CAPACITORS **

C1, 2, 22	0.02
C3, 7	0.47
C4, 8	1.0
C5, 28	0.1
C6, 11, 12, 13	0.47
C9	2.0
C10, 14, 32, 33	0.01
C15	5-80 pfd
C16	2.2 pfd
C17	3.9 pfd
C18, 19	100 pfd
C20, 21, 25	80
C23, 24	40
C26	0.5
C27, 30	100
C29	0.001
C31	4000
C34	50

INDUCTORS

L1	10 μ h, 50 turns #22 wire on Micrometal T80-7 toroid core
L2	2.1 μ h, 20 turns #16 wire on Micrometal T80-6 toroid core
L3	4.7mh
L4	8 μ h
L5	80 μ h

TRANSISTORS

Q2	SF-5868 or 2N3819 (selected for low noise)
Q3, 6, 7	2N2501
Q4, 5	2N3572
Q8, 9, 12	2N4261
Q10, 11	MM 999
Q13	RCA 40424
Q14, 15, 16	RCA 40327
Q17	2N3906
Q18, 20, 21, 22	2N3904
Q19	Tektronix 151-140
Q23	2N442
Q24	2N3715

DIODES & ZENERS

D1	IN 962
D2, 3, 4, 5	IN 4005

Table D.1.1 (Continued)

D9, 10, 11, 12, 13, 15	Tektronix 152-0040
D6	IN 752
D7, 8	IN 227
D14	IN 960B

NOISE DIODE

Q1	5722 (Sylvania)
----	-----------------

METERS

M1, M2	0-50 μ A TAUT BAND
--------	------------------------

* All resistor values are in ohms; MF = metal film.

** All capacitor values are in microfarads unless otherwise specified; capacitors associated with the amplifier are ≥ 50 VWDC, whereas the capacitors associated with the power supply are ≥ 250 VWDC.

D.2. Amplifier and Wave Analyzer Characteristics. In order to perform the necessary noise measurements, the amplifier must be linear, low noise and have sufficient voltage gain over a wide frequency range to enable the wave analyzer to detect the small noise signals. The wave analyzer is a Hewlett-Packard HOR-312A with a frequency range from 10kHz to 22MHz. A filter bandpass of 3kHz is used for all measurements. Since the device dynamic resistance is of the order of 1 k Ω to 10 k Ω the real part of the amplifier input impedance should be greater than 10 k Ω in order to reduce attenuation of the device noise signals. However, the output impedance of the amplifier should be about 50 Ω or less since this is the value of the input impedance of the wave analyzer.

A junction Field-Effect-Transistor (FET), type SF-5868, is utilized in the first stage of amplification since it fulfills the criterion of low noise and high input impedance (the real part being greater than 100Meg Ω). Figure D.2.1 shows the amplifier gain as a function of frequency for an input ac generator source impedance of 50 Ω . For this case the amplifier is also terminated in 50 Ω . The gain is greater than 40db over the frequency range from 10kHz to 22MHz. This gain is more than adequate for the sensitivity of the wave analyzer. Since $R_1 = 300$ k Ω , $R_2 = 100$ k Ω and $R_3 = 10$ Meg Ω , the real part of the input impedance is approximately 75 k Ω . The measured output impedance is 8.4 Ω .

Van der Ziel has shown that for a junction FET the theoretical equivalent noise resistance is given by

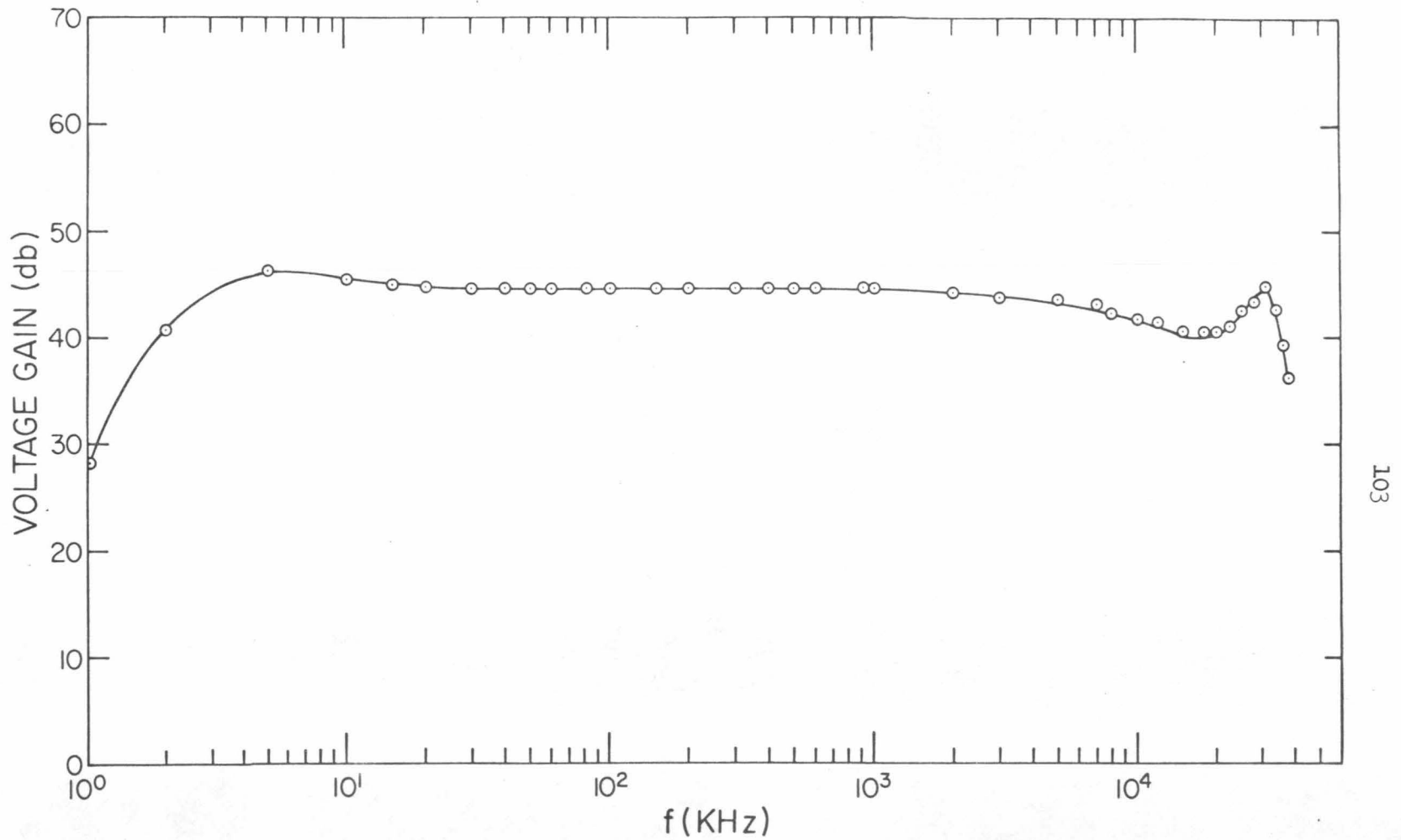


Figure D.2.1. Voltage gain of the input amplifier (Figure D.1.1) from 10kHz to 40MHz.

$$R_{eq} = \frac{2}{3} \left[\frac{1}{g_m} \right], \quad (D.2.1)$$

where g_m is the transconductance of the FET.^(D.2) A measured $g_m \Big|_{VGS=0}$ of 4.5 ma/v for the SF-5868 corresponds therefore to a theoretical equivalent noise resistance of 148 Ω . The actual measured short-circuit equivalent noise resistance of the amplifier is shown in Figure D.2.2. A high frequency limiting value for R_{eq} of approximately 275 Ω indicates that possibly other noise sources besides that of the FET are contributing to the overall short-circuit noise of the amplifier. For device dynamic resistances greater than 275 Ω , the noise of the amplifier is sufficiently low to insure accurate measurements of I_{eq} .

D.3. High Frequency Effects. The total measured input capacitance of the amplifier is 15.4 pfd. Approximately 6pfd, 7pfd and 2.4pfd are associated with the FET, noise diode, and distributed wiring capacitance respectively. Depending on the dynamic resistance of the device, this input capacitance may appreciably attenuate the noise signals at high frequencies. As a result, the signal noise approaches that of the amplifier, and the error in the measured spectral noise density of the device may become very large (see Eq.(C.5.7)). To overcome this effect, a tuned circuit consisting of a high Q inductor and variable capacitor is added to the input impedance of the amplifier. This circuitry consists of the elements L1, L2, C15 and S3 as shown in Figure D.1.1. The combination of the inductor L1, input capacitance ($\sim c_p$) and

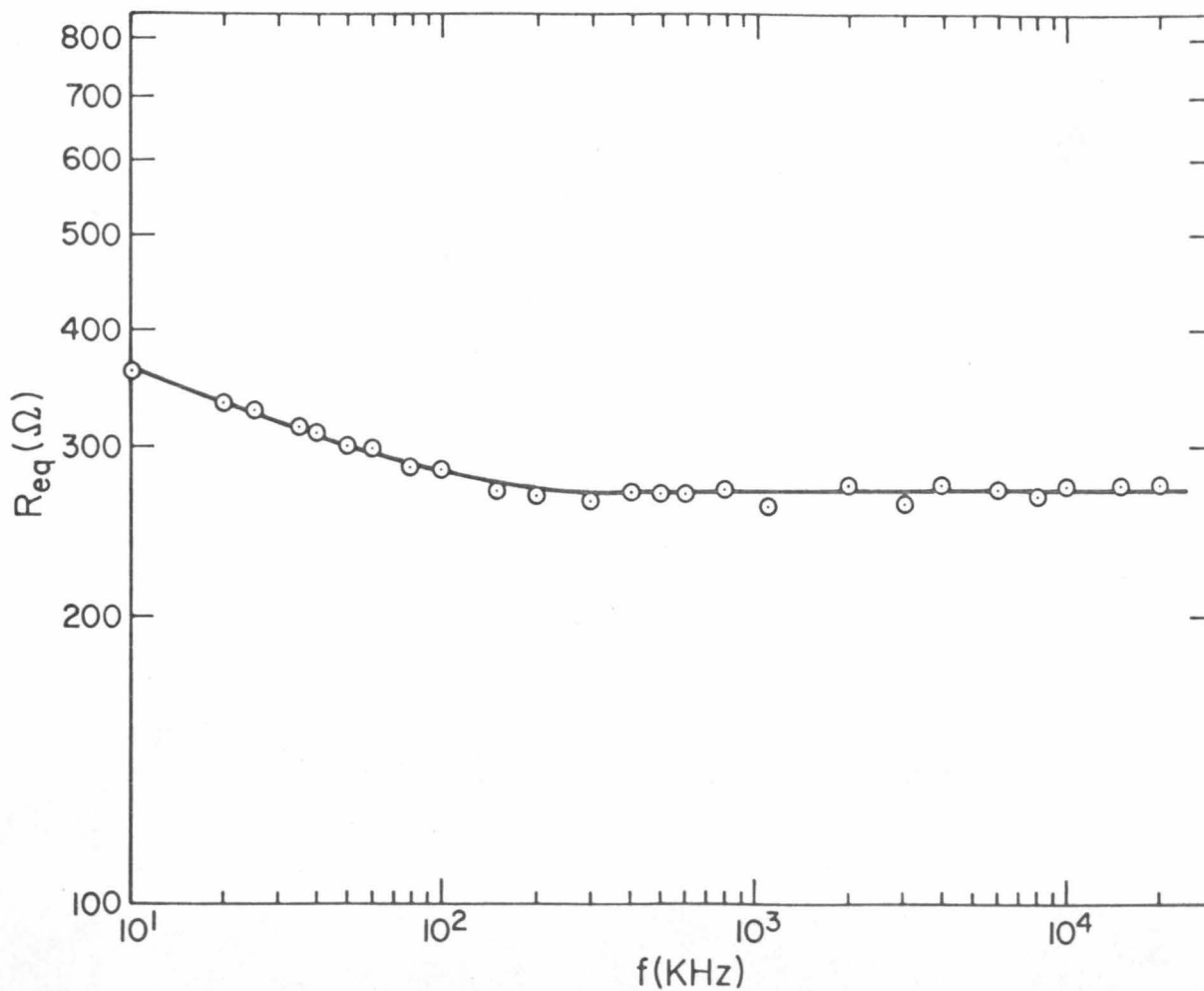


Figure D.2.2. Equivalent noise resistance of amplifier (Figure D.1.1) from 10kHz to 22 MHz.

variable capacitor C15 is tunable over a frequency range from 5MHz to 9MHz, while L2 in a similar arrangement covers 13 MHz to 22 MHz. With the wave analyzer set, for example, in the frequency range where L1 is applicable, the variable capacitor C15 is adjusted for maximum noise output signal. Under this resonance condition, the reactive part of the input impedance is eliminated, and the parallel combination of R1, R2, R3 plus the losses associated with L1 determines the magnitude of the real part of the amplifier input impedance ($> 10k\Omega$). The theory and procedure of the noise measurement described in Appendix C is not altered by the introduction of the tuned circuitry at high frequencies. Since the Q of the wave analyzer is much greater than that of the tuned circuit, the frequency bandpass Δf is still determined by the wave analyzer.

D.4. Low Frequency Effects. If the dynamic resistance of the device is sufficiently small, the increasing impedance of the coupling capacitor C1 at low frequencies causes the measured noise spectral density to decrease. Under these conditions, the correct equivalent noise current is calculated from

$$I_{eq} = \xi(f_o) I_{eq \text{ measured}}, \quad (D.4.1)$$

where

$$\xi(f_o) = \frac{1 + (2\pi f_o r_d C1)^2}{(2\pi f_o r_d C1)^2} . \quad (D.4.2)$$

Since the value of the capacitor C_1 is $0.02\mu\text{fd}$, which in this case is the maximum value attainable within the given space restrictions, Eq.(D.4.1) is utilized when r_d is less than $1\text{k}\Omega$ over the appropriate low frequency range.

D.5. Measurement of Gain Ratio η . The deviation of the gain ratio η from 1.0 is found experimentally to depend only on the magnitude of R_3 and the noise diode plate current I_c . This probably arises from a dc leakage current through C_2 developing a bias voltage across R_3 which subsequently alters the g_m of the FET Q_2 . This effect is negligible (i.e. $\eta = 1$) when the high frequency L-C network is switched into the amplifier input since L_1 and L_2 effectively short circuit any dc voltage appearing across R_3 . The measured values of η for various values of I_c and R_3 are given in Table D.5.1.

TABLE D.5.1

Measured values of the gain ratio η .

η	$I_c \leq 50\mu\text{A}$	$I_c = 100\mu\text{A}$	$I_c = 200\mu\text{A}$	$I_c = 400\mu\text{A}$
L-C out $R_3=10\text{Meg}\Omega$	1	0.953	0.883	0.828
L-C out $R_3=500\text{K}\Omega$	1	1	1	0.950
L-C in	1	1	1	1

It is noted that for I_c less than $50\mu\text{A}$, the gain ratio η is equal to 1 and does not depend on the amplifier input impedance.

D.6. Comments on Construction. The amplifier, input circuitry, noise diode and associated power supplies form an integral system. The utilization of solid state devices permits all of these units to be placed in a single metal enclosure which acts as a Faraday shield. This construction also facilitates the location of one signal ground which is labeled (G) in Figure D.1.1. The general construction techniques of high frequency equipment are employed in laying out the amplifier and input circuitry. Metal film resistors which exhibit nearly ideal thermal noise over a wide range of frequency and current are used extensively. The shorting switch S2 is a point contact of low capacity. Inductors L1 and L2 are toroids and have Q's typically greater than 175. All power supplies are of the series regulator type and have peak to peak ripple of less than 1 millivolt.

D.7. Active Integrator. With a noise signal at the input, the output voltage of the narrow bandpass wave analyzer fluctuates around a mean value \bar{v} ($\bar{v} \leq 1V$). To improve on the expected error of this reading, the output voltage is integrated for T seconds (see Appendix H).

The integrator consists basically of an operational amplifier with an RC feedback network. Figure D.7.1 illustrates such an integrating scheme. Here, the operational amplifier Q1 in conjunction with C2 and R6 through R11 make up the integrator for the fluctuating input voltage. The total integration time T is determined by a similar arrangement (Q2, C3, R12-R17) which integrates a constant input voltage of 1V. When S2 is in the RESET position, the FET switches Q4 and Q5 are on; capacitors C2 and C3 are discharged by resistors R18 and R20 respectively. Placing S2 in the INT.

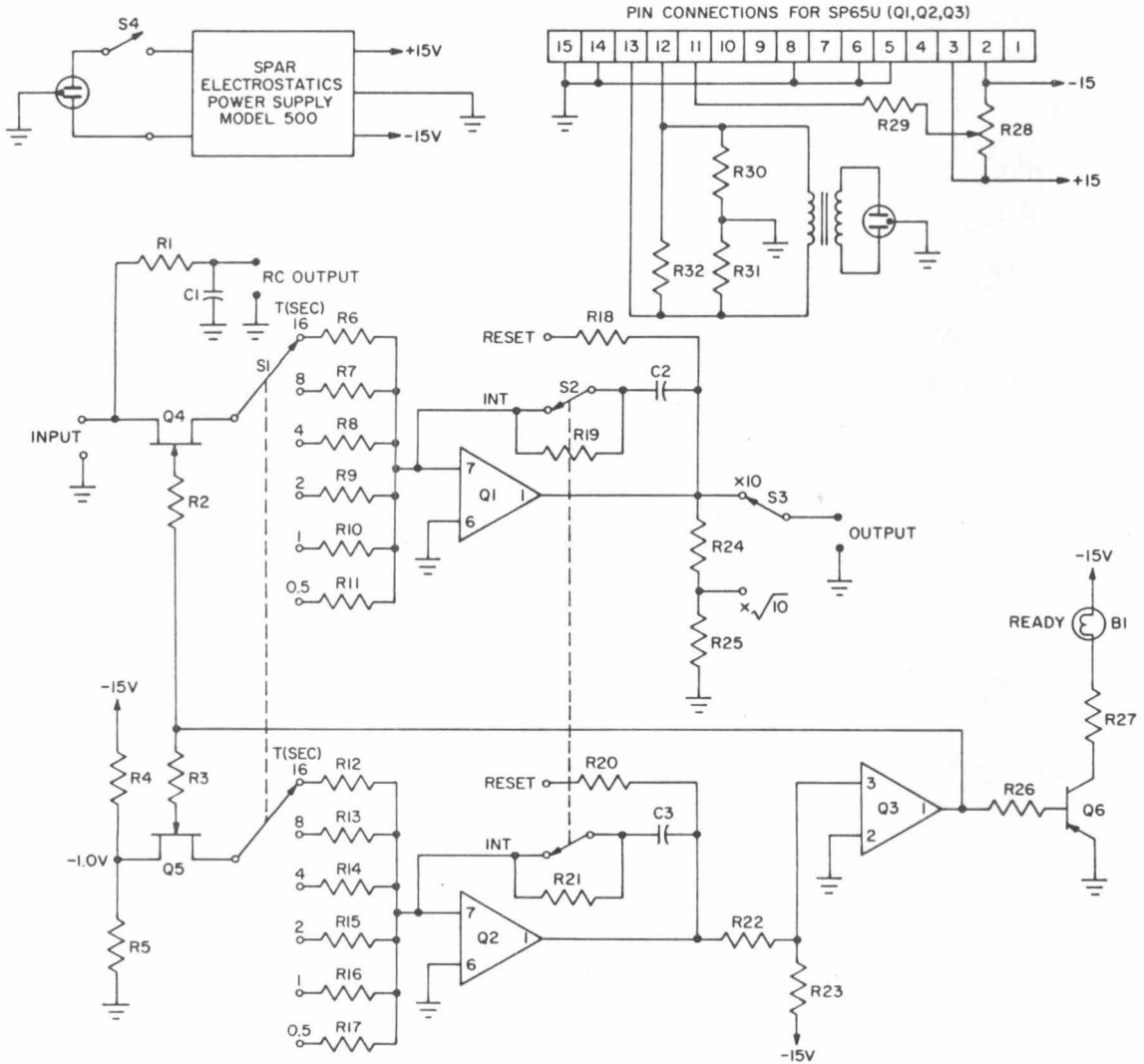


Figure D.7.1. Wiring diagram for active integrator.

TABLE D.7.1

Parts list for active integrator.

RESISTORS *

R1, 29	1M Ω , 1/2w
R2, 3	100M Ω , 1/4w
R4	14k, 1/2w
R5, 18, 20, 30	1k, 1/2w
R6, 12	1.6M Ω , 1/2w
R7, 13	800k, 1/2w
R8, 14	400k, 1/2w
R9, 15	200k, 1/2w
R10, 16, 22	100k, 1/2w
R11, 17, 24	50k, 1/2w
R19, 21	500k, 1/2w
R23	150k, 1/2w
R25	231k, 1/2w
R26	10k, 1/2w
R27	30, 1/2w
R28	100k, 1/2w
R31	470, 1/2w
R32	10k, 10w

CAPACITORS **

C1, C2, C3	4 μ fd
------------	------------

DEVICES

Q1, 2, 3	Philbrick SP65Au operational amplifier
Q4, 5	2N3819

* All resistors values are in ohms; MF = metal film.

** All capacitor values are \geq 50 VWDC.

position starts the integration. After T seconds, the level detector Q3 activates the READY indicator B2 and turns off Q4 and Q5 simultaneously. The integrated input voltage is read at the output of Q1 with a digital voltmeter. One of the main advantages of such an integrator is that the relative standard error is smaller than with a passive RC integrator of the same time constant. (D.3)

APPENDIX E

CALIBRATION MEASUREMENTS

E.1. Wave Analyzer Detector. An investigation of the wave analyzer shows that the detector is a linear half-wave rectifier followed by a passive RC time averaging circuit. For an input sine wave with amplitude V_o , the half wave-rectified output voltage $\langle V_{h.w.r} \rangle_S$ is $\frac{V_o}{\pi}$. The output of the wave analyzer, however, is calibrated in R.M.S. (root-mean-square) voltage and reads

$$\langle V^2 \rangle_{S, \text{INDICATED}}^{1/2} = \frac{V_o}{\sqrt{2}} . \quad (\text{E.1.1})$$

Therefore, for a sine wave

$$\frac{\langle V^2 \rangle_{S, \text{INDICATED}}^{1/2}}{\langle V_{h.w.r.} \rangle_S} = \frac{\pi}{\sqrt{2}} . \quad (\text{E.1.2})$$

Now consider an input noise voltage being applied to the same half-wave rectifier. The noise voltage is assumed to have a normal (Gaussian) distribution which is defined as

$$p(v) = \frac{1}{\sqrt{2\pi}} \frac{1}{v_{\text{eff}}} \exp \left[-\frac{1}{2} \left[\frac{v}{v_{\text{eff}}} \right]^2 \right] \quad (\text{E.1.3})$$

where $p(v) dv$ is the probability that the noise voltage has a value between v and $v + dv$ and v_{eff} is the standard deviation. For a half-wave rectifier, the expected value of the output noise voltage is

$$(\bar{v}_{\text{h.w.r.}})_N = \int_0^{\infty} \frac{v}{\sqrt{2\pi} v_{\text{eff}}} \exp\left[-\frac{1}{2} \left(\frac{v}{v_{\text{eff}}}\right)^2\right] dv = \frac{v_{\text{eff}}}{\sqrt{2\pi}} \quad (\text{E.1.4})$$

and the R.M.S. value is given by

$$\frac{\langle v^2 \rangle_N^{1/2}}{(\bar{v}_{\text{h.w.r.}})_N} = v_{\text{eff}} \quad (\text{E.1.5})$$

Therefore, for a noise voltage

$$\frac{\langle v^2 \rangle_N^{1/2}}{(\bar{v}_{\text{h.w.r.}})_N} = \sqrt{2\pi} \quad (\text{E.1.6})$$

From Eqs.(E.1.2) and (E.1.6), the actual R.M.S. noise is given by

$$\langle v^2 \rangle_N^{1/2} = \frac{2}{\sqrt{\pi}} \langle v^2 \rangle_{N, \text{INDICATED}}^{1/2} \quad .$$

Since the system is used as a comparator (see Eq.(C.5.7)) this correction does not appear explicitly in the evaluation of the result. It does appear, however, in the testing procedure discussed in Section E.2.

E.2. Verification of Nyquist's Theorem. According to Nyquist's theorem, the mean square value of the voltage developed across a resistance R at the ambient temperature T °K in a narrow frequency interval Δf is (C.4)

$$\langle v^2 \rangle = 4k T R \Delta f \quad (\text{E.2.1})$$

A $10k\Omega$ metal film resistor in lieu of the device is placed at the input of the amplifier. The measured value of this resistor in parallel with the input biasing networks of the amplifier is $8.2 k\Omega$ at a temperature of $298^{\circ}K$. With the wave analyzer set at a center frequency of $50kHz$ and a bandwidth Δf of $3kHz$, the voltage gain of the system as measured by the wave analyzer is 173 . From Eq.(E.2.1) the theoretical noise voltage is

$$\langle V^2 \rangle_{\text{theoretical}} = 4(1.38 \times 10^{-23} \text{ j/}^{\circ}K)(298^{\circ}K)(8.2k\Omega)(3kHz) = 0.405(\mu V)^2.$$

The output reading is $97\mu V$ (RMS at wave analyzer). Therefore the actual noise measured with respect to the input is

$$\langle V^2 \rangle_{\text{measured}} = \frac{4}{\pi} \left[\frac{97_{\mu V}}{173} \right]^2 = (0.401 \pm .01)(\mu V)^2 .$$

The experimental result agrees very well with the theoretical expression of Nyquist and demonstrates that metal film resistors exhibit nearly ideal thermal noise.

E.3. Verification of Schottky's Theorem. In accordance with Schottky's theorem, the mean square noise current from a temperature limited vacuum tube diode in a frequency interval Δf is given by

$$\langle i^2 \rangle = 2q I_c \Delta f , \quad (\text{E.3.1})$$

where I_c is the dc plate current of the diode. (C.3)

Under experimental conditions identical with those described in E.2 the output noise voltage with the shot noise diode activated is (see Eq.(C.5.3))

$$\langle V^2 \rangle \propto 2 q I_c R^2 |G_2|^2 \Delta f , \quad (\text{E.3.2})$$

where

$$\langle V^2 \rangle = \frac{4}{\pi} \langle V_2^2 \rangle .$$

Figure E.3.1 shows a plot of the output noise $\langle V^2 \rangle$ as a function of the shot noise diode plate current I_c . The result demonstrates the linear dependence of $\langle V^2 \rangle$ on I_c , and also establishes the linearity of the amplifying system. From the slope of this curve and Eq.(E.3.2), the value of $|q|$ is determined as

$$|q| = (1.65 \pm .06) \times 10^{-19} \text{ coulombs} .$$

This measured value for the magnitude of the electronic charge is in good agreement with the accepted value of 1.602×10^{-19} coulombs. It also verifies the pure shot noise behavior, as expressed by Eq.(E.3.1), of the temperature limited diode QL.

E.4. Resistor Calibration. In order to fully check the performance of the noise measuring apparatus and verify the theory and procedure described in Appendix C, the noise spectral density for a series of resistors is measured at room temperature ($T \approx 298^\circ\text{K}$). The theoretical

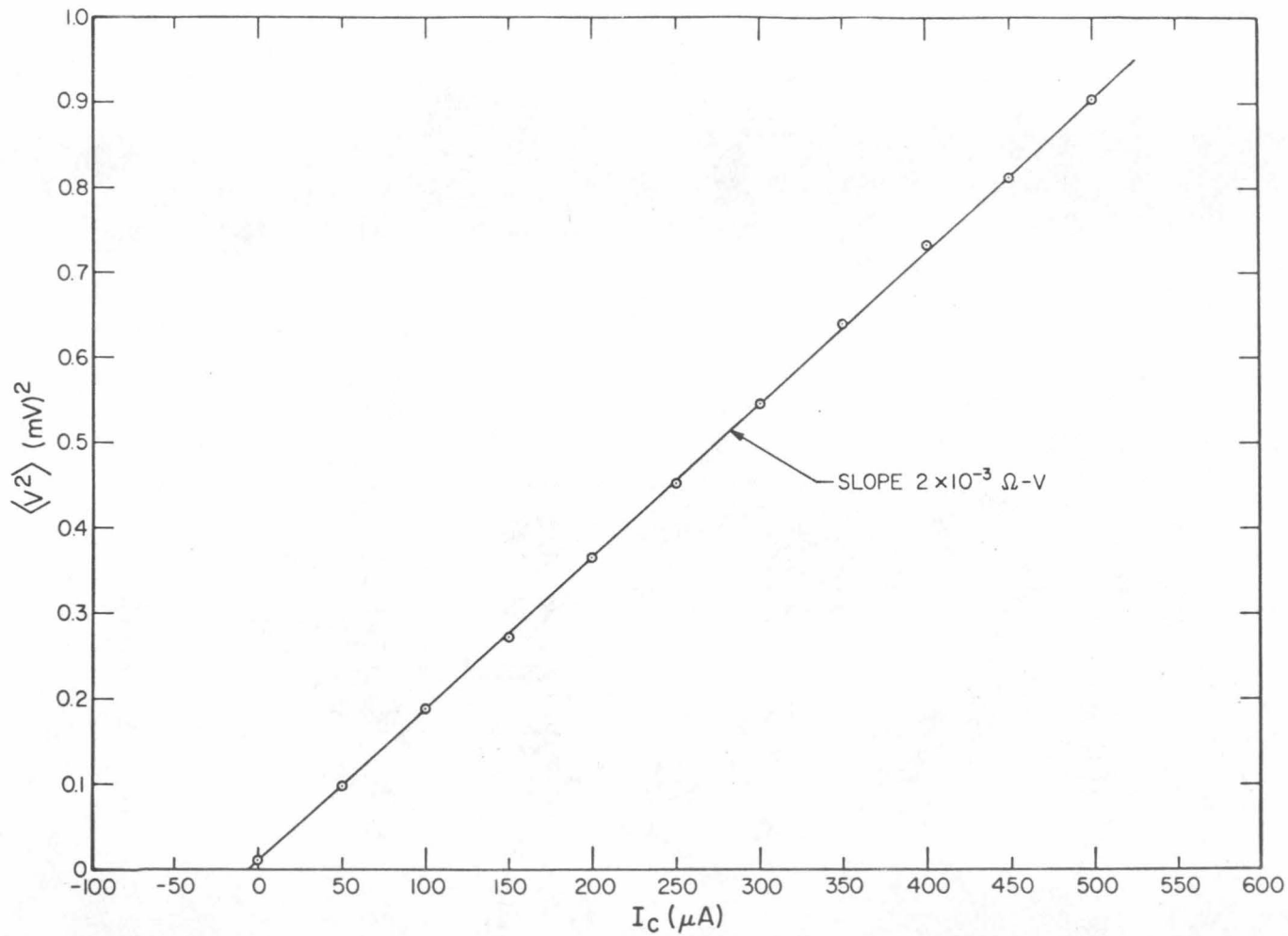


Figure F.3.1. Mean square amplifier output voltage versus noise diode dc plate current for 5722 vacuum tube at 50kHz.

equivalent noise current of a resistance R is given by

$$I_{eq_theoretical} = \frac{2kT}{qR} \quad . \quad (E.4.1)$$

Figure E.4.1 shows the measured equivalent noise current for a 100k Ω , 10k Ω , 1k Ω and 301 Ω metal film resistor over a frequency range from 10kHz to 22MHz. The results are tabulated in Table E.4.1. In all cases, the average measured equivalent noise current deviates by no more than 5% from the theoretical equivalent noise current calculated from Eq.(E.4.1). Since the real part of the amplifier input impedance at 22MHz is approximately 17k Ω , the experimental results for the 100k Ω resistor illustrate the rather remarkable accuracy that can be obtained by this technique. The experimental data presented in Figure E.4.1 demonstrate that the apparatus has a capability of making noise spectral density measurements on two terminal devices which may have an equivalent noise current from 0.5 μ A to over 170 μ A. The long term stability, reliability and absence of temperature drift of the system, is attributed to well designed solid state circuitry and is reflected in the measurements shown in Figure E.4.1.

TABLE E.4.1

Comparison between the theoretical and measured equivalent noise current for resistors.

Resistance (Ω)	$I_{eq_measured}$ (μ A)	$I_{eq_theoretical}$ (μ A)	% Error
100k	0.50	0.52	3.9%
10k	5.2	5.2	0%
1k	51	52	1.9%
301	164	171	4.1%

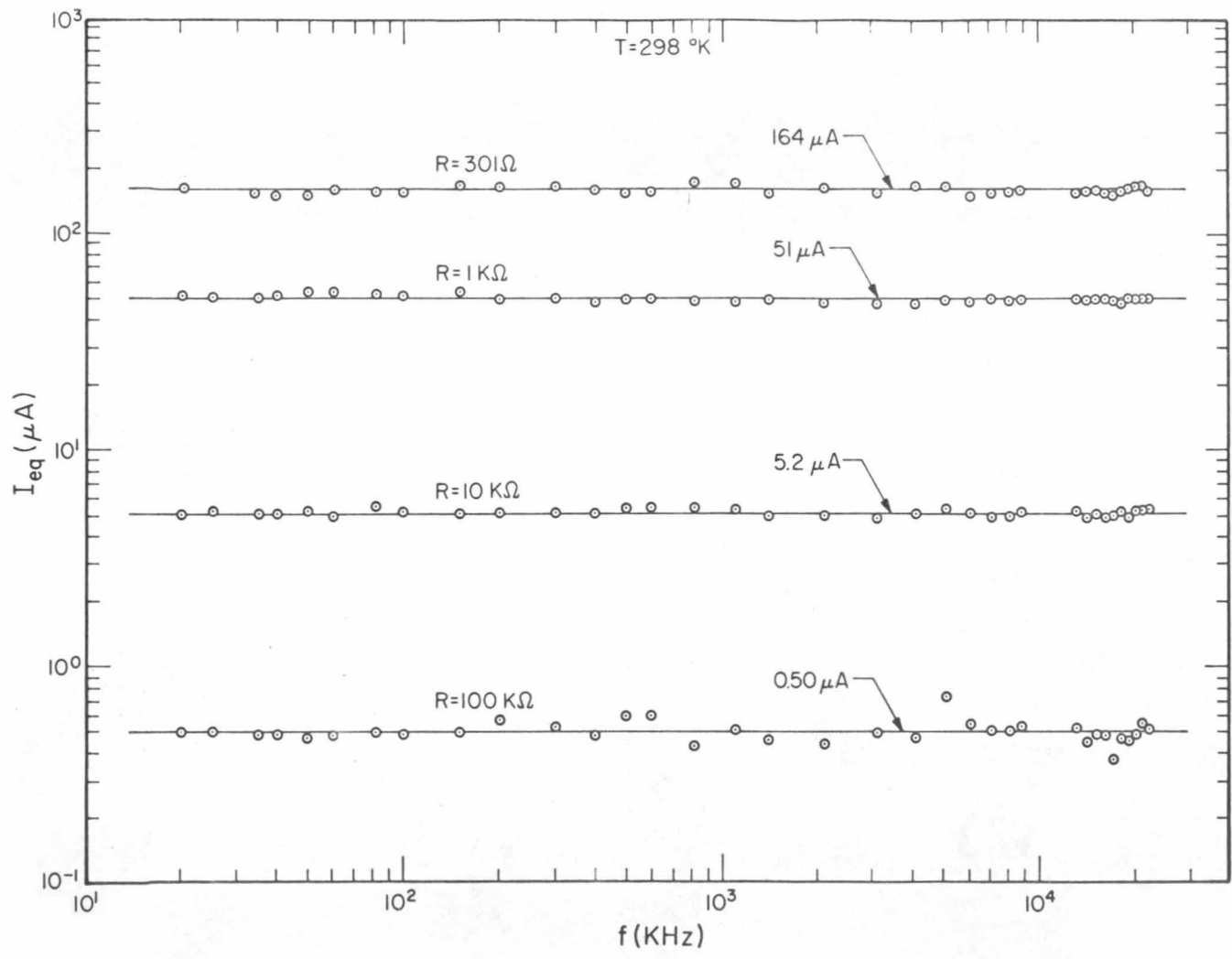


Figure E.4.1. Equivalent noise current for a 100k Ω , 10k Ω , 1k Ω and 301 Ω metal film resistor from 20kHz to 22MHz.

APPENDIX FTEMPERATURE ENVIRONMENT AND THERMOSTAT

F.1. General Considerations. The principle applied to vary the temperature of the device under test is to heat precooled nitrogen gas to the desired temperature and expose the device to this gas. A thermally insulated fixture houses the device and heating element. Feedback is utilized to maintain a constant temperature within the chamber. Temperatures from 100°K to over 400°K have been achieved with this system.

F.2. Description of Thermostat. Figure F.2.1 shows the experimental arrangement. Nitrogen gas is passed through a coiled copper tube submersed in liquid nitrogen. A reduction valve and flowmeter, which is calibrated from 0 up to 40 SCFH (Standard Cubic Feet per Hour), regulates the gas flow. The precooled gas flows to a heater coil where it is heated and subsequently enters the temperature chamber which contains the device. The ambient temperature is raised in the same manner but without precooling the gas (i.e. no liquid nitrogen).

The feedback configuration used for control of the temperature consists of a thermocouple sensor, temperature reference source, comparison voltage source, and amplification system (dark lines in Fig. F.2.1). An iron-constantan thermocouple located in the temperature chamber near the device is the sensor. The iron-constantan wires are carried through the amplifier enclosure to a copper block located in a crystal oven (Monitor Model 512, $T = 349.7^{\circ}\text{K}$). This establishes the temperature of the reference junction. The output voltage between the

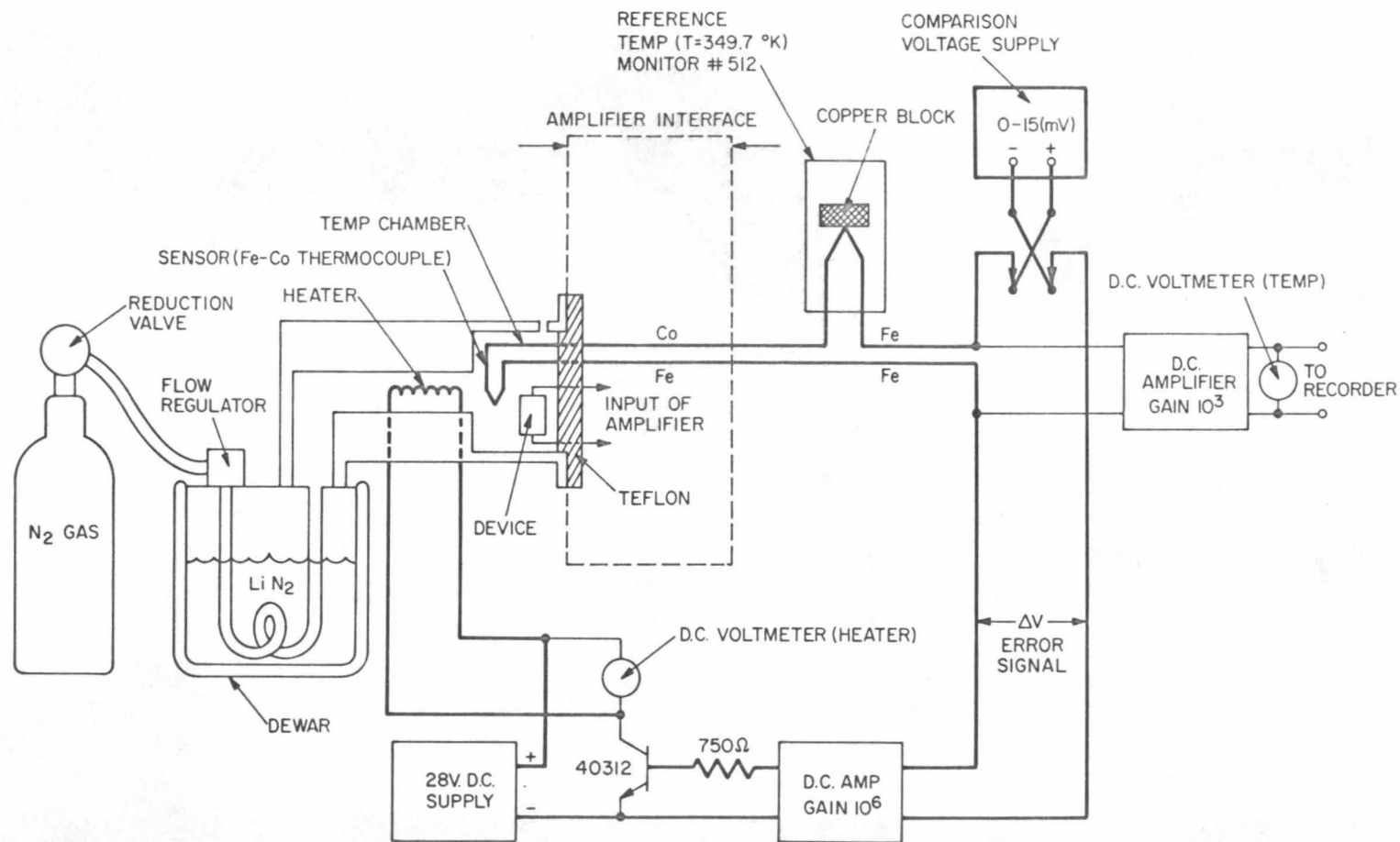


Figure F.2.1. Experimental arrangement for thermostat.

sensor and reference thermocouple junctions is compared to a variable (0-15mv) voltage source. An error voltage ΔV resulting from this comparison is amplified by two cascaded chopper stabilized amplifiers with a total voltage gain of 10^6 . This amplified error voltage is the input signal for a power transistor (RCA 40312) with the heater coil as its collector load. If ΔV is greater than 0v, the heater coil will draw current from its 28v dc supply. The heater, which is composed of Nichrome wire wound around four ceramic tubes and assembled in a "bird cage" fashion, has a small heat capacity and a resistance of approximately 20Ω . Therefore, the heater is capable of delivering 39 watts into the gas stream. Indication of the chamber temperature is provided by a X1000 chopper stabilized amplifier and a dc voltmeter. A recorder output is also supplied.

F.3. Operation and Procedure. The chamber temperature is determined by setting the comparison voltage. Depending upon the desired temperature, the voltage across the heater coil will be 0v (off) or 28v (on). Successful operation of the system is achieved when the measured heater voltage is somewhere between 0 and 28v. This is accomplished by adjusting the flowmeter and or the gain of the error signal amplifier. When the system is properly adjusted, a change in temperature (typically 20%) is accomplished within a few minutes. The temperature will generally overshoot and then undershoot once before accurate regulation is achieved.

In order that the room temperature characteristics of the amplifier remain constant, a thermal insulating wall which consists of a Teflon disc is used to couple the temperature chamber to the amplifier enclosure.

Stainless steel wires, which have a relatively low thermal conductivity, are used to carry the noise signals and biasing current of the device through the temperature wall to the amplifier input. Furthermore, the temperature chamber being made of copper provides an extension the Faraday shield.

F.4. Calibration. With ice-water (273°K) as a reference temperature, the iron-constantan thermocouple is calibrated at liquid nitrogen (77°K) and found to be less than 1% from the values quoted in standard calibration tables.^(F.1) Using this calibrated thermocouple, the measured temperature of the crystal oven is 349.7°K . Calibration of the comparison voltage supply indicates an error of $10\mu\text{V}$ (less than 1% error for voltages greater than 1mV).

For noise considerations, the sensor thermocouple is not directly attached to the device. Therefore, in order to insure that the device temperature is that of the temperature chamber, the following measurements are performed. A $1\text{k}\Omega$ metal film resistor is placed in the temperature chamber and the spectral noise density is measured at 100°K and 200°K . Figure F.4.1 shows the results in which the measured temperature of the resistor R is determined from $T = qRI_{\text{eq}}/2k$. Table F.4.1 summarizes the results.

TABLE F.4.1

Calibration values for temperature chamber.

T (Thermocouple)	T (Resistor)	% Error
100°K	103°K	3%
200°K	205°K	2.5%

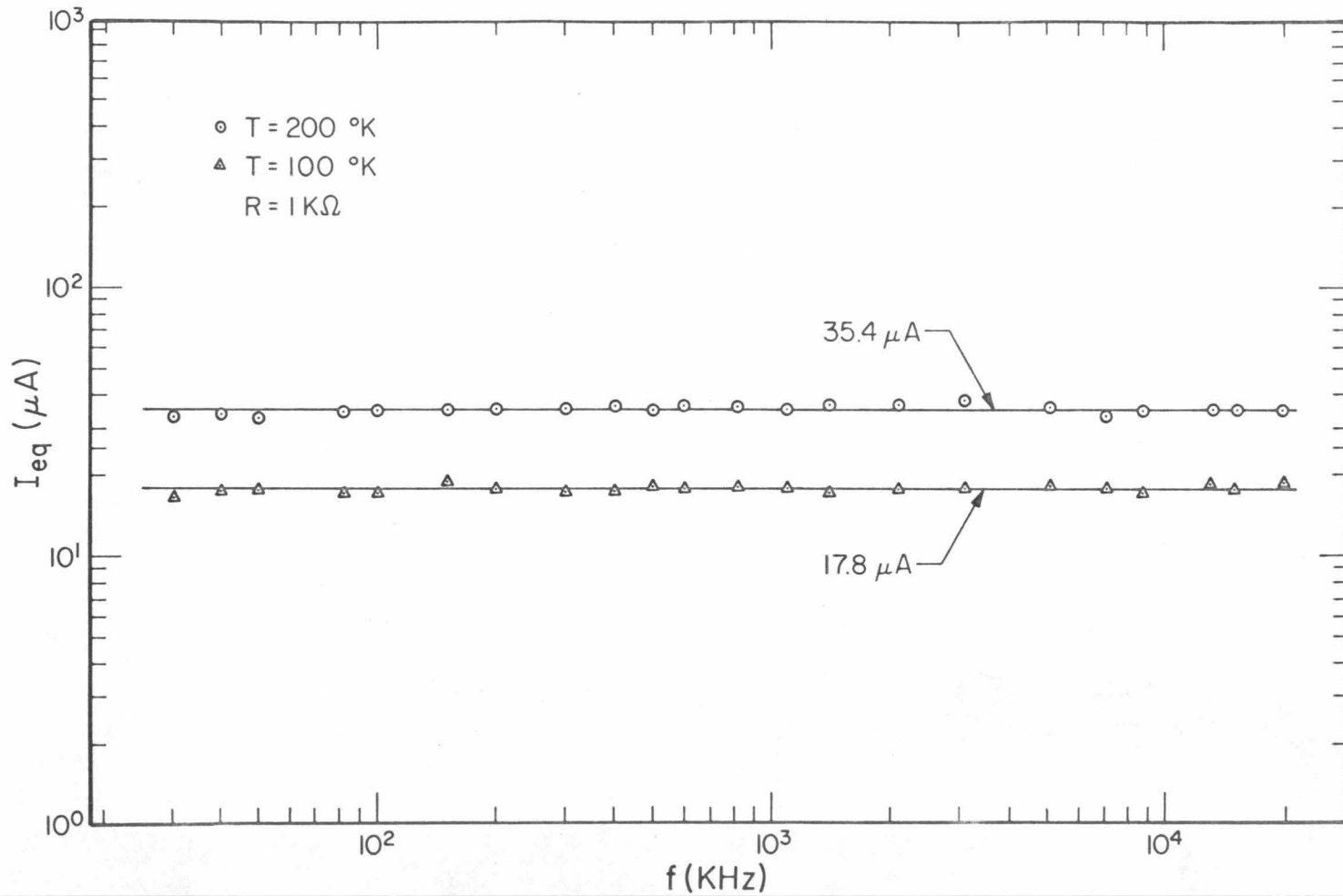


Figure F.4.1. Equivalent noise current for a 1kΩ resistor at 100°K and 200°K ambient temperature.

There is excellent agreement between the temperature as measured by the thermocouple and that of the resistor which is determined from the noise measurement. This illustrates the fact that the lattice temperature of the device (under normal operating conditions) is equal to the ambient temperature of the chamber to within 3%.

APPENDIX GCURVE FITTING AND ERROR ANALYSIS

G.1. Introduction. In the present case, the experimentally measured equivalent noise current of the double injection diode can be represented by the equation

$$I_{eq} = C_1 + \frac{C_2}{\left[\frac{C_3}{f^3} \right]} \quad (G.1.1)$$

where f is between 10kHz and 22MHz. The first term C_1 represents the "white" or thermal noise level, whereas the second term represents the "excess" noise (due to generation-recombination). In order to improve upon the estimate of C_1 , Eq.(G.1.1) is fitted to the data by a least-squares procedure.

G.2. Least-Squares Curve Fitting of a Function $I_{eq} = y(f, C_v)$. (G.1)

Consider the function $y(f, C_v)$ which need not be linear in the coefficients C_v . The independent variable f is real and assumed to have no errors. The data consist of L points which shall exceed the N parameters C_v (i.e. $v = 1, \dots, N$) to be determined. Each point is represented by the number pair I_{eq_i}, f_i . The I_{eq_i} 's are assumed to be uncorrelated, however, the absolute errors in the I_{eq_i} 's are not, in general, equal. Therefore, the weights w_i are incorporated. A given initial set of estimated coefficients is represented by $C_v^{(0)}$ ($v = 1, \dots, N$). The function is now linearized in the coefficients by means of a Taylor expansion through $O(\Delta C_v^2)$. Thus,

$$y(f_{i,C_v}) - y(f_i, C_v) \Big|_{\substack{C_1 = C_1^{(0)} \\ \vdots \\ C_N = C_N^{(0)}}} = \Delta y_i, \quad (\text{G.2.1})$$

where

$$\Delta y_i = \sum_{v=1}^N d_v \Delta C_v + O(\Delta C_v^2), \quad (\text{G.2.2})$$

and

$$d_v = \frac{\partial y(f_i, C_v)}{\partial C_v} \Big|_{\substack{C_1 = C_1^{(0)} \\ \vdots \\ C_N = C_N^{(0)}}}. \quad (\text{G.2.3})$$

The quantity

$$\sum_{i=1}^L w_i (y_i - \Delta y_i)^2 \quad (\text{G.2.4})$$

where

$$y_i = I_{eq_i} \quad (\text{G.2.5})$$

is now minimized. After differentiation versus the N coefficients C_v , the N linear equations for the ΔC_v are given by

$$\sum_{i=1}^L w_i d_1^2 \Delta C_1 + \sum_{i=1}^L w_i d_1 d_2 \Delta C_2 + \cdots + \sum_{i=1}^L w_i d_1 d_N \Delta C_N = \sum_{i=1}^L w_i y_i d_1$$

$$\sum_{i=1}^L w_i d_1 d_2 \Delta C_1 + \sum_{i=1}^L w_i d_2^2 \Delta C_2 + \cdots + \sum_{i=1}^L w_i d_2 d_N \Delta C_N = \sum_{i=1}^L w_i y_i d_2$$

⋮

$$\sum_{i=1}^L w_i d_1 d_N \Delta C_1 + \sum_{i=1}^L w_i d_2 d_N \Delta C_2 + \cdots + \sum_{i=1}^L w_i d_N^2 \Delta C_N = \sum_{i=1}^L w_i y_i d_N \quad (\text{G.2.6})$$

By solving these equations for the ΔC_v , an improved estimate (\bar{C}_v) for the coefficients is given by

$$\bar{C}_v = C_v^{(0)} + \Delta C_v \quad (\text{G.2.7})$$

The analysis is now repeated using the improved coefficients \bar{C}_v as the initial estimates.

G.3. Determination of the Weights w_i . A good approximation for the spectral noise density at a center frequency f is (see Appendix C)

$$I_{\text{eq}} = \begin{bmatrix} v_1^2 - v_a^2 \\ \eta v_2^2 - v_1^2 \end{bmatrix} I_c - \begin{bmatrix} \tilde{v}_1^2 - \tilde{v}_a^2 \\ \tilde{v}_2^2 - \tilde{v}_1^2 \end{bmatrix} \tilde{I}_c \quad (\text{G.3.1})$$

where the time average symbols are dropped for convenience. The weight, which is proportional to the reciprocal of the variance σ^2 , is given by $w = 1/\sigma^2$. By considering the propagation of errors, the variance is calculated accordingly as

$$\sigma^2 = \bar{\sigma}^2 + \tilde{\sigma}^2, \quad (\text{G.3.2})$$

where

$$\bar{\sigma}^2 = \left[\frac{I_c}{\eta V_2^2 - V_1^2} \right]^2 \left\{ \left[\frac{2V_1^2(\eta V_2^2 - V_a^2)}{\eta V_2^2 - V_1^2} \right]^2 + \left[\frac{2V_2^2[V_1^2 - V_a^2]}{\eta V_2^2 - V_1^2} \right]^2 + (2V_a^2)^2 \right\} \quad (\text{G.3.3})$$

and

$$\tilde{\sigma}^2 = \left[\frac{\tilde{I}_c}{\tilde{V}_2^2 - \tilde{V}_1^2} \right]^2 \left\{ \left[\frac{2\tilde{V}_1^2(\tilde{V}_2^2 - \tilde{V}_a^2)}{\tilde{V}_2^2 - \tilde{V}_1^2} \right]^2 + \left[\frac{2\tilde{V}_2^2[\tilde{V}_1^2 - \tilde{V}_a^2]}{\tilde{V}_2^2 - \tilde{V}_1^2} \right]^2 + (2\tilde{V}_s^2)^2 \right\} \quad (\text{G.3.4})$$

In this case, I_c and \tilde{I}_c are assumed to have no errors. Also, the quantities $\langle V_1^2 \rangle^{1/2}$, $\langle V_2^2 \rangle^{1/2}$, $\langle V_a^2 \rangle^{1/2}$, etc. are assumed to be Gaussian distributed with equal relative standard errors.

In order to demonstrate that the relative standard errors are approximately equal, 500 measurements are made on each of the noise readings $\langle V_a^2 \rangle^{1/2}$ and $\langle V_1^2 \rangle^{1/2}$. The readings are taken with the active integrator set for a 2 second total integration time. Figure G.3.1 shows the experimental data in which the relative standard errors for $\langle V_a^2 \rangle^{1/2}$ and $\langle V_1^2 \rangle^{1/2}$ are 0.80% and 0.84% respectively. A Gaussian with the same mean and variance is also fitted to the

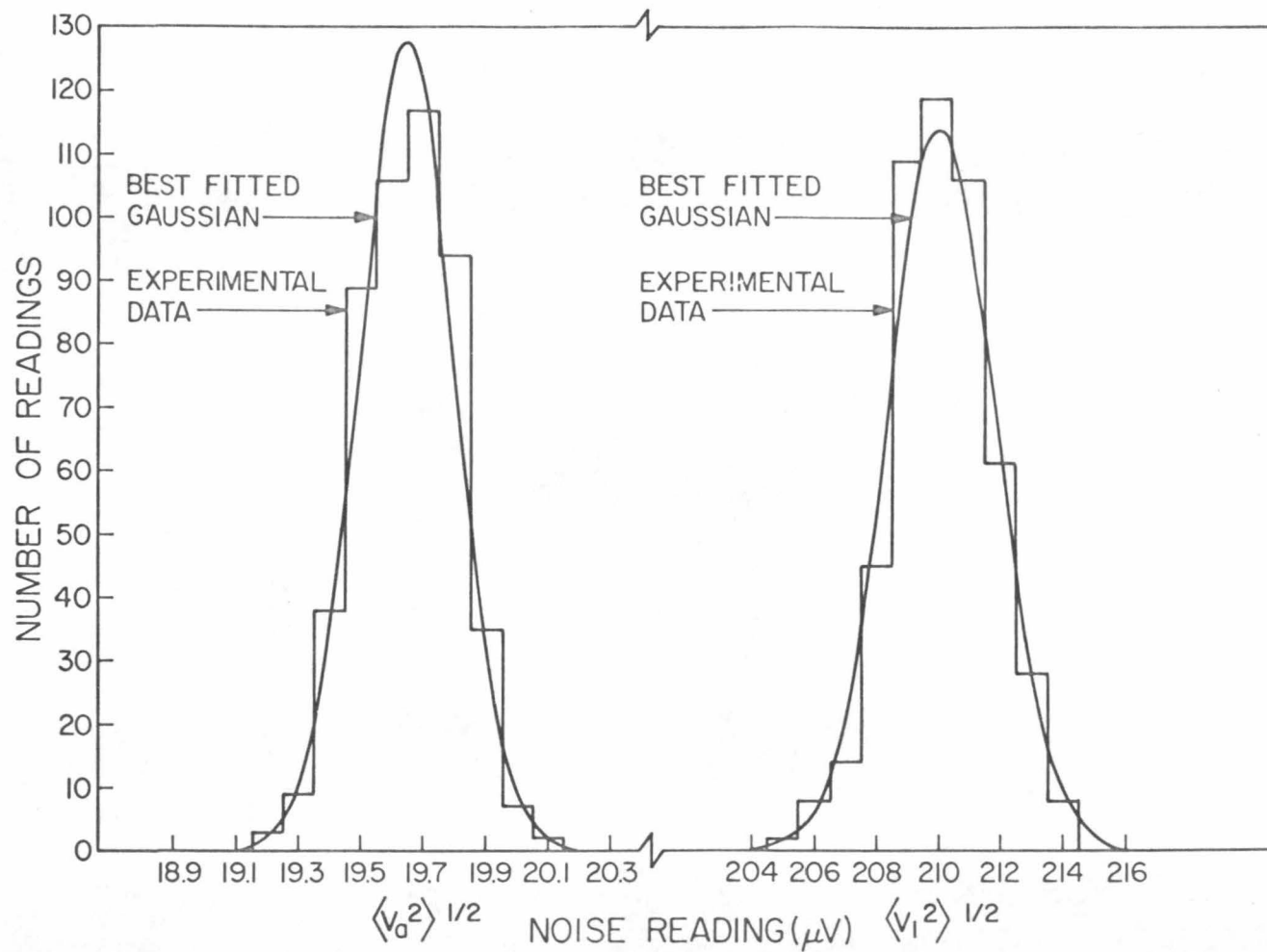


Figure G.3.1. Experimental data for 500 noise readings per histogram; a Gaussian with the same mean and variance is fitted to the experimental data.

appropriate data. The theoretical standard error $\alpha^{1/2}$ is given by

$$\alpha^{1/2} = (1/2T \Delta f)^{1/2} \quad (\text{G.3.5})$$

where

T = total integration time.

From Eq.(G.3.5), the theoretical relative standard error is 0.91% which is in good agreement with the measured results.

G.4. Computer Program. A computer program is written to perform the necessary arithmetical manipulations involved in calculating I_{eq} from Eq.(C.5.7). In general, more than 25 data points (I_{eq_i}, f_i) are determined throughout the frequency range from 10kHz to 22 MHz. Equation (G.1.1) is then fitted to the data using the least-squares procedure of G.2. In this procedure, the iterations are continued until the sum of the squares, $\sum \Delta y^2$, of the residuals, in two successive iterations m and $m+1$ satisfies the condition

$$\frac{\sum \Delta y^2_m - \sum \Delta y^2_{m+1}}{\sum \Delta y^2_{m+1}} < \epsilon \quad (\text{G.4.1})$$

An error matrix is also calculated in which the diagonal terms are the R.M.S. errors β_v of the coefficients C_v . Estimates of β_v are given by

$$\beta_v = \left[\frac{\text{SUMSQ}}{L-N} A_{VV} \right]^{1/2}, \quad (\text{G.4.2})$$

where A is the inverted matrix of the set of linear equations, and SUMSQ is the magnitude of the sum squares of the residuals after the last iteration. A graphical plot of the data plus the fitted curve is also provided.

REFERENCES

- 1.1. S. T. Liu, S. Yamamoto, and A. van der Ziel, "Noise in Double Injection Space-Charge-Limited Diodes", Appl. Phys. Letters 10, 308; 1967.
- 1.2. F. Driedonks, R. J. J. Zijlstra, and C. Th. J. Alkemade, "Double Injection and High Frequency Noise in Germanium Diodes", Appl. Phys. Letters 11, 318; 1967.
- 1.3. M-A. Nicolet, H. R. Bilger, and E. R. McCarter, "Noise Suppression in a Double Injection Silicon Diode", Appl. Phys. Letters 9, 434; 1966.
- 1.4. A. Rose, "Comparative Anatomy of Models for Double Injection of Electrons and Holes into Solids", J. Appl. Phys. 35, 2664; 1964.
- 1.5. M. A. Lampert, "A Simplified Theory of Two-Carrier, Space-Charge-Limited Current Flow in Solids", RCA Rev. 20, 682; 1959.
- 1.6. M. A. Lampert, A. Rose, "Volume Controlled, Two-Carrier Current in Solids: The Injected Plasma Case", Phys. Rev. 121, 26; 1961.
- 1.7. M. A. Lampert, "Double Injection in Insulators", Phys. Rev. 125, 126; 1962.
- 1.8. J. W. Mayer, R. Baron, and O. J. Marsh, "Observation of Negative Resistance in Long Silicon p- π -n Diodes", J. Appl. Phys. Letters 6, 38; 1965.
- 1.9. J. W. Mayer, R. Baron, and O. J. Marsh, "Observation of Double Injection in Long Silicon pin Structures", Phys. Rev. 137, A286; 1965.
- 1.10. J. W. Mayer, O. J. Marsh, and R. Baron, "Double Injection in Long Silicon p- π -n Structures", J. Appl. Phys. 39, 1447-1455; 1968.
- 1.11. R. Baron, "Effects of Diffusion on Double Injection in Insulators", Phys. Rev. 137, A272-A285; 1965.
- 1.12. R. Baron, "Effects of Diffusion and Thermal Generation on Double Injection in Semiconductors", J. Appl. Phys. 39, 1435-1446; 1968.
- 1.13. D. H. Lee and M-A. Nicolet, "Space-Charge-Limited Currents in Solids for Various Geometries and Field-Dependent Mobility", Solid-State Electronics 8, 182-184; 1965.
- 1.14. B. Meltzer, "Space-Charge-Limited Currents in Cylindrical and Spherical Insulator Diodes", J. Electron. Control 8, 171-176; 1960.

- 1.15. V. Rodriguez and M-A. Nicolet, "Influence of Geometry on Unipolar Space-Charge-Limited Current in Solids and in Vacuum", *J. Appl. Math and Phys. (ZAMP)* 18, 273-280; 1967.
- 1.16. R. Baron, O. J. Marsh, and J. W. Mayer, "Transient Response of Double Injection in a Semiconductor of Finite Cross Sections", *J. Appl. Phys.* 37, 2614-2626; 1966.
- 1.17. R. Baron, J. W. Mayer, Double Injection in Semiconductors, to be published.
- 1.18. W. Schottky, "Uber spontane Stromschwankungen in verschiedenen Elektrizitätsleitern", *Ann. d. Phys. (Leipzig)*, 57, 541; 1918.
- 1.19. H. B. Callen and T. A. Welton, "Irreversibility and Generalized Noise", *Phys. Rev.* 83, 34-40; 1951.
- 1.20. A. van der Ziel, "Noise in Junction Transistors", *Proc. IRE* 46, 1019-1038; 1958.
- 1.21. A. van der Ziel and K. M. van Vliet, "H. F. Thermal Noise in Space-Charge-Limited Solid State Diodes-II", *Solid-State Electronics* 11, 508-509; 1968.
- 1.22. H. R. Bilger, P. R. Worch, L. L. Lee, and M-A. Nicolet, "Generation-Recombination Noise in Double-Injection", to be published.
- 1.23. A. B. Fazakas and A. Friedman, "On the Double Injection Current Noise in Solids", *Phy. Stat. Sol.* 28, 385-393; 1968.
- 1.24. A. van der Ziel, "Noise in Double-Injection-Space-Charge-Limited Solid State Diodes", *IEEE MTT* 16, 308; 1968.
- 1.25. J. H. Liao, "Noise in Germanium Double Injection Space-Charge-Limited Diodes", *Elect. Letters* 4, 402; 1968.
- 2.1. R. H. Dean, "Transient Double Injection in Germanium", *Appl. Phys. Letters* 13, 164; 1968.
- 2.2. M. Neuberger, "Silicon Data Sheets", DS-137, Electronic Properties Information Center, Hughes Aircraft; 1964.
- 2.3. D. M. Evans, "The Temperature Dependence of the Low-Level Lifetime and Conductivity Mobility of Carriers in Silicon", *J. of Electronics and Control*, 7, 112-122; 1959.
- 2.4. D. Long and J. Myers, "Ionized-Impurity Scattering Mobility of Electrons in Silicon", *Phys. Rev.* 115, 1107; 1959.
- 2.5. J. W. Mayer, O. J. Marsh and R. Baron, "Double Injection in Long Silicon p- π -n Structures", *J. Appl. Phys.* 39, 1447-1455; 1968.

- 2.6. G. W. Ludwig and R. L. Watters, "Drift and Conductivity Mobility in Silicon", Phys. Rev. 101, 1699-1701; 1956.
- 2.7. Dow Corning Ingot, No. 06-0400-7.
- 2.8. J. Messier and J. M. Flores, "Temperature Dependence of Hall Mobility and μ_H/μ_D for Si", J. Phys. Chem. Solids, 24, 1539-1542; 1963.
- C.1. A. van der Ziel, Noise, Prentice Hall, Englewood Cliffs, New Jersey, 1954.
- C.2. F. C. Williams, "Fluctuation Voltage in Diodes and in Multi-Electrode Valves", J. Inst. Elec. Engrs. (London), 79, 349; 1936.
- C.3. W. Schottky, "Uber spontane Stromschwankungen in verschiedenen Elektrizitätsleitern", Ann. d. Phys. (Leipzig), 57, 541; 1918.
- C.4. H. Nyquist, "Thermal Agitation of Electronic Charge in Conductors", Phys. Rev., 32, 110; 1928.
- D.1. Sylvania Electronic Tubes; Engineering data specifications may be obtained from the Technical Publications Section Emporium, Penn.
- D.2. A. van der Ziel, "Thermal Noise in Field-Effect Transistors", Proc. IRE, 50, 1808-1812; 1962.
- D.3. E. R. McCarter, Ph.D. Dissertation, Oklahoma State University; 1965.
- F.1. For calibration tables see Hdbk. Chem. Phys., Coll. Ed., p. E-91; 1966-1967.
- G.1. W. C. Hamilton, Statistics in Physical Science, p. 150ff, Ronald Press Co., New York; 1964.